

# **Heat Transfer Model for End Winding Cooling of Hydro Generators by Computational Fluid Dynamics Analysis**

submitted as doctoral dissertation for obtaining the academic  
degree of doctor of technical sciences  
at the Graz University of Technology

by

Stephan Klomberg

Supervisor/First reviewer: Prof. Dr.-techn. Oszkár Bíró  
Second reviewer: Dr.-techn. Bernhard Brandstätter

Graz, 2015



## **Preface**

After three years of intensive work at the Christian Doppler Laboratory for Multiphysical Simulation, Analysis and Design of Electrical Machines I would like to thank all supporters for their valuable contributions to my thesis during this time.

Especially, I would like to express my deep gratitude to my PhD supervisor Prof. Dr.-techn. Oszkár Bíró for his precious guidance and feedback during the last years.

Furthermore, it is a pleasure to thank the Christian Doppler Research Association and the Andritz Hydro GmbH for the financial support of this work. My thanks are also extended to my supervisors at the industrial partner, Dr.mont. Ernst Farnleitner and Dr.mont. Gebhard Kastner, for their inspiring support, advices and knowledge transfer.

I am also very grateful to my colleagues at the Institute for Fundamentals and Theory in Electrical Engineering at the Graz University of Technology.

Finally, I would like to thank my family and friends for their continued care, support and encouragement.



## **Abstract**

Lumped parameter thermal models calculate the temperature rises in air-cooled hydro generators in the first design step. These models need input parameters as wall temperatures, power losses or convective heat transfer coefficients for the various components. The heat transfer coefficients are generally determined by measurements or by analytical formulas for simple geometries. However, since detailed temperature measurements of large generators are very time and cost expensive and hence unusual, it is the state-of-the-art method to use approximation models for these coefficients at specific walls of the end winding bars, stator ducts or pole surfaces.

The heat transfer model presented in this work computes the convective heat transfer coefficients at the end winding walls considering different ventilation schemes applied. Dimensionless numbers have been used for the approximation formulation and the unknown coefficients have been correlated with numerical results using least square techniques. On the one hand, computational fluid dynamics simulations of 15 different ventilation schemes have yielded an enormous amount of data for the identification of a heat transfer model and, on the other hand, the definition of the various heat transfer model equations has benefited from the numerical results, too.

Furthermore, the heat transfer model has been validated by heat conduction computations as well as by temperature measurements of several hydro generators.

Keywords: computational fluid dynamics, convective heat transfer coefficient, cooling, end winding bars, heat conduction, heat transfer, lumped parameter network, stator bars, synchronous generators, thermal analysis



## Kurzfassung

Konzentrierte thermische Netzwerke werden in der ersten Konstruktions- und Auslegungsphase von Luft-gekühlten Wasserkraftgeneratoren verwendet, um die Bauteiltemperaturen im Gesamtsystem zu untersuchen. Diese Netzwerke benötigen Eingabeparameter wie Wandtemperaturen, Leistungsverluste oder konvektive Wärmeübergangskoeffizienten. Die Wärmeübergangskoeffizienten werden grundsätzlich durch Messungen bestimmt oder durch Gleichungen von einfachen Geometrien abgeleitet. Da allerdings ausführliche Temperaturmessungen bei Großgeneratoren sehr zeit- und kostenintensiv und deshalb sehr selten sind, werden dem Stand der Technik entsprechend vereinfachte mathematische Näherungsmodelle verwendet, um die Wärmeübergangskoeffizienten von spezifischen Wänden des Statorwickelkopfes, der Statorschlitze oder der Poloberflächen zu bestimmen.

Das in dieser Dissertation präsentierte Wärmeübergangsmodell berechnet den konvektiven Wärmeübergangskoeffizienten der Wickelkopfstäbe unter Berücksichtigung verschiedener angewandter Ventilationsmethoden. Für die Formulierung der Näherungsmodelle wurden dimensionslose Kennzahlen verwendet und mit der Methode der kleinsten Fehlerquadrate wurden durch Korrelation mit numerischen Ergebnissen die unbekanntenen Koeffizienten definiert. Zum einen hat der Einsatz der numerischen Strömungsmechanik eine enorme Datenmenge über die 15 verschiedene Ventilationsmethoden für die Korrelation des Wärmeübergangsmodelles realisiert, zum anderen hat auch die Definition der Modellgleichungen von den numerischen Ergebnissen profitiert.

Außerdem wurde das Wärmeübergangsmodell mit Wärmeleitungsgleichungen als auch mit Temperaturmessungen von verschiedenen in Betrieb befindlichen Wasserkraftgeneratoren validiert.

Schlagwörter: numerische Strömungsmechanik, konvektiver Wärmeübergangskoeffizient, Kühlung, Wickelkopf-Stäbe, Wärmeleitung, Wärmetransport, konzentriertes thermisches Netzwerk, Stator-Stäbe, Synchrongeneratoren, thermische Untersuchung



## **Statutory Declaration**

I declare that I have authored this thesis independently, that I have not used other than the declared sources / resources and that I have explicitly marked all material which has been quoted either literally or by content from the used sources.

## **Eidesstattliche Erklärung**

Ich erkläre an Eides statt, dass ich die vorliegende Arbeit selbstständig verfasst, andere als die angegebenen Quellen/Hilfsmittel nicht benutzt und die den benutzten Quellen wörtlich und inhaltlich entnommenen Stellen als solche kenntlich gemacht habe.

---

Ort

---

Datum

---

Unterschrift



# Contents

<b>CONTENTS</b> .....	<b>I</b>
<b>1 INTRODUCTION</b> .....	<b>1</b>
1.1 MOTIVATION .....	1
1.2 REVIEW OF PAST INVESTIGATIONS .....	4
1.3 THESIS OUTLINE.....	8
<b>2 FUNDAMENTALS</b> .....	<b>9</b>
2.1 SYNCHRONOUS GENERATORS .....	9
2.1.1 Design of large hydro generators.....	10
2.1.2 Heating and Cooling .....	12
2.1.3 Machine losses .....	13
2.2 FLUID DYNAMICS .....	14
2.2.1 Introduction.....	14
2.2.2 Basic equations of continuum mechanics .....	15
2.2.2.1 Continuity equation.....	15
2.2.2.2 Momentum equation .....	16
2.2.2.3 Energy equation .....	18
2.2.3 Turbulent flow .....	19
2.2.4 The Navier-Stokes equations for laminar flow .....	20
2.2.5 The Reynolds equations for turbulent flow .....	22
2.2.6 Boundary layer theory .....	24
2.3 HEAT TRANSFER .....	28
2.3.1 Heat conduction .....	28
2.3.2 Heat convection .....	31
2.4 COMPUTATIONAL FLUID DYNAMICS .....	37
2.4.1 Discretization .....	38
2.4.2 Common numerical techniques .....	40
2.4.3 Numerical treatment of turbulent flows.....	41
2.4.3.1 Turbulence modelling .....	42
2.4.3.2 SST $k-\omega$ model.....	44

2.4.4	Near Wall Treatment .....	45
2.4.4.1	Standard wall functions .....	45
2.4.4.2	Scalable wall functions .....	46
2.4.4.3	Automatic wall treatment .....	47
2.4.4.4	Heat flux computation .....	48
2.4.5	Modelling flows with moving reference frames .....	49
2.4.5.1	Mixing plane .....	51
2.4.5.2	Frozen rotor .....	53
<b>3</b>	<b>NUMERICAL MODELS.....</b>	<b>57</b>
3.1	INVESTIGATED VENTILATION SCHEMES .....	57
3.2	POLE SECTOR MODEL.....	61
3.3	SLOT SECTOR MODEL.....	64
3.4	SIMULATION SET-UP .....	65
3.4.1	Mesh generation .....	65
3.4.2	Boundary conditions and loss sources.....	67
3.4.3	Fluid properties.....	68
3.5	VALIDATION OF THE REDUCED MODEL .....	69
3.5.1	Mesh sensitivity study .....	69
3.5.2	Comparison to the steady state results.....	72
3.5.3	Comparison to transient results .....	78
3.5.4	Comparison of the computational time .....	81
3.6	HEAT CONDUCTION MODELS.....	82
3.6.1	Heat conduction of the end winding bar.....	82
3.6.2	Conjugate heat transfer model.....	83
<b>4</b>	<b>RESULTS OF THE PARAMETRIC STUDY .....</b>	<b>85</b>
4.1	COMPARISON OF THE VENTILATION SCHEMES.....	85
4.2	FLOW DIRECTION FOR RADIAL FAN SCHEMES.....	90
<b>5</b>	<b>HEAT TRANSFER MODEL .....</b>	<b>93</b>
5.1	CHARACTERIZATION OF THE HEAT TRANSFER COEFFICIENT.....	95
5.2	CALCULATION OF THE INDEPENDENT NUSSELT NUMBER .....	97
5.2.1	Mass flow through bars with external cooling .....	100
5.2.2	Mass flow through bars with shaft mounted cooling .....	100

<b>6</b>	<b>VALIDATION OF THE HTM.....</b>	<b>103</b>
6.1	VALIDATION WITH CFD RESULTS .....	103
6.2	VALIDATION WITH HEAT CONDUCTION CALCULATIONS .....	107
6.3	VALIDATION WITH MEASUREMENTS .....	109
6.3.1	Accuracy of the parametric bar model.....	110
6.3.2	Comparison with measurements .....	115
<b>7</b>	<b>SUMMARY OF NEW SCIENTIFIC RESULTS .....</b>	<b>119</b>
	<b>BIBLIOGRAPHY .....</b>	<b>123</b>
	<b>APPENDIX .....</b>	<b>133</b>



# 1 Introduction

## 1.1 Motivation

Climate change has become one of the most pressing topics of mankind since the beginning of this century. An obvious temperature rise in the atmosphere and the oceans is occurring and, furthermore, the antarctic ice sheet is decreasing causing sea levels to rise. The main reason for this global warming is the increase of the amount of greenhouse gases in the atmosphere. In the next decades, one of the most important challenges will be to counteract these processes by reducing the emission of carbon dioxide, methane and ozone. Especially the carbon dioxide emissions of caloric power plants, traffic and industry have a large influence on the greenhouse effect [1].

One significant measure to achieve the reduction of the greenhouse gases is the progressive change of the sources of energy conversion to renewable energy as wind power, solar energy, biomass, geothermal energy or hydropower. Particularly, hydropower energy has a high unused potential all over the world with pumped-storage, run-of-the-river or tidal power plants as examples. These power generation techniques are well-engineered and have been used for over hundred years. However, there is always room for improvement in every component of the power plant. An increase in the efficiency, performance and reliability of turbines, pumps, generators or transformers leads to lower energy losses and lower maintenance costs.

From the viewpoint of mechanical engineering, the generators and motors are still the least investigated parts of hydropower plants. These electrical machines convert the mechanical energy of the turbine or pump into electrical energy or vice versa.

Due to this transformation, a few percent of the nominal power of the generator are losses, wherefore the dissipated thermal power can be in the range of some megawatts. The most significant losses during operation are the copper, iron, eddy current, friction and windage losses. Their dissipation has to be guaranteed by an appropriate cooling scheme. Furthermore, there is also a high potential to improve the design process of the thermal management of these machines, especially in the stator ducts, the rotor with poles and the end winding bars.

The cooling of generators can be realized with different media and distinct techniques. Beginning with air cooling for machines rated up to 400 megawatts, the coolant changes with increasing power to hydrogen and further to water or oil. Water has the advantage of a high thermal conductivity and hence a more or less constant temperature distribution reducing the mechanical stresses and increasing the durability and reliability of the machine. The ventilation losses and aerodynamic losses are also smaller than those generated in air-cooled machines. However, a water cooling system is complicated and its maintenance consumes much cost and time. Due to this fact, cooling with water and hydrogen is mainly used for high power generators with ratings beginning at 300-400 megawatts [2]. More details about cooling methods of electrical machines are presented in [3]. This work is focused on ventilation by air.

One of the key problems of the thermal management of generator components is the evaluation of the heat transfer rate at a specified temperature difference. The literature on heat transfer distinguishes three different types of heat transmission: conduction, radiation and convection. In electrical machines, the rate of the radiative heat transfer is negligibly low in comparison to the convective and conductive ones. The conductive heat transport in solid parts and the convective heat transfer from a solid to a cooling medium, or vice versa, are the significant phenomena for the thermal design of electrical machines. Conduction in a medium can be generally predicted by Fourier's law [4]. Convection, on the other hand, can be determined by analytical equations for simple geometries as tubes, plates or valves [5] and by measurements or by computational fluid dynamics (CFD) for complex shapes. A fundamental value for the heat convection is the wall heat transfer coefficient (HTC) which describes the energy transport between two media. It especially depends on the fluid properties and the flow conditions of the fluid near to walls.

Lumped parameter thermal networks are primarily used in the thermal design of electrical machines to estimate the temperature rise. A thermal model consists of thermal resistances, thermal capacitances and power losses (heat losses), analogously

to electrical circuits. The HTC is one important parameter and has to be specified for every component of the network.

The three major thermally relevant parts of a synchronous generator are the stator end winding bars, poles and stator ducts. The cooling of the stator ducts and the pole region has been investigated extensively in the last decades as described in section 1.2. However, the heat transmission at the end winding region has not yet received such attention, due to the high effort needed for empirical and computational investigations on complex geometries. Prototypes of such large machines are economically not affordable, wherefore temperature and other significant measurements in hydro generators are usually done during the operation in power plants.

As a result, the motivation for extensively investigating the cooling of the end winding region of large electrical machines by CFD is strong. Such simulations enable the acquisition of a large amount of flow data to facilitate defining analytical formulas for the heat transfer coefficient at the end winding walls. The development of such rules correlating various operational parameters to the HTC is one of the aims of the present work.

## 1.2 Review of past investigations

Many books deal with the theory and design of electrical motors and generators [6, 7]. However, these books do not treat the cooling of the machines in sufficient detail. A valuable introduction to the conversion of the electrical and mechanical losses into heat as well as to the conductive, convective and radiative heat transport in the machines is given in [3] and [8]. The general theory of the cooling and ventilation techniques is presented in [3] but a more detailed overview can be found in the publications [9-32].

The first step in the design process of electrical machines is primarily based on zero-dimensional tools like thermal and flow networks. The lumped parameter networks are able to analyze complex problems very quickly. Compared with other methods, these networks are simple, attractive and can give an accurate representation of the thermal conditions within the machine [9]. However, these circuits need input variables of pressure loss coefficients and convective HTC's. In the last decades, many publications have dealt with the determination of the parameters of such networks by generally focusing on small motors in a power class of a few kilovolt-amperes [9-18]. These machines have a simple design and cooling scheme. Several researchers have attempted to establish the heat transfer coefficient at the end winding bars by measurements [13], CFD [17], lumped parameter networks [10] or in combination of these methods [11, 12, 14]. They have set up simple analytical formulas by different approaches to calculate the convective heat transfer coefficient as an input parameter of the network. The PhD thesis in [18] has investigated such heat transfer coefficients for the end-region of a small electrical machine by CFD and measurements. The author presents an extremely accurate heat transfer prediction for the end winding bars of a totally enclosed fan cooled machine with one ventilation scheme. The drawback of this work is the fixed cooling method and hence, the limitation of the formulas for one machine only.

However, the heat transfer at the end winding bars or the flow around the end winding region of large machines can hardly be computed by using networks, while the application of three-dimensional numerical methods makes their calculation possible. Furthermore, heat and flow measurements of generators can be done at prototypes or at assembled machines in the plant. Prototypes of such large machines are too expensive and rarely used. Nevertheless, some publications compare CFD computations and measurements on a half-scale generator model [19, 20]. The

empirical data of a generator in a power plant are often used to verify and improve the design procedures discussed in the following.

The effort and the accuracy of a computational fluid dynamical simulation depend strongly on the numerical model used, the calculation approach and the mesh density. CFD computations result in the description of the detailed flow through the machine and can help optimize the cooling. Their disadvantage is the large computational effort needed. Some publications describing the use of CFD in the area of large generators as well as ones dealing with the comparison of CFD with or its impact on lumped parameter networks are reviewed in the next passages.

The numerical analysis of the convective heat transfer at the end winding bars, stator ducts or pole coils needs a fine mesh at the relevant surfaces. It is not possible to use such detailed grids to model the whole generator geometry with its large dimensions and all details, because the number of elements would increase enormously. As listed in [21], some state-of-the-art methods to simplify the numerical model of an electrical machine are using

1. an assumed axial symmetry
2. the circumferential periodicity
3. a separation of the fan model and generator model
4. an approximation of the rotor-stator interaction with steady state methods
5. a simple geometry without details
6. smooth walls at the surface instead of ribbed ones
7. a coarse mesh for less interesting areas

Most publications applying fluid flow computations in hydro generators use these simplifications to reduce the numerical effort. Several authors work with the state-of-the-art pole sector model (PSM) wherein the whole machine model is generally reduced by the simplifications 1-4 above. However, the computation time for a PSM of a whole generator is still very time consuming as the number of elements remains high. Some interesting examples are [22-25]. The authors have modelled one pole-sector of the generator with all end winding bars and stator ducts in this sector included. These models still need a number of days for the calculation. An early investigation of the air flow and heat transfer in a salient pole electrical machine is presented in [22]. This study looks at various aspects of using CFD in rotating electrical machines. The main focus is on the heat transfer at the rotor windings and the impact of the above assumptions. The authors of [23] have identified the advantages of CFD in the design process of large electrical machines. They have

pinpointed parameters with influence on the heat transfer, windage losses and pressure drop at the stator end winding bars. The most relevant parameters are the mass flow rate, fan outlet swirl, fan position and fan type. Different rotor-stator interaction modelling approaches are presented in [24]. The multiple frame of reference methods are compared and a study on the radial position of the interface between the pole and stator region has been accomplished. The application of CFD and flow networks for the cooling design of hydro generators is presented in [25]. A PSM has been used for the CFD computations and the results have shown a good agreement with those obtained from a thermal network.

In [26], a pole sector model of a generator including all components has been investigated. This is one of the rare publications with the authors not assuming an axial symmetry condition and additionally considering geometrical details as ribbed pole surfaces. Accordingly, the mesh size has increased enormously to about 125 million elements. The results have shown the asymmetric flow and pressure distribution of the investigated generator. In addition, these results have been used for a detailed conductive heat transfer simulation of a stator core compared with plant measurements. This method solves the heat conduction in the solid with sources of the electromagnetic losses and is also named conjugate heat transfer (CHT) method. This validation has proven the accuracy and the reliability of the state-of-the-art simulation approach using a PSM very well.

A further PhD thesis [27] deals with the CFD analysis of the rotor region of a salient pole generator. A simple model of the rotor with the pole gap has been used to compute the flow through the pole region and analyze the heat transfer at the pole winding surface. The results of this analysis have been used to find a set of formulas for the ventilation design by network calculations. Additionally, the windage losses and the influence of the pole geometry and dimensions on the cooling have been investigated. The numerical results have been validated with measurement results of a laboratory model.

Another possible simplification is treating the end winding or stator duct geometry as a porous medium. This technique simplifies the geometry and meshing and accelerates the analysis. An introduction to this topic is given in [28], where the end winding region is modelled as filled by a porous medium and the velocity and pressure fields in this area have been investigated. A second publication using a porous medium is [29]. Two different models have been built. The first model is a PSM, simplified by a porous medium in the end winding region and the stator ducts. The results of these simulations have shown good agreement with measurements at the ducts. The second model represents a periodic sector of the stator and extends

over one slot in the angular direction. A more detailed investigation of the flow in the stator ducts has been carried out using results of the first model as input parameters for the second one.

The authors of [20-26] have all used the commercial software package ANSYS CFX or FLUENT. However, it is hardly possible to customize the numerical solvers and utilities for special problems in ANSYS. Therefore, the flow simulations in [19] have been carried out by the free CFD toolbox OpenFOAM. It demonstrates the possibilities and the reliability of OpenFOAM for flow simulations in a small scale generator and compares the results with measurements. The simulation and the experiment have exhibited qualitative agreement and showed the influence of the end winding and inlet geometry on the flow path, too.

Measured data of a scaled generator, network calculations and CFD simulations have been used to arrive at a homogeneous air flow through the machine in [20]. Other works combining CFD and measurements for small-scale generators are described in [30-32]. Flow and temperature measurements in the pole region and the stator are presented in [30]. Based on these results, formulas for the dimensionless Nusselt number have been determined at the rotor pole, rotor slots and the stator. In [31], the authors have investigated the heat transfer on the pole face and the air gap numerically. The CFD and CHT studies have been validated by measurements on a test rig of a scaled rotor and stator. Finally, the heat transfer on the pole surfaces of an additional scaled generator is presented in [32].

## 1.3 Thesis outline

This thesis is subdivided into 7 chapters. The first chapter introduces the work with the motivation and a literature review which is related to the applied methods of numerical flow simulations in electrical machines as well as the determination approaches for the heat transfer coefficients at the end winding bars.

The following chapter 2 presents an introduction to hydro generators with the cooling and ventilation schemes. It will continue with fundamentals and theory of the heat transfer, fluid dynamics and CFD. The CFD part will especially describe the multiple frames of reference methods for a rotor-stator system.

Chapter 3 explains the reduction procedure of the whole generator model to the pole sector model (PSM) and finally to a novel reduced model named slot sector model (SSM). This chapter also presents a mesh density study at the bar walls and validates the SSM by comparison with the PSM and other reference studies. With this configuration setup, a comprehensive parametric study with 15 different cooling schemes and various changing operational conditions is carried out in chapter 4. On the one hand, this study will investigate the influence of the ventilation schemes on the end winding cooling and, on the other hand, the enormous amount of flow data serves as the basis for an approximate heat transfer model (HTM) of the HTC at the end winding bars. As mentioned in section 1.1, due to the high cost of temperature and flow measurements in hydro generators, it is important to determine the HTC by using CFD results. The definition of the estimation model is the most important aim of this thesis and follows in chapter 5, where the HTM will be described.

The validation of the HTM is presented in chapter 6 by a comparison of temperature measurements at the bars of different hydro generators with results of heat conduction computations. This will show the reliability, accuracy and usability of the approximate model for lumped parameter thermal networks. Finally, a conclusion summarizes the main points of this work.

## 2 Fundamentals

### 2.1 Synchronous generators

This section presents the basic characteristics and design details of the cooling system for synchronous machines in power plants. Further technical details like the principle of operation, the revolving magnetic field or the torque generation of synchronous machines are extensively described in the textbooks [6], [7] or [33]. However, first of all some details have to be clarified to limit the research topic and scopes.

The main field of application of synchronous machines is the generator mode with a nominal power up to 1500 megavolt-amperes. However, synchronous motors are used in pumped-storage water plants as well. A further feature for the classification of synchronous machines is the pole construction. On the one hand, hydro generators have a salient pole and normally operate in hydroelectric power plants and, on the other hand, turbogenerators have a cylindrical-rotor and operate in thermal power plants often with a higher rotational speed. Figure 2.1 illustrates the two different design variants. The left figure shows a schematic sketch of a salient 4-pole machine and the right one a 2-pole cylindrical-rotor generator with their main components. The rotor windings of the turbogenerator are placed in slots along two-thirds of the circumference. As a result, the distribution of the current and the magnetic flux density in the air gap are approximately sinusoidal. The pole winding of the salient pole machine is wound around the pole shoe. The stator, pole shoes and poles are built of laminated iron blocks. Additionally, the stator and the rotor have radial ventilation ducts between the iron sheets [34]. A salient pole machine has a low rotor

speed (100 rpm to 1500 rpm) and hence the number of poles is higher to attain the required frequency. A typical number of poles is 4 to 80. A turbogenerator has a rotational speed of 1500 rpm to 3000 rpm and the number of poles is usually 2 or 4.

The distinction regarding the rotor shape is very important for the cooling of synchronous machines because the thermal behaviour and the flow through the machine, especially in the pole region, differ substantially for the two designs. Therefore, a third aspect for classification is the choice of the cooling system and the appropriate media. This thesis investigates only large hydro generators which are typically air cooled machines with salient poles and have a nominal power in the range of 40 – 400 megawatts.

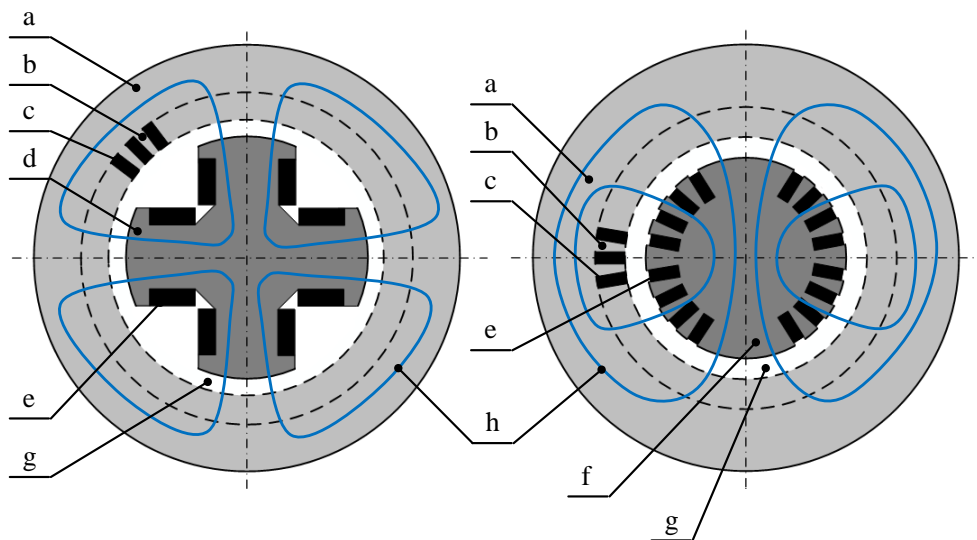


Figure 2.1: Basic design of a synchronous machine [34]: left: salient pole machine, right: cylindrical-rotor machine. Main components: a) stator yoke, b) stator teeth, c) stator slots with winding, d) rotor pole shoe, e) rotor excitation winding, f) rotor pole, g) air gap, h) magnetic field.

### 2.1.1 Design of large hydro generators

The modelling and pre-processing for numerical fluid dynamics computations generally use simplified geometries or surfaces and further assumptions to create a simple model. This also applies to electrical machines like hydro generators. The basic elements are the rotor with the shaft, pole shoes, excitation windings and fans, if the generator is cooled by a shaft mounted ventilation system. The stator core and the stator windings are the important stationary parts. The housing around the stator and the end winding bars serves to ensure an optimal cooling by guiding the air through the machine. Figure 2.2 shows a fragmented generator with these essential

parts. This example is an 8-pole machine with a radial fan as a cooling system. Elements with less relevance for CFD computations, like the bearing system, external ventilation equipment and heat exchanger or the frontal connections are not included in this figure. The fan model is also not considered for these investigations because the geometry of the blades changes with the volume flow rate, the rotational speed and the fluid velocities. This would cause a geometry adaptation for every different ventilation scheme and respective inlet boundary conditions and increase the modelling effort. Furthermore, the number of elements would substantially increase, too. These assumptions and simplification are valid for all investigated ventilation schemes listed in Table 3.1 in section 3.1.

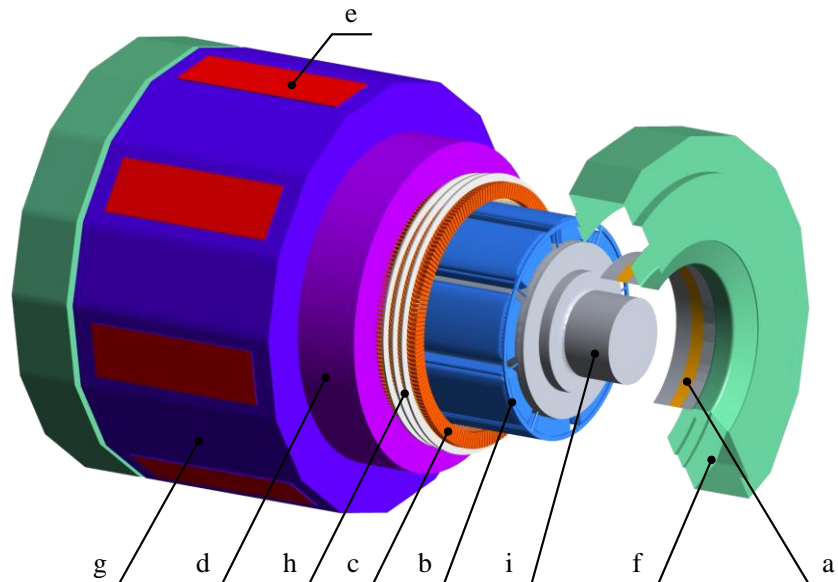


Figure 2.2: Large hydro generator with a radial fan and the main components for a CFD computation: a) boundary inlet, b) salient pole, c) end winding bars, d) stator ducts, e) boundary outlet, f) frame inlet, g) frame outlet, h) support rings, i) shaft.

### 2.1.2 Heating and Cooling

The heating of particular components during operation has a crucial impact on the reliability, durability and efficiency of the hydro generator. Therefore, acceptable temperatures and temperature limits for large salient pole hydro machines have been defined in [35]. Experience and laboratory measurements have shown that high temperatures lead to a degradation of the insulation and of other materials which, in turn, influences the mechanical and electrical loads. Hence, two strategies emerge, enabling the optimization of durability and efficiency. On the one hand, improvements of the thermal and mechanical characteristics of the used materials and, on the other hand, the appropriate choice of the cooling and ventilation scheme, largely influencing the thermal behaviour [3]. However, the machine losses and, consequently, the heat sources have to be determined first. To this end, Figure 2.3 gives an overview of the energy flow in an electrical machine.

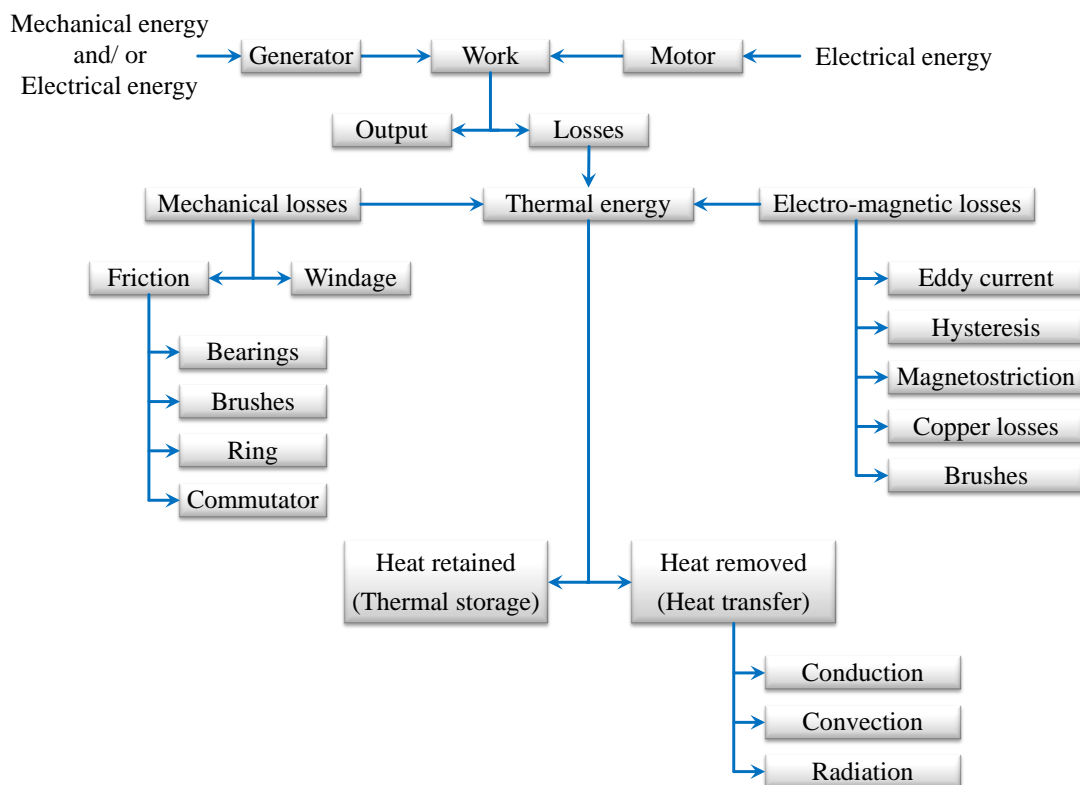


Figure 2.3: Energy flow diagram of an electrical machine [8].

### 2.1.3 Machine losses

Despite the fact that large synchronous machines have a very high efficiency, the nominal power loss is still in the range of several megawatts. Consider, for example, a large hydro generator with a nominal power of 400 megawatts and an efficiency of 98%. The resulting power loss amounts to 8 megawatts corresponding to the power of two wind turbines [7]. These losses are largely converted into heat and have to be dissipated. The following types of losses emerge in a synchronous generator:

- Stator winding loss
- Rotor winding loss
- Stator core loss
- Stray load loss
- Excitation system loss
- Friction and windage loss
- Ventilation and cooling loss

The conversion of the losses into heat in the various components of a machine is described in more detail in [8] or [35].

## 2.2 Fluid dynamics

### 2.2.1 Introduction

Fluid dynamics is the study of the behaviour of fluids in motion and the subsequent effects of the fluid on boundaries which may be forces on solid surfaces or interfaces with other fluids. A fluid can be gaseous or liquid and hence fluid dynamics has a wide range of applications. This section presents the most important basics of fluid dynamics and further recommended literature can be found in textbooks [36-41].

The definition of a fluid is provided by the classic problem of a flow between two plates. The lower plate is fixed and the upper one is moving steadily with the velocity  $u_p$ . The fluid has a no-slip condition at the surfaces and moves with the upper plate. Due to this motion, the fluid elements are displaced by shear forces.

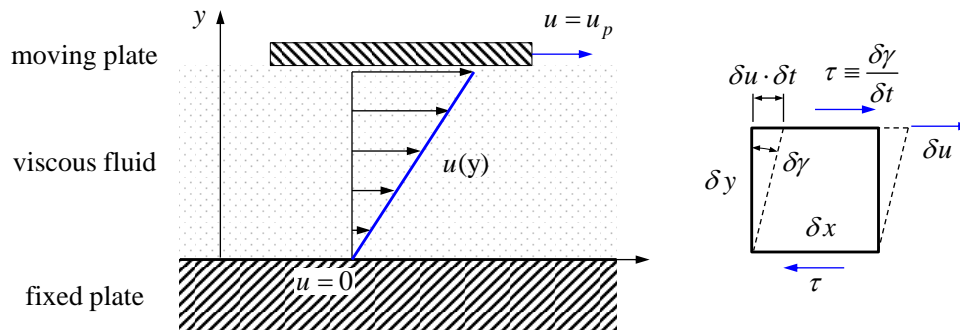


Figure 2.4: Viscous flow between two plates [37].

The shear stress in planes parallel to the plates is constant since the plate does not accelerate and no pressure variation in the flow direction is assumed. The relation between the shear strain rate and the velocity gradient for infinitesimal changes  $\delta$  is

$$\tau \equiv \frac{\delta \gamma}{\delta t} = \frac{\delta u}{\delta y} . \quad (2.1)$$

The shear (dynamic) viscosity  $\mu$  is the constant of proportionality for the linear relationship in (2.1):

$$\tau(y) = \mu \cdot \frac{du}{dy} \quad (2.2)$$

Accordingly, the shear stress depends on the velocity gradient and the viscosity is a thermodynamic property which varies with pressure and temperature [37].

## 2.2.2 Basic equations of continuum mechanics

### 2.2.2.1 Continuity equation

The axiom of continuity of mass assumes that mass is conserved and cannot be produced or destroyed in a closed fluid system. The law of conservation can be written in the differential form

$$\frac{\partial \rho}{\partial t} + (\nabla \cdot \rho \vec{v}) = 0 \quad (2.3)$$

with the density  $\rho$  and the velocity vector

$$\vec{v} = \begin{pmatrix} u \\ v \\ w \end{pmatrix}. \quad (2.4)$$

Liquids are assumed to be incompressible for technically relevant cases, since their compressibility is negligible in contrast to gases. This simplification leads to the reduced continuity equation for incompressible media:

$$\nabla \cdot \vec{v} = 0 \quad (2.5)$$

or, written in Cartesian coordinates:

$$\frac{\partial u}{\partial x} + \frac{\partial v}{\partial y} + \frac{\partial w}{\partial z} = 0, \quad (2.6)$$

see also [37] and [41].

### 2.2.2.2 Momentum equation

The rate of change of the momentum of a body is the sum of all surface and volume forces. The derivation of the momentum axiom is shown here for a tetrahedral control volume of a continuum as depicted in Figure 2.5.

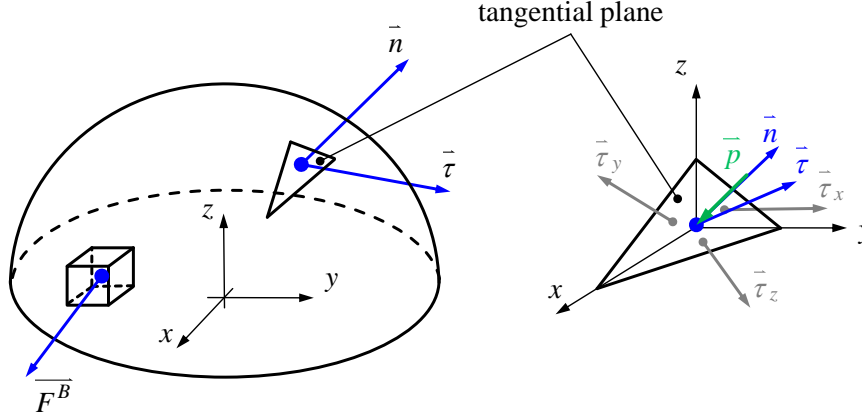


Figure 2.5: Depiction of the volume and surface forces.

The axiom of conservation of the momentum is generally written as

$$\int_V \frac{\partial}{\partial t} (\rho \bar{v}) dV + \int_S \rho \bar{v} (\bar{v} \cdot \bar{n}) dS = \sum \bar{F} . \quad (2.7)$$

The left hand side of the equation is the change of momentum of the control volume plus the momentum flux on the surface and the right hand side is the sum of all volume and surface forces. The volume forces  $\bar{F}^B$  are centrifugal forces, Lorenz forces or the gravitational force. The surfaces forces on the tetrahedral control volume occur in the form of pressure and tension forces [41]. The force balance for the control volume is defined in vector form as

$$\bar{\tau} \cdot A = \bar{\tau}_x \cdot A_{yz} + \bar{\tau}_y \cdot A_{xz} + \bar{\tau}_z \cdot A_{xy} \quad (2.8)$$

with the shear stress vectors  $\tau$ ,  $\tau_x$ ,  $\tau_y$ ,  $\tau_z$  and the appropriate surfaces  $A$ ,  $A_{xy}$ ,  $A_{xz}$ ,  $A_{yz}$ . The surfaces on the right hand side of equation (2.8) can be expressed with the aid of the normal vector  $\bar{n}$  of the surfaces hence, instead of (2.8), we can write

$$\bar{\tau} = \bar{\tau}_x \cdot n_x + \bar{\tau}_y \cdot n_y + \bar{\tau}_z \cdot n_z . \quad (2.9)$$

The matrix representation of this balance equation leads to

$$\bar{\tau} = \underbrace{\begin{pmatrix} \sigma_{xx} & \tau_{yx} & \tau_{zx} \\ \tau_{xy} & \sigma_{yy} & \tau_{zy} \\ \tau_{xz} & \tau_{yz} & \sigma_{zz} \end{pmatrix}}_{\text{shear stress tensor}} \cdot \begin{pmatrix} n_x \\ n_y \\ n_z \end{pmatrix} \quad (2.10)$$

where the diagonal elements are the normal stresses  $\sigma_{ii}$  and the non-diagonal elements the shear stresses  $\tau_{ij}$ . The hydrostatic pressure  $\bar{p}$  on the tangential plane is always perpendicular to the plane and the magnitude of  $p$  is independent of the normal vector. The pressure can be separated from the normal stresses as

$$\sigma_{xx} = -p + \tau_{xx}, \quad \sigma_{yy} = -p + \tau_{yy} \quad \text{and} \quad \sigma_{zz} = -p + \tau_{zz}. \quad (2.11)$$

By combining (2.10) and (2.11) as

$$\bar{\tau} = -p \cdot \begin{pmatrix} n_x \\ n_y \\ n_z \end{pmatrix} + \begin{pmatrix} \tau_{xx} & \tau_{yx} & \tau_{zx} \\ \tau_{xy} & \tau_{yy} & \tau_{zy} \\ \tau_{xz} & \tau_{yz} & \tau_{zz} \end{pmatrix} \cdot \begin{pmatrix} n_x \\ n_y \\ n_z \end{pmatrix}, \quad (2.12)$$

the balance equation can be written in vector notation as

$$\bar{\tau} = -p \cdot \bar{n} + \bar{\tau}_x \cdot n_x + \bar{\tau}_y \cdot n_y + \bar{\tau}_z \cdot n_z. \quad (2.13)$$

The momentum equation can be appended by these surface forces leading to the integral form

$$\int_V \frac{\partial}{\partial t} (\rho \bar{v}) dV + \int_S \rho \bar{v} (\bar{v} \cdot \bar{n}) dS = \int_S -p \cdot \bar{n} dS + \int_S \bar{\tau}_x \cdot n_x dS + \int_S \bar{\tau}_y \cdot n_y dS + \int_S \bar{\tau}_z \cdot n_z dS + \int_V \rho \cdot \bar{f}^B dV \quad (2.14)$$

where  $\bar{f}^B$  is the acceleration of a volume body which can be in the special case the earth gravitational acceleration  $\bar{g}$ .

In differential form for all three Cartesian coordinates, this is written as [41]:

$$\begin{aligned}
 x: \quad \frac{\partial(\rho u)}{\partial t} + (\nabla \cdot \rho u \bar{v}) &= -\frac{\partial p}{\partial x} + \frac{\partial \tau_{xx}}{\partial x} + \frac{\partial \tau_{yx}}{\partial y} + \frac{\partial \tau_{zx}}{\partial z} + \rho \cdot f_x^B \\
 y: \quad \frac{\partial(\rho v)}{\partial t} + (\nabla \cdot \rho v \bar{v}) &= -\frac{\partial p}{\partial y} + \frac{\partial \tau_{xy}}{\partial x} + \frac{\partial \tau_{yy}}{\partial y} + \frac{\partial \tau_{zy}}{\partial z} + \rho \cdot f_y^B \\
 z: \quad \frac{\partial(\rho w)}{\partial t} + (\nabla \cdot \rho w \bar{v}) &= -\frac{\partial p}{\partial z} + \frac{\partial \tau_{xz}}{\partial x} + \frac{\partial \tau_{yz}}{\partial y} + \frac{\partial \tau_{zz}}{\partial z} + \rho \cdot f_z^B.
 \end{aligned} \tag{2.15}$$

### 2.2.2.3 Energy equation

The third axiom describes the conservation of energy in a system. The rate of change of the total energy of a volume is equal to the sum of the powers of all external forces, of the transferred heat and of the supplied heat of inner sources. The energy equation for the control volume shown in Figure 2.5 is written as

$$\underbrace{\frac{\partial}{\partial t} e_t}_1 + \underbrace{\nabla \cdot \bar{v} e_t}_2 = \underbrace{\rho (\bar{v} \cdot \bar{f}^B)}_3 - \underbrace{(\nabla \cdot p \bar{v})}_4 + \underbrace{(\nabla \cdot [\tau \cdot \bar{v}])}_5 - \underbrace{(\nabla \cdot \bar{q})}_6 + \underbrace{\bar{q}_S}_7 \tag{2.16}$$

with the total energy

$$e_t = \rho \left( e + \frac{\bar{v}^2}{2} \right). \tag{2.17}$$

The various terms are:

- 1 ... rate of change of the total energy in the infinitesimal control volume
- 2 ... energy transport by convection
- 3 ... power of the volume forces (body forces)
- 4 ... power of pressure forces
- 5 ... power of shear forces
- 6 ... energy transport by conduction
- 7 ... power of inner heat sources

Equation (2.16) has to be rearranged to a general and compact form in order to be used for fluid dynamics calculations including heat transfer. This transformation is described in detail in [37] or [41] and (2.16) finally becomes

$$\rho \frac{dh}{dt} = \frac{dp}{dt} + (\tau \cdot \nabla \bar{v}) - (\nabla \cdot \bar{q}) + \dot{q}_S . \quad (2.18)$$

The part  $\tau \cdot \nabla \bar{v}$  is a dissipation function with the stress tensor matrix  $\tau$  and the velocity gradient  $\nabla \bar{v}$ . The energy equation in the form (2.18) will be used in section 2.3 to describe the thermal energy transport by heat conduction.

### 2.2.3 Turbulent flow

Modelling turbulence in flows or detecting it experimentally is still a great challenge and a crucial task. Osborne Reynolds defined the transition of laminar to turbulent flows making use of his observations of the nature of flow in pipes. Turbulent flows emerge from laminar flows if small disturbances are no longer damped but rather increase in time and space. The essential features of turbulent flows are strong and irregular fluctuating magnitudes of the velocity, pressure or temperature. Figure 2.6 shows a typical unsteady time variation of the flow velocity.

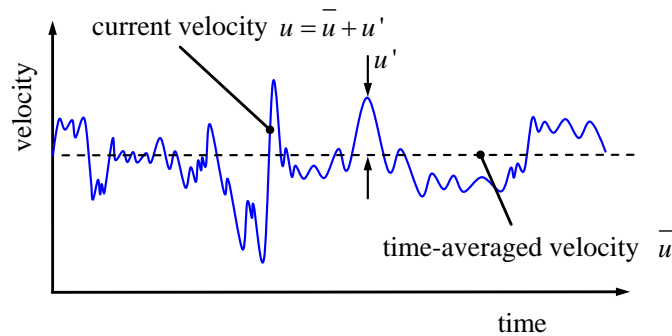


Figure 2.6: Measured velocity of a turbulent flow.

The dimensionless Reynolds number  $Re$  is used to characterize different flow regimes and it is defined as the ratio of the inertial forces to viscous forces which can be written as

$$Re = \frac{\rho \cdot u \cdot L_{char}}{\mu} \quad (2.19)$$

where  $\rho$  is the density,  $\mu$  the dynamic viscosity,  $u$  a reference velocity and  $L_{char}$  a characteristic length. The viscous forces are dominant in laminar flows with low Reynolds numbers and the inertial forces dominate in turbulent flows with high  $Re$  values. It is difficult to define an exact transition between the two conditions,

however, the laminar flow in pipes is limited by  $Re_{crit}=2300$ . A more general representation of ranges is presented in [38] with

$0 < Re < 10^3$ :	laminar
$10^3 < Re < 10^4$ :	transition to turbulence
$10^4 < Re < 10^6$ :	turbulent, moderate $Re$ dependence
$10^6 < Re < \infty$ :	turbulent, slight $Re$ dependence

Further explanations to the turbulence theory and the application of turbulence models in fluid dynamics will follow in subsection 2.4.3.1. Distinguishing between laminar and turbulent flows is crucial for the calculation of flow problems since laminar conditions are governed by the standard Navier-Stokes equations and turbulent flows with the Reynolds-Averaged Navier-Stokes equations.

### 2.2.4 The Navier-Stokes equations for laminar flow

This section presents the derivation of the Navier-Stokes equations for an incompressible medium in laminar flow without heat transport. The continuity and momentum equations of section 2.2.2 have 14 unknown scalar variables ( $\rho, p, u, v, w, \tau_{xx} \dots \tau_{zz}$ ) in 4 equations. The further 10 equations needed are derived in the following.

1. Thermal equation of state [41]:

$$p = p(\rho, T) \quad \text{e.g.: ideal gas} \quad p = \rho \cdot R \cdot T \quad (2.20)$$

$p$  is the pressure,  $T$  the temperature,  $\rho$  the density and  $R$  the ideal gas constant.

2. The viscous stresses are proportional to the element strain rates and the viscosity for a Newtonian fluid [38]. Accordingly, the generalization of (2.2) for an incompressible three-dimensional viscous flow is

$$\begin{aligned} \tau_{xx} &= 2 \cdot \mu \cdot \frac{\partial u}{\partial x}, \quad \tau_{yy} = 2 \cdot \mu \cdot \frac{\partial v}{\partial y}, \quad \tau_{zz} = 2 \cdot \mu \cdot \frac{\partial w}{\partial z} \\ \tau_{xy} &= \mu \cdot \left( \frac{\partial u}{\partial y} + \frac{\partial v}{\partial x} \right), \quad \tau_{yz} = \mu \cdot \left( \frac{\partial v}{\partial z} + \frac{\partial w}{\partial y} \right), \quad \tau_{xz} = \mu \cdot \left( \frac{\partial u}{\partial z} + \frac{\partial w}{\partial x} \right). \end{aligned} \quad (2.21)$$

3. The Boltzmann axiom describes the symmetry of shear stresses to every fluid in motion or rest [41], i.e.

$$\begin{aligned}
\tau_{xy} &= \tau_{yx}, \\
\tau_{xz} &= \tau_{zx}, \\
\tau_{yz} &= \tau_{zy}.
\end{aligned} \tag{2.22}$$

The Navier-Stokes equations will be written for the  $x$ -component of (2.15) as an example. The relations (2.21) and (2.22) are substituted into (2.15) to yield

$$\frac{\partial u}{\partial t} + (\bar{v} \cdot \nabla)u = -\frac{1}{\rho} \frac{\partial p}{\partial x} + \frac{\mu}{\rho} \left[ \frac{\partial^2 u}{\partial x^2} + \frac{\partial^2 u}{\partial y^2} + \frac{\partial^2 u}{\partial z^2} + \frac{\partial^2 v}{\partial x \partial x} + \frac{\partial^2 w}{\partial x \partial z} + \frac{\partial^2 u}{\partial z^2} \right] + f_x^B. \tag{2.23}$$

Using the continuity equation (2.3) further simplifies the equation to

$$\frac{\partial u}{\partial t} + (\bar{v} \cdot \nabla)u = -\frac{1}{\rho} \frac{\partial p}{\partial x} + \frac{\mu}{\rho} \left[ \frac{\partial^2 u}{\partial x^2} + \frac{\partial^2 u}{\partial y^2} + \frac{\partial^2 u}{\partial z^2} \right] + \underbrace{\frac{\mu}{\rho} \frac{\partial}{\partial x} \left[ \frac{\partial u}{\partial x} + \frac{\partial v}{\partial y} + \frac{\partial w}{\partial z} \right]}_{\text{div}u=0} + f_x^B, \tag{2.24}$$

and the Navier-Stokes equation can be hence written as

$$\frac{\partial u}{\partial t} + (\bar{v} \cdot \nabla)u = -\frac{1}{\rho} \frac{\partial p}{\partial x} + \frac{\mu}{\rho} \left[ \frac{\partial^2 u}{\partial x^2} + \frac{\partial^2 u}{\partial y^2} + \frac{\partial^2 u}{\partial z^2} \right] + f_x^B. \tag{2.25}$$

Using the definition of the kinematic viscosity

$$\nu = \frac{\mu}{\rho}, \tag{2.26}$$

the differential momentum equations for a Newtonian fluid with constant density and viscosity are

$$\begin{aligned}
x: \quad \frac{\partial u}{\partial t} + (\bar{v} \cdot \nabla)u &= -\frac{1}{\rho} \frac{\partial p}{\partial x} + \nu \cdot \nabla^2 u + f_x^B, \\
y: \quad \frac{\partial v}{\partial t} + (\bar{v} \cdot \nabla)v &= -\frac{1}{\rho} \frac{\partial p}{\partial y} + \nu \cdot \nabla^2 v + f_y^B, \\
z: \quad \frac{\partial w}{\partial t} + (\bar{v} \cdot \nabla)w &= -\frac{1}{\rho} \frac{\partial p}{\partial z} + \nu \cdot \nabla^2 w + f_z^B.
\end{aligned} \tag{2.27}$$

The combination of the incompressible continuity relation in (2.5) and the three momentum equations in (2.27) have four unknowns ( $p$ ,  $u$ ,  $v$ ,  $w$ ) and they can hence be used to solve laminar flow problems for incompressible Newtonian fluids.

Examples for problems solvable with these equations are a drag flow between two plates or a Hagen–Poiseuille flow in pipes [39, 42].

### 2.2.5 The Reynolds equations for turbulent flow

Every velocity and pressure term in (2.27) is rapidly varying due to the fluctuations occurring in turbulent flows. Using computational resources available nowadays, it is hardly possible to handle such instantaneously fluctuating variables and solve the Navier-Stokes equations numerically. Moreover, time-averaged turbulent values of the flow are sufficiently accurate for most engineering problems and hence the equations in (2.27) are transformed into the Reynolds-averaged Navier-Stokes (RANS) equations for turbulent flows [38, 41].

The turbulent motion shown in Figure 2.6 can be split into a mean velocity  $\bar{u}$  and the fluctuation  $u'$ . The flow variables are hence written as

$$u = \bar{u} + u', \quad v = \bar{v} + v', \quad w = \bar{w} + w', \quad p = \bar{p} + p'. \quad (2.28)$$

The time average value of a turbulent function is given by

$$\bar{u} = \frac{1}{T} \int_0^T u dt \neq 0 \quad (2.29)$$

and the averaged fluctuation has a zero mean value

$$\overline{u'} = \frac{1}{T} \int_0^T u' dt = 0. \quad (2.30)$$

The continuity equation is transformed to time averaged values by substituting the relations in (2.28) into (2.6), reducing the equation to

$$\frac{\partial \bar{u}}{\partial x} + \frac{\partial \bar{v}}{\partial y} + \frac{\partial \bar{w}}{\partial z} = 0. \quad (2.31)$$

The  $x$ -component of the momentum equation (2.27) is rewritten by adding a zero term:

$$\frac{\partial u}{\partial t} + u \frac{\partial u}{\partial x} + v \frac{\partial u}{\partial y} + w \frac{\partial u}{\partial z} + \underbrace{u \left[ \frac{\partial u}{\partial x} + \frac{\partial v}{\partial y} + \frac{\partial w}{\partial z} \right]}_{=0} = -\frac{1}{\rho} \frac{\partial p}{\partial x} + \nu \cdot \nabla^2 u + f_x^B \quad (2.32)$$

and, on rearrangement, the equation becomes [41]

$$\frac{\partial u}{\partial t} + \frac{\partial}{\partial x}(u^2) + \frac{\partial}{\partial y}(uv) + \frac{\partial}{\partial z}(uw) = -\frac{1}{\rho} \frac{\partial p}{\partial x} + \nu \cdot \nabla^2 u + f_x^B. \quad (2.33)$$

The relations in (2.28) are now applied to (2.33) and hence we obtain

$$\begin{aligned} \frac{\partial \bar{u}}{\partial t} + \bar{u} \frac{\partial \bar{u}}{\partial x} + \bar{v} \frac{\partial \bar{u}}{\partial y} + \bar{w} \frac{\partial \bar{u}}{\partial z} + \underbrace{\bar{u} \left[ \frac{\partial \bar{u}}{\partial x} + \frac{\partial \bar{u}}{\partial y} + \frac{\partial \bar{u}}{\partial z} \right]}_{=0} = \\ -\frac{1}{\rho} \frac{\partial \bar{p}}{\partial x} + \nu \cdot \nabla^2 \bar{u} + f_x^B - \frac{\partial}{\partial x} \overline{u'^2} - \frac{\partial}{\partial y} \overline{u'v'} - \frac{\partial}{\partial z} \overline{u'w'}. \end{aligned} \quad (2.34)$$

The three additional inertia terms on the right side can be assumed to be turbulent stresses due to the flow fluctuations. Actually, they are convective acceleration terms but have the mathematical form of stress [39, 42]. The final Reynolds-averaged Navier-Stokes equations in Cartesian coordinates are hence:

$$\begin{aligned} x: \bar{u} \frac{\partial \bar{u}}{\partial x} + \bar{v} \frac{\partial \bar{u}}{\partial y} + \bar{w} \frac{\partial \bar{u}}{\partial z} &= -\frac{1}{\rho} \frac{\partial \bar{p}}{\partial x} + \nu \cdot \nabla^2 \bar{u} + f_x^B - \frac{\partial \overline{u'^2}}{\partial x} - \frac{\partial \overline{v'u'}}{\partial y} - \frac{\partial \overline{w'u'}}{\partial z}, \\ y: \bar{u} \frac{\partial \bar{v}}{\partial x} + \bar{v} \frac{\partial \bar{v}}{\partial y} + \bar{w} \frac{\partial \bar{v}}{\partial z} &= -\frac{1}{\rho} \frac{\partial \bar{p}}{\partial y} + \nu \cdot \nabla^2 \bar{v} + f_y^B - \frac{\partial \overline{u'v'}}{\partial x} - \frac{\partial \overline{v'^2}}{\partial y} - \frac{\partial \overline{w'v'}}{\partial z}, \\ z: \bar{u} \frac{\partial \bar{w}}{\partial x} + \bar{v} \frac{\partial \bar{w}}{\partial y} + \bar{w} \frac{\partial \bar{w}}{\partial z} &= -\frac{1}{\rho} \frac{\partial \bar{p}}{\partial z} + \nu \cdot \nabla^2 \bar{w} + f_z^B - \frac{\partial \overline{u'w'}}{\partial x} - \frac{\partial \overline{v'w'}}{\partial y} - \frac{\partial \overline{w'^2}}{\partial z}. \end{aligned} \quad (2.35)$$

Beside the 4 unknowns ( $\bar{u}$ ,  $\bar{v}$ ,  $\bar{w}$ ,  $\bar{p}$ ) in (2.31) and (2.35), the 6 unknown Reynolds stresses

$$\begin{aligned} \tau'_{xx} &= -\rho \overline{u'u'}, \\ \tau'_{yy} &= -\rho \overline{v'v'}, \\ \tau'_{zz} &= -\rho \overline{w'w'}, \\ \tau'_{yx} &= \tau'_{xy} = -\rho \overline{u'v'}, \\ \tau'_{zx} &= \tau'_{xz} = -\rho \overline{u'w'}, \\ \tau'_{zy} &= \tau'_{yz} = -\rho \overline{v'w'}. \end{aligned} \quad (2.36)$$

need also be described by turbulence models. Turbulence modelling creates a mathematical model to approximate the physical behaviour of turbulent flows and therefore it is one of the key elements in CFD [42]. Modelling turbulent flow and an

introduction of the most important turbulence models will be discussed in subsection 2.4.3.

### 2.2.6 Boundary layer theory

The boundary layer problem is a special layout in fluid dynamics where the friction has a large influence on the flow near walls. An important contribution to the boundary layer theory was made by Ludwig Prandtl who identified the influence of viscosity in flows with large Reynolds numbers and simplified the Navier-Stokes equations by introducing an order of magnitude analysis for this case [43]. This large and extensive theory is described accurately and with all details and applied cases in [40]. A short introduction is given here for the example of a two-dimensional flow with a small viscosity along a flat plate in the following.

The boundary layer theory implies that a flow with high Reynolds numbers is divided into two unequally large zones. The major flow is in the free stream with a negligibly small viscosity. However, the viscosity has a large influence on the flow in the thin boundary layer at the wall. Two flow conditions, laminar and turbulent, occur in the boundary layer with a transition zone between them. A general division of the boundary layer is shown in Figure 2.7.

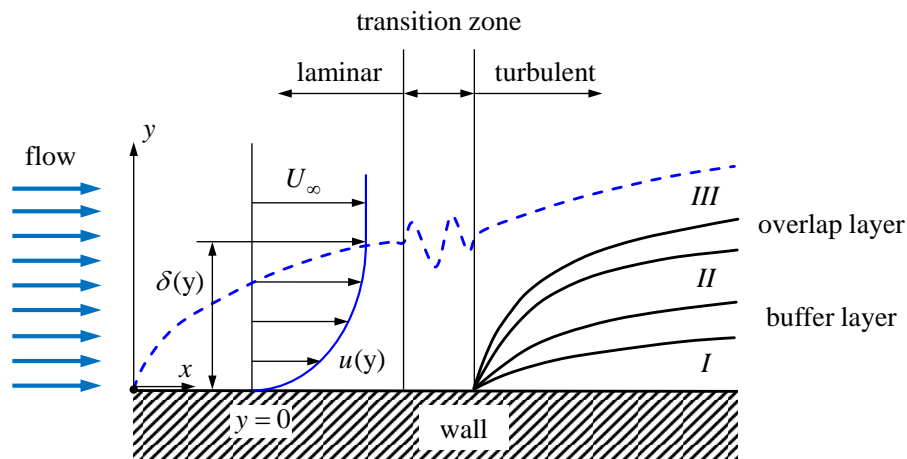


Figure 2.7: Definition of the boundary layer [41].

The flow has a constant velocity distribution in front of the plate. The layer is steadily growing with increasing distance from the leading edge, because a no-slip condition prevails at the wall, i.e. the fluid adheres to the surface, and increasingly more fluid elements are decelerated due to the friction. The assumed thickness of the

boundary layer  $\delta(x)$  increases along the plate. The boundary layer thickness is just a theoretical value, as the transition to the free stream flow is actually continuous [40]. By convention, the limiting distance from the wall is assumed to be  $y$  if

$$u(y) = 0,99 \cdot U_\infty . \quad (2.37)$$

The boundary layer thickness for laminar flow can be estimated by the equilibrium between friction forces (left hand side) and inertial forces (right hand side) per unit volume

$$\mu \cdot \frac{U_\infty}{\delta(x)^2} \sim \frac{\rho \cdot U_\infty^2}{x} . \quad (2.38)$$

The unknown  $x$  in this equation is defined as the exact solution of the equation

$$\frac{\delta_{99}(x)}{L_{char}} = \frac{5}{\sqrt{Re}} \cdot \sqrt{\frac{x}{L_{char}}} , \quad (2.39)$$

see [44] or [40]. The boundary layer decreases with increasing  $Re$  number and disappears at the limit  $Re \rightarrow \infty$ .

As mentioned above, the boundary layer is not laminar along the whole plate. The flow condition changes from laminar to turbulent in the transition zone when the critical length  $x_{crit}$  is reached which corresponds to a Reynolds number of about  $5 \cdot 10^5$  for the flow along a plate.

The turbulent boundary layer is also shown in Figure 2.7. This layer is divided in three sub-sections: viscous sub-layer (I), turbulent inner (II) and outer layer (III) which are important for the different wall function models presented in section 2.4.4 [41]. The basis for the calculation of the near wall velocity is the law of the wall. This approach can be derived by the mixing length hypothesis of Prandtl [45] which assumes a simplified model for the turbulent fluid motion of fluid particles merging into lumps and moving as a unit. It describes the momentum transfer by turbulent Reynolds stresses in the boundary layer as

$$\tau_{xy} = \rho \cdot l_{mix}^2 \cdot \left| \frac{d\bar{u}}{dy} \right| \cdot \frac{d\bar{u}}{dy} . \quad (2.40)$$

The mixing length  $l_{mix}$  is a distance in the  $y$  direction in which the lumps retain their  $x$ -directed momentum [42]. The mixing length is chosen to be proportional to  $y$  since the Reynolds stresses must vanish at the wall:

$$l_{mix} = \kappa \cdot y. \quad (2.41)$$

This choice is also made for dimensional reasons because, near to walls but outside the viscous sub-layer, all physically relevant lengths must be proportional to  $y$ . Furthermore, the shear stresses at the wall are constant and defined with the aid of the friction velocity  $u_\tau$  as

$$\tau_{xy} = \tau_w = \rho \cdot u_\tau^2. \quad (2.42)$$

Using (2.40), the mixing length model leads to

$$u_\tau = \kappa \cdot y \cdot \frac{d\bar{u}}{dy} \quad (2.43)$$

which can be integrated to obtain the velocity profile of the logarithmic law of the wall outside the viscous sublayer:

$$\frac{\bar{u}}{u_\tau} = \frac{1}{\kappa} \ln(y) + C \quad (2.44)$$

where  $\kappa$  is the von Karman constant and  $C$  is assumed to be

$$C = \frac{1}{\kappa} \ln\left(\frac{u_\tau}{\nu}\right) + B. \quad (2.45)$$

This results in a non-dimensional notation of the logarithmic law of the wall [46]

$$u^+ = \frac{1}{\kappa} \ln(y^+) + B \quad (2.46)$$

$$\text{with } \kappa = 0.41, B = 5.5, u^+ = \frac{\bar{u}}{u_\tau} \text{ and } y^+ = y \frac{u_\tau}{\nu}. \quad (2.47)$$

The velocity near the wall resulting from the mixing length model is shown in Figure 2.8. The logarithmic law of the wall is only valid in the fully turbulent zones beginning with  $y^+ > 30$ . A linear relation between the non-dimensional distance of the wall  $y^+$  and the non-dimensional velocity  $u^+$  can be assumed in the viscous sub-

layer near the wall ( $0 \leq y^+ \leq 5$ ). The buffer layer is a transition zone between the logarithmic and viscous zone in the range of  $5 < y^+ < 30$  [37].

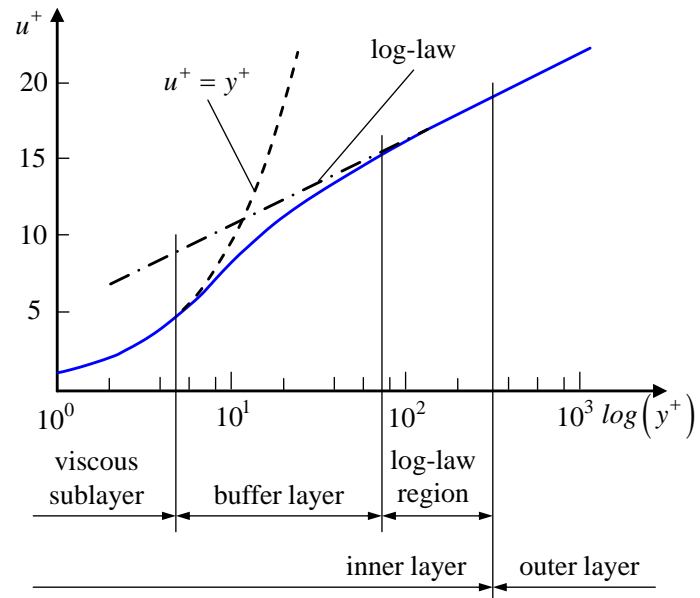


Figure 2.8: Velocity near the wall with the mixing length model.

## 2.3 Heat transfer

The heat exchange between two systems with different temperatures is governed by the physical laws of heat transmission. Thermodynamics describe the supply and dissipation of heat flux and heat in a system. However, the conversion of energy in heat and its transfer are not considered. This mechanism is governed by heat transfer theory connecting thermodynamics and fluid dynamics. For example, a generator is divided into a classical thermodynamic model and a heat transmission model in Figure 2.9.

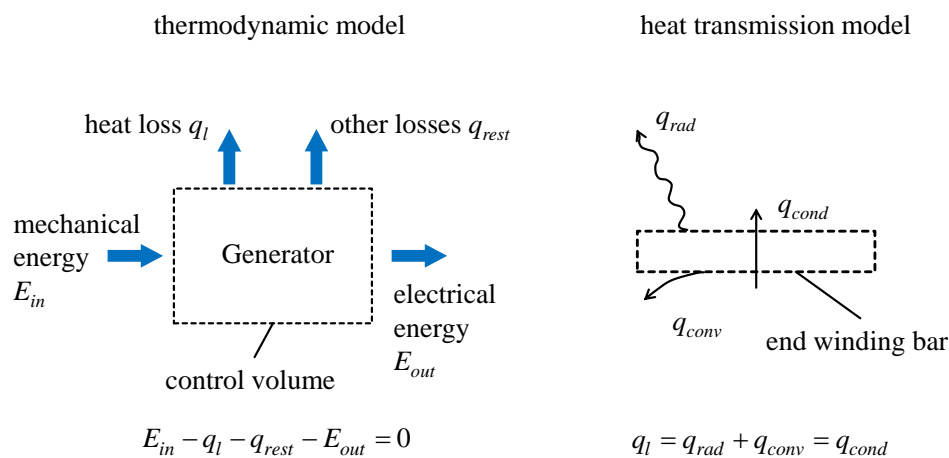


Figure 2.9: Comparison of a thermodynamic model to a heat transmission model.

$q_{cond}$  ... conductive heat flux,  $q_{conv}$  ... convective heat flux,  $q_{rad}$  ... radiative heat flux

The conductive and convective modes of heat transfer are described in the following subsections. The radiation of heat is negligibly small in electrical machines however; a short introduction is given in Appendix B.

### 2.3.1 Heat conduction

Heat conduction is the molecular heat transfer in a solid, liquid or gaseous medium. The heat is always transferred from a higher temperature level to a lower one and, therefore, the existence of a temperature gradient is essential for heat conduction. The propagation of heat is fundamentally described by equation (2.18) whereby the parts  $dp/dt$  and  $\tau \cdot \nabla \vec{v}$  are zero for systems in rest and solids and, hence, the energy equation leads to the simpler form

$$\rho \frac{dh}{dt} = -(\nabla \cdot \vec{q}) + \dot{q}_S . \quad (2.48)$$

With the differential change of the enthalpy expressed with temperature

$$dh = c_p \cdot dT \quad (2.49)$$

and the law of Fourier [4]

$$\dot{q} = -\lambda \cdot \nabla T \quad (2.50)$$

follows the temperature formulation of the heat conduction equation:

$$\rho \cdot c_p \cdot \frac{\partial T}{\partial t} = \nabla \cdot (\lambda \nabla T) + \dot{q}_S \quad (2.51)$$

with the assumption of constant fluid properties (thermal conductivity  $\lambda$ , specific heat capacity  $c_p$  and density  $\rho$ ).

The thermal conductivity characterizes the ability of a medium to transport heat by the motion of atoms. It depends on temperature and, especially for gases, on pressure. For isotropic media it has the same values in each direction. However, a composite or laminated solid consists of two or more materials with different thermal conductivities which may lead to anisotropy. In such cases, a combined thermal conductivity may be used to simplify the heat conduction calculations [41]. Table 2.1 shows the thermal conductivities for some isotropic materials.

Material	Thermal conductivity $\lambda$ [W / m K]
Copper (pure)	401
Aluminium (pure)	236
Steel (13CrMo4)	46
Water	0.562
Polyamide	0.320
Epoxy resin	0.200
Ethanol	0.174
Particle board	0.170
Hydrogen	0.169
Air	0.024

Table 2.1: Thermal conductivity of some solids, liquids and gases at 0°C and 1 bar [5].

Equation (2.51) has been adjusted for this work since the heat conduction computations are steady-state and the solid domain of the end winding bars consists of a composite material with copper, coating and insulation. Hence, (2.51) can be written with an anisotropic thermal conductivity as

$$0 = \nabla \cdot (\overline{\lambda} \nabla T) + \dot{q}_S \quad (2.52)$$

where  $\overline{\lambda}$  is the conductivity tensor.

The stator bars are actually a composite material built up of copper conductors of small cross section, of the coating and of the insulation. As shown in Figure 2.10a, a stator bar can include a large number of conductors in horizontal as well as in vertical direction which leads to a composite material with overall anisotropic properties. The thermal conductivity of this composite material (copper plus coating) changes substantially in each direction and modelling each conductor separately would lead to overly high computational effort. Using a homogenized bar model saves computation time and the detailed modelling of all conductors is not necessary. Figure 2.10b shows the homogenized bar model for the simulations.

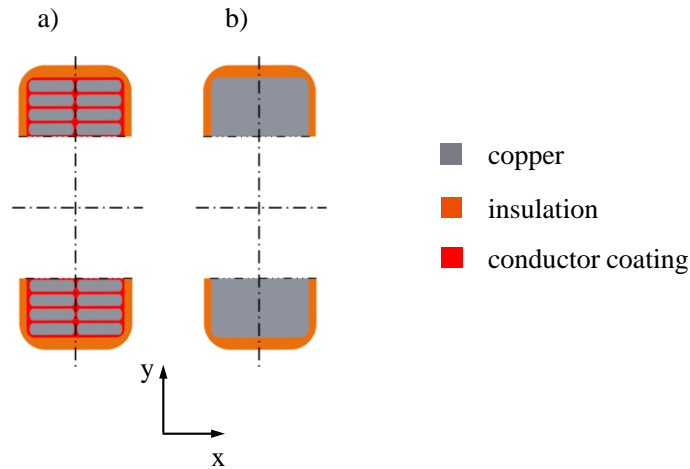


Figure 2.10: a) real bar structure, b) homogenized structure.

The anisotropy can be considered by calculating an equivalent thermal conductivity for each axis  $\lambda_x$ ,  $\lambda_y$  and  $\lambda_z$  (see technical report [47]). The thermal conductivity of the insulation has been assumed constant in all coordinate directions.

### 2.3.2 Heat convection

In general, convection is the transport of a physical quantity by macroscopic motion in a fluid. On the one hand, heat is conducted through a medium due to the temperature gradient and on the other hand energy flows in the form of enthalpy and kinetic energy as a result of the fluid motion. Therefore, the convective heat transport in a fluid is a superposition of heat conduction and of energy transport by the flow. Two forms of convection are distinguished in literature. The free or natural convection is the result of fluid motion by temperature and density differences. In forced ventilated electrical machines free convection is of less significance, for details, see [48]. Forced convection occurs, if the fluid motion is generated by an applied pressure gradient due to an external source. Such an external source can be a fan, a pump or some other suction device [41]. Heat transfer by forced convection is more important for engineering problems and will be described below for a heated static plate shown in Figure 2.11.

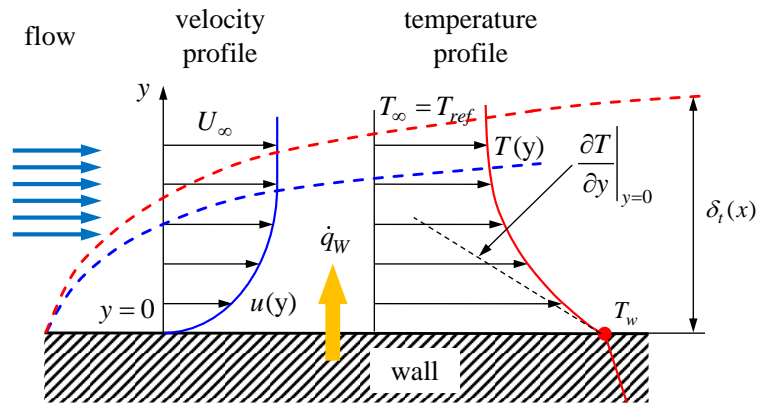


Figure 2.11: Temperature and velocity distribution at a heated surface [49].

The flow streams parallel to the plate. The velocity near the wall changes from zero to the free stream velocity  $U_\infty$  and the temperature decreases from the wall temperature  $T_w$  to the reference temperature  $T_\infty$  in the free stream. This transition happens in the small thermal boundary layer near the wall (see subsection 2.2.6). The ratio of the thicknesses of the velocity boundary layer  $\delta(x)$  and the temperature boundary layer  $\delta(x)_t$  is proportional to the Prandtl number [39]:

$$\frac{\delta(x)}{\delta(x)_t} \sim \sqrt{Pr}. \quad (2.53)$$

The Prandtl number  $Pr$  is a dimensionless number for fluids and describes the ratio of the kinematic viscosity to the thermal conductivity:

$$Pr = \frac{\mu \cdot c_p}{\lambda}. \quad (2.54)$$

Hence,  $Pr$  is temperature and pressure dependent. The Prandtl number of air is about 0.72 ( $p=1$  bar,  $T=0^\circ\text{C}$ ).

Newton's law of cooling characterizes the convection process by the expression

$$\dot{q}_w = \alpha \cdot (T_w - T_\infty) \quad (2.55)$$

where  $\dot{q}_w$  is the convective wall heat flux and  $\alpha$  the convective wall heat transfer coefficient (HTC). The wall heat flux  $\dot{q}_w$  at  $y=0$  is defined by (2.50) as

$$\dot{q}_w = -\lambda \cdot \left. \frac{\partial T}{\partial y} \right|_{y=0} \quad (2.56)$$

and the combination of (2.55) and (2.56) yields the definition of the heat transfer coefficient (HTC):

$$\alpha = \frac{-\lambda \cdot \left. \frac{\partial T}{\partial y} \right|_{y=0}}{T_w - T_\infty}. \quad (2.57)$$

The HTC depends on conditions in the boundary layer such as the surface geometry and roughness, the fluid properties and thermodynamics, the thermal boundary conditions at the surface as well as the level of turbulence of the flow. Particularly turbulent boundary layers can hardly be analyzed exactly and, hence, the introduction of the HTC enables a simple formulation. Table 2.2 presents the range of the coefficient for different convection modes.

Process	HTC $\alpha$ [W / m <sup>2</sup> K]
Free convection	
Gases	2 – 25
Liquids	50 – 1000
Forced convection	
Gases	25 – 250
Liquids	100 – 20.000
Convection with phase change	
Boiling or condensation	2.500 – 100.000

Table 2.2: Typical values of the convective heat transfer coefficient [48].

Many empirical formulas for the prediction of the convective heat transfer along various surfaces have been defined in the technical literature on heat transfer. Such formulas usually describe correlations between non-dimensional quantities like the Reynolds ( $Re$ ), Grashof ( $Gr$ ), Taylor ( $Ta$ ), Prandtl ( $Pr$ ) and Nusselt ( $Nu$ ) numbers. The dimensional analysis combines several variables into dimensionless groups to simplify the interpretation and extend the range of application of experimental data. Generally, dimensionless numbers transport more information than empirical coefficients [49]. Assuming that  $\alpha$  is known for a certain heat transfer problem (e.g. a pipe with water), the wall heat flux can be calculated from the given temperature difference. This statement is only valid for the specific pipe with the diameter  $D^*$  and water with the thermal conductivity  $\lambda$ . For other diameters and fluid conditions, the HTC have to be determined again. However, the Nusselt number connects  $\dot{q}_w$ ,  $\Delta T$ ,  $D^*$  and  $\lambda$  and thus extends the information content and, therefore, the applicability.

The dimensionless Nusselt number is generally based on the HTC and includes a characteristic length of the geometry  $L_{ref}$  and the thermal conductivity  $\lambda$  of the fluid:

$$Nu = \alpha \cdot \frac{L_{ref}}{\lambda}. \quad (2.58)$$

Using the dimensional analysis, the Nusselt number can also be written as a function of the Reynolds and Prandtl numbers as well as a spatial variable  $x^*$ :

$$Nu = f(x^*, Re, Pr). \quad (2.59)$$

This function has the advantage of enabling the computation of  $Nu$  for different fluids and for different geometries. Moreover, from the local Nusselt number, an

average value of  $\overline{Nu}$  can be obtained by integrating over the surface of the solid to make it independent of  $x^*$  [49]:

$$\overline{Nu} = f(Re, Pr). \quad (2.60)$$

Accordingly, the relationship between the wall heat transfer coefficient and the flow conditions for a particular geometry are characterized by dimensionless numbers. The equations are more useful for engineering problems although, in practice, the conditions vary according to free stream turbulence and surface roughness [48]. Therefore, the Nusselt number formula is extended to include further non-dimensional parameters  $\Pi_i$  representing various physical properties (length, time, velocity, fluid properties, ...):

$$Nu = f(Pr, Re, \Pi_1, \Pi_2, \Pi_3, \dots). \quad (2.61)$$

The correlation with  $Re$  is used in conjunction with forced convection problems, however, for natural convection, the typical correlated quantity is the Grashof number  $Gr$ . The convective heat transfer is often represented by an algebraic expression of the form

$$Nu = a \cdot Pr^b \cdot Re^c \cdot \Pi_i^n \cdot \dots \quad (2.62)$$

The constant  $a$  and the exponents ( $b, \dots, n$ ) can be identified by comparing the values obtained from such an equation with measured data or numerical results. A similar formulation is used for flat plates, pipes, cylinders, heat exchangers, etc. in [5, 49] and the fundamentals and the derivation of such correlations are presented in [48].

A number of authors have investigated the heat transfer for special geometries (e.g. pipes, plates, heat exchanger systems ...) and flow conditions (laminar, turbulent) and found expressions for the Nusselt number [5]. For example, the heat transfer in a pipe with a constant wall temperature and laminar flow is found in [5] to be

$$Nu = 1.077 \cdot \left( Re \cdot Pr \cdot \frac{D^*}{x^*} \right)^{1/3}. \quad (2.63)$$

Some special heat transfer correlations for electrical machines have been investigated by several authors in the past. The HTC at the end winding bars of a small electrical motor has been formulated in many publications [8, 12, 50, and 51] as

$$\alpha = k_1 \cdot \left[ 1 + k_2 \cdot v^{k_3} \right] \quad (2.64)$$

where  $\alpha$  is the HTC,  $v$  the local fluid velocity and  $k_1$ ,  $k_2$  and  $k_3$  are constants. The heat transfer in the air gap of such a machine has been correlated in [50] to the Taylor number

$$Nu = a \cdot Ta^b \cdot Pr^c . \quad (2.65)$$

The authors of [52] have used dimensional analysis and the  $\Pi$ -theorem to find an approximate formula for the end winding bars:

$$Nu = \Pi_1^{q_1} \cdot \Pi_2^{q_2} \cdot \Pi_3^{q_3} \cdot \Pi_4^{q_4} \cdot q_5 \quad (2.66)$$

where  $\Pi_i$  are Reynolds numbers in several control surfaces between the two bars or a bar and the guiding and  $q_i$  are constants.

A further detailed investigation of three heat transfer correlations has been carried out in [30] for the rotor pole, the rotor slots and the stator. Measurements on a complex annular channel with an inner rotating wall have generated data for a correlation. The test case under investigation corresponds to the air gap of an open four-pole synchronous motor. The authors have used an integral formulation of the averaged  $Nu$  number at the pole and rotor slot surfaces as well as for the entire rotor with

$$\overline{Nu} = C \int_m^n \int_o^p Nu(\Pi_1, \Pi_2) d\Pi_1 d\Pi_2 \quad (2.67)$$

where  $C$  is a constant and  $\Pi_1$  and  $\Pi_2$  are geometry ratios.

A more simplified procedure has been developed for the pole surfaces of a salient pole generator in [27]. The Nusselt number for the leading and the trailing sides of the poles are defined as

$$Nu_{\text{leading/trailing side}} = C \cdot Re_i^\varepsilon \quad (2.68)$$

where  $C$  and  $\varepsilon$  are constants. The heat transfer at the pole end side is obtained similarly as

$$Nu_{\text{pole end side}} = C_1 \cdot \Pi_i^{\varepsilon_1} + C_2 \cdot Re_i^{\varepsilon_2} \quad (2.69)$$

where  $C_1$  and  $C_2$  are constant coefficients,  $\varepsilon_1$  and  $\varepsilon_2$  are exponents and  $\Pi_i$  is a geometry ratio.

## 2.4 Computational fluid dynamics

The first experimental investigations of fluids have been carried out in the 17<sup>th</sup> century and the theoretical calculations and proofs have followed centuries later. In the last decades, computational fluid dynamics (CFD) has grown to become the third approach in the study and development of fluid mechanics thanks to the fast increase of computational resources. CFD synergistically complements the two other approaches. The major advantages of CFD compared with experimental fluid dynamics are

- the reduction of the design and development time
- the simulation of not reproducible flow conditions in experimental tests
- more detailed and comprehensive information
- increasing cost effectiveness.

The general scope of CFD is the approximate numerical solution of complex fluid dynamic and heat transfer problems. The three fundamental principles of mass, momentum and energy conservation can be expressed in terms of partial differential equations (PDE). Various CFD techniques replace the integrals and partial derivatives in these equations by discretized algebraic forms. These are solved to obtain values for the flow field at discrete points in time and space. This procedure is illustrated in Figure 2.12.



Figure 2.12: Overview of computational solution procedure [53].

This section is restricted to the features of CFD relevant for this thesis and the books [53-56] are recommended for further study.

### 2.4.1 Discretization

The governing equations for fluid dynamics and heat transfer calculations have been introduced in sections 2.2 and 2.3, respectively. These are partial differential equations (PDEs) with first and second order derivatives in the spatial coordinates and first order derivatives in time. The time derivatives appear linearly but the spatial derivatives often have nonlinear coefficients. The PDEs can be converted to a system of algebraic equations with the finite difference (FDM), finite element (FEM) or finite volume method (FVM) to solve them numerically [53]. The FDM uses the conservative form of the PDEs to solve the equations in the mesh nodes. The partial derivatives of the PDEs are substituted by differences making the implementation of the FDM easy and especially effective with higher order methods. However, this discretization type requires a structured mesh, strongly limiting its applicability. The basics of spatial and time discretization will be discussed in Appendix C for a 2-dimensional FDM mesh in order to keep the discussion simple.

The FEM is especially used for the analysis of solids or electromagnetic problems. The method is applied to the weak forms of the boundary value problems of the PDEs and approximates the unknown functions by locally defined low order polynomials.

The FVM discretization exhibits good accuracy for discontinuities and is used for the most CFD codes. The PDEs are given in integral form and the integrals over the volume elements are substituted by sums. The equations are solved either for the values in the centre of the volume element or those at the mesh corners (nodes) [57].

The finite volume method takes full advantage of an arbitrary mesh with a large number of choices for the definition of the control volumes to express the conservation laws. The shape and location of the control volumes with their mesh points and edges as well as the rules for computing the fluxes through the control volumes can be varied. These possibilities make the FVM extremely flexible and hence a vast number of numerical techniques have emerged to solve the PDEs by means of the FVM [56].

The finite volume method will be presented for the general first-order equation (C.17) with the appropriate flux vectors (C.18) - (C.20) where only first derivatives are present and the discussion is hence simple. Figure 2.13 shows a control volume with its reference centre points ( $A, B, C, D$ ).

We integrate (C.17) over the control volume to obtain

$$\int_{ABCD} \left( \frac{\partial \bar{U}}{\partial t} + \frac{\partial \bar{F}}{\partial x} + \frac{\partial \bar{G}}{\partial y} \right) dx dy = 0, \quad (2.70)$$

and by applying the divergence theorem we can write

$$\frac{d}{dt} \int \bar{U} dx dy + \int_B^C \bar{F} dy - \int_D^A \bar{F} dy + \int_A^B \bar{G} dx - \int_C^D \bar{G} dx = 0. \quad (2.71)$$

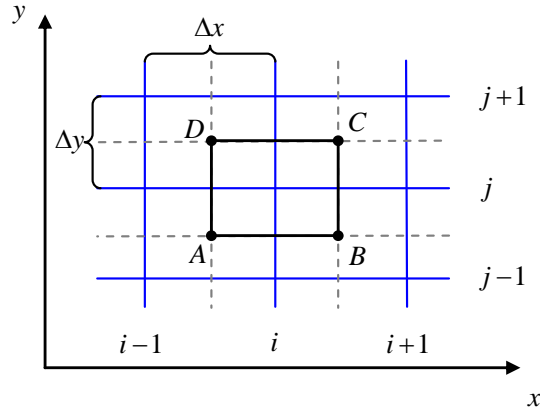


Figure 2.13: Finite volume mesh for discretization.

The integrals in (2.71) can be replaced by the sums of the specific mass fluxes over the elements boundaries:

$$\frac{d}{dt} \sum \bar{U} \Delta x \Delta y + \sum_B^C \bar{F} \Delta y - \sum_D^A \bar{F} \Delta y + \sum_A^B \bar{G} \Delta x - \sum_C^D \bar{G} \Delta x = 0. \quad (2.72)$$

The flux components along the edges ( $\overline{AB}$ ,  $\overline{BC}$ ,  $\overline{CD}$  or  $\overline{DA}$ ) depend on the selected integration scheme. An overview of the different evaluation methods for the fluxes over the control surfaces is given in [56]. For the current discussion we take the method of averaging the fluxes to obtain

$$\Delta x \Delta y \frac{d}{dt} \bar{U}_{i,j} + \frac{1}{2} (\bar{F}_{i,j} + \bar{F}_{i+1,j}) \Delta y - \frac{1}{2} (\bar{F}_{i-1,j} + \bar{F}_{i,j}) \Delta y + \frac{1}{2} (\bar{G}_{i,j-1} + \bar{G}_{i,j}) \Delta x - \frac{1}{2} (\bar{G}_{i,j} + \bar{G}_{i,j+1}) \Delta x = 0. \quad (2.73)$$

The rearrangement of (2.73) results in a second-order central space discretization:

$$\frac{d}{dt} \bar{U}_{i,j} + \frac{(\bar{F}_{i+1,j} - \bar{F}_{i-1,j})}{2\Delta x} + \frac{(\bar{G}_{i,j+1} - \bar{G}_{i,j-1})}{2\Delta y} = 0. \quad (2.74)$$

The described finite volume method has the advantage of good conservation properties and hence, CFD codes usually use the FVM.

### 2.4.2 Common numerical techniques

To deal with any fluid dynamic problem, it is necessary to review the basic equations of fluid dynamics and heat transfer at first. Secondly, it is also important to investigate the various numerical discretization techniques. Finally we will apply the discretization methods discussed to the fluid dynamics and heat transfer equations with the aid of different numerical tools. It would go beyond the scope of this thesis to describe every existing numerical method. Instead, we refer to the textbooks [53], [54] and [55] presenting in depth information and explanations on the common numerical algorithms for the solution of PDEs. In [59], an overview of the techniques and a coarse classification is given:

- Central methods
  - Lax-Wendroff, e.g. [60]
  - Runge-Kutta, e.g. [61]
  - ADI (Alternating direction implicit) , e.g. [62]
- Upwind methods
  - Flux-vector-splitting, e.g. [63]
  - Flux-difference-splitting, e.g. [64]
- High-resolution methods, e.g.
  - Upwind-TVD (Total variation diminishing) , e.g. [65]
  - Central-TVD, e.g. [66]

### 2.4.3 Numerical treatment of turbulent flows

Turbulence is very important for most natural and engineering flows. As mentioned in section 2.2.3, turbulence is characterized by rapid fluctuations of velocity, pressure or temperature. This chaotic nature of turbulence is even today a problem which can only be solved by making approximate assumptions.

The three principal methods to solve the Navier-Stokes equations with turbulence taken into account are the direct numerical simulation (DNS), the large eddy simulation (LES) and the use of the Reynolds-averaged Navier-Stokes (RANS) equations. The selection from among these methods depends particularly on the size of the turbulent vortices. A DNS solves the Navier-Stokes equations exactly without any turbulence model, i.e. all spatial turbulent length scales have to be resolved with an extremely fine grid. The smallest length scale in the energy cascade is described by the Kolmogorov microscales when the kinetic energy of the vortices dissipates into heat [67]. Figure 2.14 shows the decrease of the turbulent vortices for the flow around a cylinder.

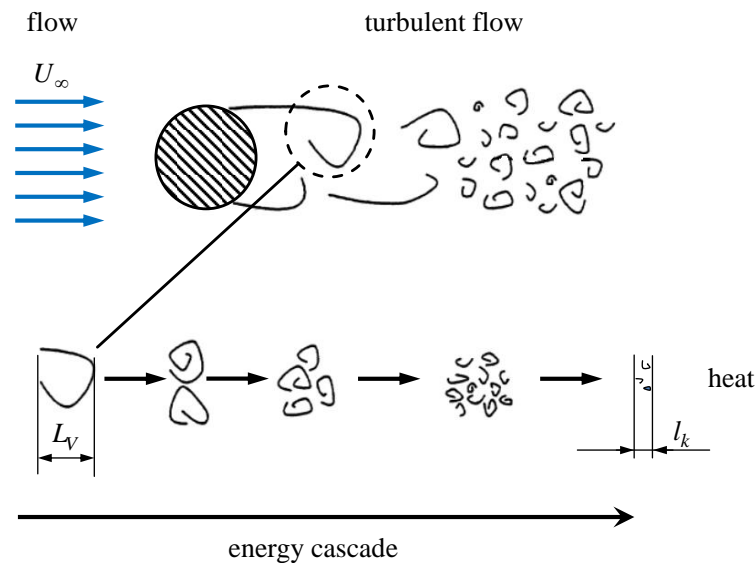


Figure 2.14: Finite volume mesh for discretization.

The spatial Kolmogorov length scale is defined as

$$l_k = \left( \frac{\nu^3}{\varepsilon} \right)^{1/4} \quad (2.75)$$

with the kinematic viscosity  $\nu$  and the turbulent dissipation  $\varepsilon$ . A DNS is nowadays only feasible for simple problems with very low  $Re$  numbers because otherwise the number of elements of the mesh and hence the computation time would increase in an extraordinary way.

The use of the RANS equations in combination with an appropriate turbulence model for a particular engineering case is the state-of-the-art method in fluid dynamics. A turbulence model predicts the effects of turbulence and closes the RANS equations by solving the unknown Reynolds stresses in (2.35). A detailed introduction to turbulence modeling is presented in the subsections below.

The LES connects the DNS and the RANS method. It is an accurate method of simulating turbulent flows in which the large flow structures are computed while small vortices are modelled. Therefore, the smallest mesh element can be much larger than the Kolmogorov length and the time step can be chosen larger than for a DNS. Special subgrid-scale models are based on space-filtered equations to take account of the small eddies, e.g. the Smagorinsky model [68] or the Scale-Adaptive Simulation model [69]. The computational cost for engineering problems is lower than for a DNS but for complex geometries or flow configurations it still very high. Important contributions to LES are presented in [68], [70] and [71].

### 2.4.3.1 Turbulence modelling

Turbulence modelling is a procedure to close the system of mean flow equations in (2.35). Due to the emerging new unknowns by the Reynolds averaging for turbulent flows, the Reynolds stresses have to be additionally expressed. Moreover, it is unnecessary to resolve the details of the turbulent fluctuations for most engineering applications. The accuracy of the numerical solution depends on the complexity of the turbulence model. Turbulence is always unsteady and highly irregular in time and space. Furthermore, the energy is dissipated due to the viscous stresses and a turbulent flow is strongly diffuse. All these properties should be described by any set of equations and relations to determine the unknown variables. Furthermore, a turbulence model should be simple and accurate to have a wide applicability. Indeed, a variety of RANS-based turbulence models have been developed in the last decades. They are coarsely classified as the eddy-viscosity models, Reynolds-stress models (RSM) and LES models (see above) [42].

The eddy-viscosity models are presently the most widely used and validated turbulence models. Their concept is based on the Boussinesq hypothesis stating that the Reynolds stresses can be linked to the mean strain rate of deformation:

$$-\overline{\rho u_i u_j} = \mu_t \cdot \left( \frac{\partial \bar{u}_i}{\partial x_j} + \frac{\partial \bar{u}_j}{\partial x_i} \right) - \frac{2}{3} \rho k \delta_{ij} \quad (2.76)$$

with  $\mu_t$  being the eddy (turbulent) viscosity,  $k$  the turbulent kinetic energy and  $\delta_{ij}$  the Kronecker delta. The subscripts  $i$  and  $j$  correspond to the  $x$  and  $y$  directions, respectively [72, 73]. The Reynolds averaged momentum equation of (2.35) can be written in tensor notation to derive the eddy-viscosity hypothesis as

$$\rho \frac{\partial \bar{u}_i}{\partial t} + \rho \frac{\partial (\bar{u}_i \bar{u}_j)}{\partial x_j} = -\frac{\partial \bar{p}}{\partial x_i} + \frac{\partial}{\partial x_j} \left[ \mu \left( \frac{\partial \bar{u}_i}{\partial x_j} + \frac{\partial \bar{u}_j}{\partial x_i} \right) - \rho \overline{u'_i u'_j} \right] + f_i^B . \quad (2.77)$$

Using the Boussinesq hypothesis, (2.76) and introducing the effective viscosity

$$\mu_{eff} = \mu + \mu_t , \quad (2.78)$$

the momentum equation becomes

$$\rho \frac{\partial \bar{u}_i}{\partial t} + \rho \frac{\partial (\bar{u}_i \bar{u}_j)}{\partial x_j} = -\frac{\partial p'}{\partial x_i} + \frac{\partial}{\partial x_j} \left[ \mu_{eff} \left( \frac{\partial \bar{u}_i}{\partial x_j} + \frac{\partial \bar{u}_j}{\partial x_i} \right) \right] + f_i^B \quad (2.79)$$

with a modified pressure

$$p' = \bar{p} + \frac{2}{3} \rho k \delta_{ij} . \quad (2.80)$$

The tensor notation of the momentum equation (2.79) is used to derive the two-equation turbulence models described below [46, 59].

The central concept of the Reynolds stress models is solving additional transport equations for each of the six independent Reynolds stresses. The isotropic assumption of the eddy viscosity can hence be avoided. The RSM is physically the most complete model and has a good accuracy for complex flows but it is computationally expensive. The exact equation for the transport of the Reynolds stresses is written as

$$\frac{D(\bar{u}_i \bar{u}_j)}{Dt} = P_{ij} + D_{ij} - \varepsilon_{ij} + \Pi_{ij} + \Omega_{ij} . \quad (2.81)$$

The rate of change of the Reynold stresses is equal to the rate of production  $P_{ij}$  plus the transport of diffusion  $D_{ij}$  minus the rate of dissipation  $\varepsilon_{ij}$  plus the transport due to pressure-rate-of-strain tensor  $\Pi_{ij}$  plus the transport due to the rotation  $\Omega_{ij}$  [57, 73].

Some of the most important turbulence models for engineering cases are listed below:

1. Linear eddy viscosity models
  - Algebraic models, e.g. Baldwin-Lomax [74]
  - One-equation models, e.g. Spalart-Allmaras model [75]
  - Two-equation models
    - $k$ - $\varepsilon$  models
      - Standard  $k$ - $\varepsilon$  model, e.g. [76]
      - Realizable  $k$ - $\varepsilon$  model, e.g. [77]
      - RNG  $k$ - $\varepsilon$  model, e.g. [78]
    - $k$ - $\omega$  models
      - Wilcox  $k$ - $\omega$  model [79]
      - SST  $k$ - $\omega$  model [80]
2. Nonlinear eddy viscosity models, e.g.  $v_2$ -f model [81]
3. Reynolds stress model, e.g. [82]

The SST turbulence model has been used for the CFD simulations in this thesis. It is a combination of the  $k$ - $\varepsilon$  model and the  $k$ - $\omega$  model and therefore, the SST model covers a wide range of engineering problems. The  $k$ - $\varepsilon$  and the  $k$ - $\omega$  turbulence models are discussed in more detail in Appendix D.

### 2.4.3.2 SST $k$ - $\omega$ model

The Shear-Stress-Transport turbulence model is the most common model for industrial, commercial and other research codes and was originally developed for aeronautics applications. It uses the  $k$ - $\varepsilon$  model in the free stream outside the boundary layer and the  $k$ - $\omega$  model in the boundary layer to combine their individual benefits. The  $k$ - $\varepsilon$  model calculates too large length scales and, accordingly, the shear stress in adverse pressure gradient flows is over-predicted. It also requires a near-wall modification. Nevertheless, the accuracy and robustness in the free stream away from walls is a significant advantage over the  $k$ - $\omega$  model because the turbulent diffusion has a strong sensitivity in the free stream outside the boundary layer. However, the  $k$ - $\omega$  turbulence model does not need damping functions in the near wall layers and it is more successful for flows with moderate adverse pressure gradients.

The great advantage of the SST model is the reduction of the weaknesses of the  $k$ - $\varepsilon$  and  $k$ - $\omega$  model [83].

The SST model uses the original equations (D.6) and (D.8) of the  $k$ - $\omega$  model and a transformed version of the  $k$ - $\varepsilon$  equations (D.3) and (D.4), where the turbulent dissipation  $\varepsilon$  is replaced by the turbulent diffusion  $\omega$  and an additional cross-diffusion term is added. Equations (D.4) and (D.8) are multiplied with a blending function  $(1-F_1)$  and the corresponding equations of each set are added to result in the  $k$  and  $\omega$  equations of the SST turbulence model. The blending function  $F_1$  is defined as

$$F_1 = \tanh \left\{ \left[ \min \left[ \max \left( \frac{\sqrt{k}}{\beta' \omega y}, \frac{500\nu}{y^2 \omega} \right), \frac{4\rho\sigma_w k}{CD_{k\omega} y^2} \right] \right]^4 \right\} \quad (2.82)$$

and ensures the switching between the  $k$ - $\varepsilon$  and  $k$ - $\omega$  models depending on the distance  $y$  to the wall  $y$  [80]. A detailed derivation of the SST turbulence model is given in Appendix D.

## 2.4.4 Near Wall Treatment

The numerical treatment of the momentum and heat fluxes in near wall regions is an important issue for the accurate prediction of turbulent flows. The near-wall formulation influences the accuracy of the wall shear stress, heat transfer and flow separations. Two fundamental methods, the wall function method and the low-Reynolds-number-modelling approach (low- $Re$ ), have been simultaneously enhanced to contribute to the improvement of turbulence models.

### 2.4.4.1 Standard wall functions

The wall function method uses empirical formulas to approximate flow conditions near the wall without resolving the boundary layer. It is an extension of the method in [84]. The basics of the standard wall functions are described with the aid of a cell-centred discretization in Figure 2.15. The conservation equations are computed by the integration over control volumes and the fluxes are integrated at the points  $\underline{ip}$ . The unknown fluxes at the wall are obtained by a logarithmic profile assumption implying that the first mesh point is in the logarithmic part of the boundary layer.

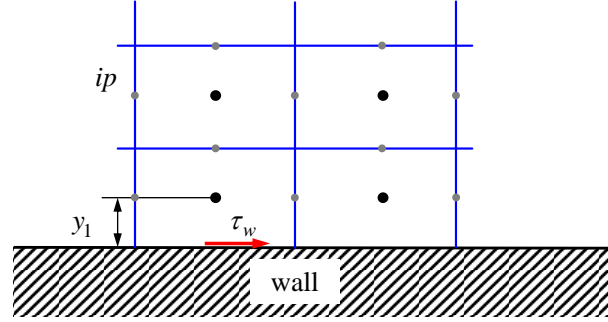


Figure 2.15: Near-wall grid.

The boundary conditions at the wall can be determined with the aid of the logarithmic law of the wall (2.46) and (2.47) with

$$u_\tau = \frac{U_1}{\frac{1}{\kappa} \ln(y^+) + B}, \quad \tau_w = \rho \cdot u_\tau^2 \quad \text{and} \quad y^+ = \frac{y_1 \cdot u_\tau}{\nu}. \quad (2.83)$$

The advantages of this approach are a relatively coarse mesh being allowed near to walls to model high gradient shear layers and the avoidance of having to account for viscous effects in the turbulence model. One major drawback is the sensitivity to the near-wall meshing and the dependence on the location of the first point nearest to the wall. The problem of inconsistencies of fine grids in this approach can be solved with the aid of the scalable wall function formulation of [85] presented in the following subsection.

#### 2.4.4.2 Scalable wall functions

The scalable wall functions avoid the restrictions on the near wall mesh of the standard wall function method. The definition of  $y^+$  is decoupled from the grid spacing for fine grids with a limiter between the logarithmic and the linear profile. Figure 2.16 illustrates this limiter. The relationship between  $u_\tau$  and  $U_1$  becomes linear if  $y^+ < Y_{lim}^+$ . The wall shear stress is modified to

$$u_\tau = \frac{U_1}{\frac{1}{\kappa} \ln(y^+) + B} \quad (2.84)$$

with the limiting expression

$$y^+ = \max(y^+, Y_{\text{lim}}^+) \text{ and } Y_{\text{lim}}^+ = 11.06. \quad (2.85)$$

The scalable wall function approach does not resolve the viscous sub-layer for arbitrarily fine grids because the wall is treated like the edge of the viscous sub-layer. Due to this fact, all grid points are outside the viscous sub-layer and all fine mesh inconsistencies are avoided. The scalable wall function approach is usually used for all turbulence models based on the  $\varepsilon$ -equation [86, 87].

### 2.4.4.3 Automatic wall treatment

The wall function methods presented above are based on problematic physical assumptions by neglecting the sub-layer in the mass and momentum balance. An alternative approach has been developed to eliminate these requirements by automatically switching from wall functions to a low- $Re$  formulation (automatic wall treatment). The low- $Re$  approach is a fine-grid analysis method extended by the viscosity-affected sub-layer near to the wall. It requires a very fine grid close to walls to resolve the details of the boundary layer profile using very small mesh length scales. Turbulence models such as the SST are based on the  $\omega$ -equation and suitable for this approach [85].

The value for  $\omega$  near the wall is blended between the logarithmic and the near wall formulation and allows a consistent mesh refinement from a coarse to a fine grid with mesh points in the viscous sub-layer. The flux for the  $k$  equation is assumed to be zero. The turbulent frequency in the first cell at the wall

$$\omega_1 = \sqrt{\omega_{\text{vis}}^2 + \omega_{\text{log}}^2} \quad (2.86)$$

is a blending equation between

$$\omega_{\text{vis}} = \frac{6\nu}{0.075 \cdot y^2} \text{ and } \omega_{\text{log}} = \frac{u_\tau}{0.3 \cdot \kappa \cdot y}. \quad (2.87)$$

A similar formulation is used for the velocity profile close to the wall

$$u_\tau = \sqrt[4]{\left(u_\tau^{\text{vis}}\right)^4 + \left(u_\tau^{\text{log}}\right)^4} \quad (2.88)$$

with

$$u_{\tau}^{vis} = \frac{U_1}{y^+} \text{ and } u_{\tau}^{log} = \frac{U_1}{\frac{1}{\kappa} \ln(y^+) + B}. \quad (2.89)$$

Physically, the first mesh point is always located at the wall. However, the first point is treated as being outside the viscous sub-layer in the wall function approach and virtually moved into the sub-layer for the low- $Re$  method. Figure 2.16 shows the transition of a low- $Re$  to a wall function mode [86].

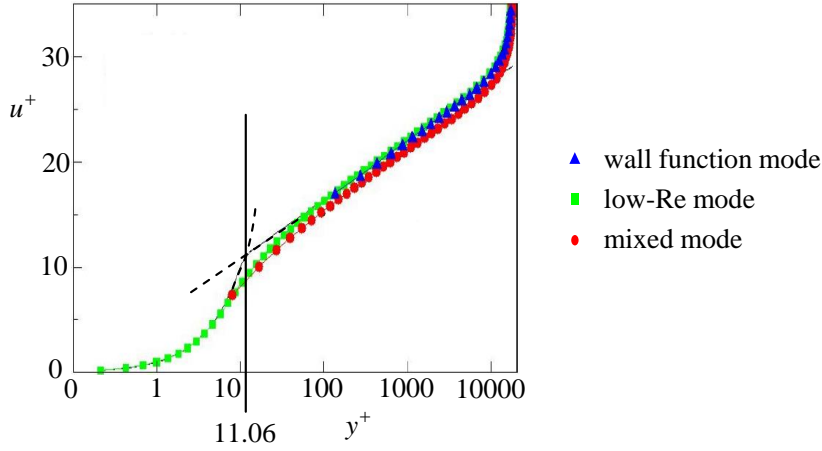


Figure 2.16: Velocity profile for the different near wall treatment methods [86].

#### 2.4.4.4 Heat flux computation

An algebraic formulation is used for the convective heat transfer computation to connect the heat flux and the temperature. The heat flux is expressed with the aid of the non-dimensional near wall velocity and temperature as

$$q_w = \frac{\rho c_p u^+ (T_w - T_f)}{T^+} \quad (2.90)$$

where  $T_w$  is the temperature at the wall,  $T_f$  the near-wall fluid temperature in the first cell adjacent to the wall,  $c_p$  the fluid heat capacity and  $q_w$  the heat flux at the wall. A fine grid with a  $y^+$  value around 1 is needed for highly accurate convective heat transfer predictions. Turbulent fluid flow and heat transfer computations without conjugate heat transfer requires the prescription of the wall heat flux or the wall temperature as a boundary condition. The non-dimensional temperature varies with the use of the turbulence model and hence the appropriate wall treatment approach.

The non-dimensional temperature profile for scalable wall functions is defined by the logarithmic law relation

$$T^+ = 0.1 \cdot \ln(y^+) + \beta \quad (2.91)$$

with

$$\beta_T = \left( 3.85 \cdot Pr^{1/3} - 1.3 \right) + 0.1 \cdot \ln(Pr). \quad (2.92)$$

The automatic wall treatment uses the thermal law of the wall function of [88] to model the thermal boundary layer. The temperature distribution is calculated with a blending between the viscous sub-layer and the logarithmic profile as

$$T^+ = Pr \cdot y^+ \cdot e^{-\Gamma} + \left[ 0.1 \cdot \ln(y^+) + \beta_T \right] \cdot e^{-1/\Gamma} \quad (2.93)$$

and

$$\Gamma = \frac{0.01 \left( Pr \cdot y^+ \right)^4}{1 + 5 \cdot Pr^3 \cdot y^+}. \quad (2.94)$$

The formulation and constants from the equations (2.90) - (2.94) are taken from [46] and used for heat transfer computations in ANSYS-CFX.

### 2.4.5 Modelling flows with moving reference frames

The prediction of the 3-dimensional viscous flow between and through rotating and stationary components is of considerable interest for many industrial problems. In the last decades, many CFD methods have been developed for the simultaneous analysis of the steady state or transient flow through the rotor and stator of turbo-machines. For example, a typical application is the flow computation of the interaction between the stator and rotor blades in turbines or compressors or the impeller and spiral casing of a hydraulic pump. The influence of the flow through the poles on the end winding bars and stator ducts is analyzed in this work. This technique is called multiple frames of reference (MFR) in the following.

The problem specification is in the majority of cases similar and will be described in the following for turbo-machinery, since the method was initially developed for such arrangements. The number of blades on the rotor (impeller) and stator (guide wheel) is usually not the same and therefore the angles of the corresponding sections

differ too. A section is the volume around one blade with the circumferential extension  $\gamma$  and periodic boundary conditions. A typical rotor-stator example is shown in Figure 2.17 with one blade for each stage. A stage is always one impeller and one guiding wheel. If a transient simulation with all blades is not mandatory it should be avoided to save computational time. Hence, a steady-state computation does not need all blades (sections) per stage and the computational effort decreases significantly.

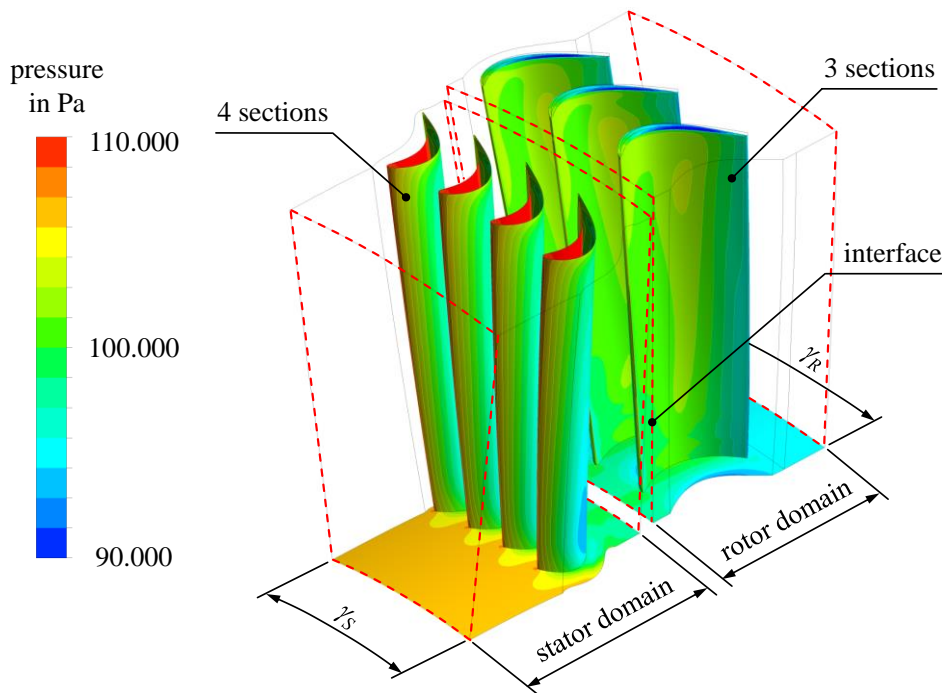


Figure 2.17: Rotor-stator example with MFR.

The main idea of most MFR codes is solving the Navier-Stokes equations in separate frames of reference for the rotor and the stator domain. The connection of the two domains with an appropriate interface strategy is the challenging task. Many variations for these frame change interfaces have been established for different CFD codes. A first example code solves an additional time and spatial averaged version of the RANS equations. The Navier-Stokes equations are appended by average sectional stress terms similar to the turbulent Reynolds stresses which carry the steady aspect of the interaction effects of the blade rows. This formulation characterizes the steady global aspect of the rotor-stator interaction without a mixing plane interface. Further details are presented in [89] and [90].

The second code applies a mixing plane between the rotating and stationary domains and is the most frequently implemented technique in commercial CFD programs. This is a simple approach where the flow variables are averaged tangentially by a mass or area weighting. The mixing plane is described in detail for the ANSYS CFX formulation in subsection 2.4.5.1 or in [46]. A comparison of the average section code and the mixing plane approach is shown for the performance prediction of a multistage compressor in [91].

### 2.4.5.1 Mixing plane

In the past, several researchers have developed methods to calculate the 3-dimensional flow through turbo-machines. The focus of these techniques has been especially on the circumferential averaging of flow parameters for periodic components like blade rows in turbines or compressors. The method in [92] is based on the first mathematical interpretations of this topic in [93] and [94]. The author has ignored the unsteady flow conditions between the rotor and stator and analyzed the flow for a rotor in a relative frame and for a stator in an absolute one. As a result, the 3-dimensional flow field is divided into two 2-dimensional planes to get a solution for the meridional and the radial section. One distribution of the flow parameters is given along streamlines in axial direction in the meridional plane. The revolution of the meridional streamlines around the machine axis forms the radial 2-dimensional planes. The concept of mixing planes used in most commercial codes was introduced in [95]. The authors investigated time marching methods and suggested the use of circumferentially averaged values on radial profiles on both sides of the connecting interface. The influence of the averaging and geometrical restrictions has been also discussed. In contrast to non-averaging simulations, a mixing plane should be independent of the relative position of the rotor and stator.

The mixing plane approach in ANSYS CFX is also called “multiple frames of reference - stage” method (MFR-ST). This method needs only one section per domain, i.e. one blade in turbo-machinery or one pole or one end winding bar in electrical machines. In every fluid domain, a steady-state problem is treated. The Navier-Stokes equations are solved in each fluid zone and the MFR-ST interface averages the fluxes in circumferential direction on bands on both the stator inlet and the rotor outlet boundary. This procedure is illustrated in Figure 2.18 and an example of averaging on bands for an interface between the generator components is shown in Figure 2.19. The MFR-ST can be used for large angle ratios between the two domains which highly reduces the number of elements. Other advantages are the

insensitivity to the relative position of the components and the fully implicit formulation. This approach also exhibits a considerable computational efficiency as it will be illustrated by the simulation times presented in subsection 3.5.4.

It should be noted that the MFR-ST interface is a steady-state solution and only an approximation to reality. The averaging on bands removes any unsteadiness that would arise due to circumferential variations in the section-to-section flow field like, for example, wakes, shock waves or separated flow. Local reverse flows as well as the mixing loss when the fluxes are entering the downstream machine component are also to be taken care of [46].

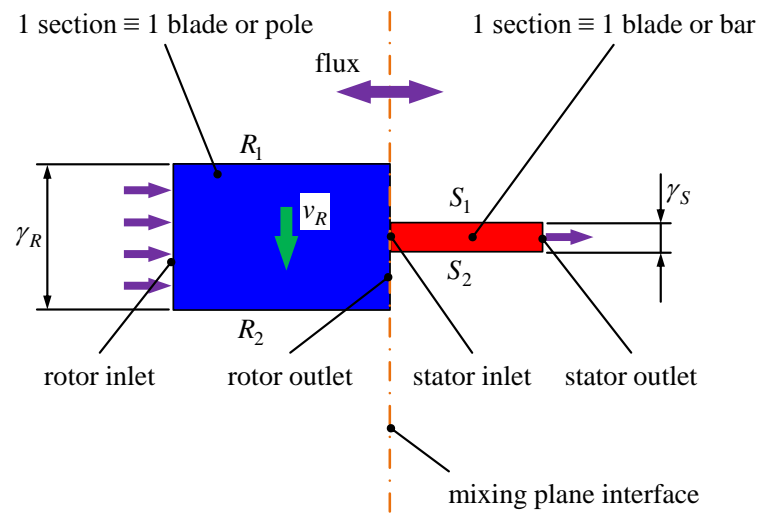


Figure 2.18: Mixing plane approach.  $R_1$ ,  $R_2$ ,  $S_1$ ,  $S_2$  are periodic boundaries and  $v_R$  is the circumferential velocity of the rotor.

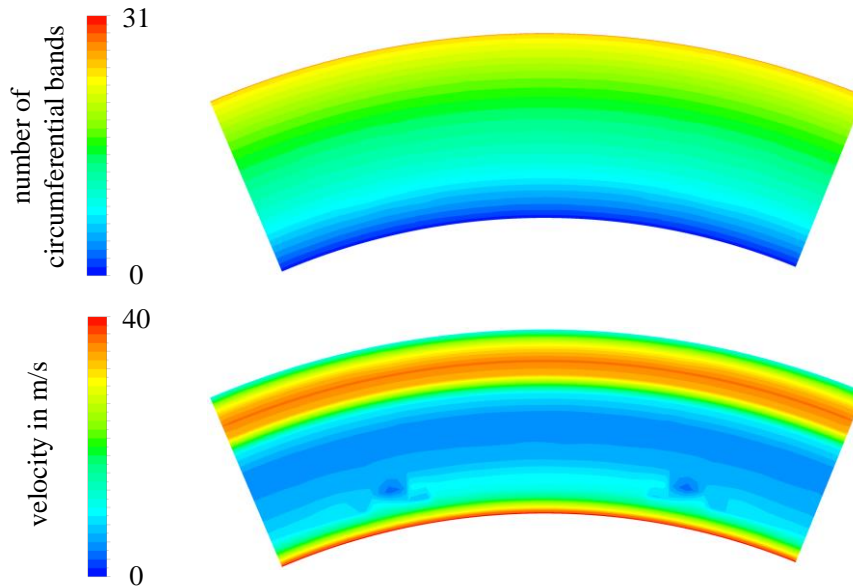


Figure 2.19: Mixing plane example with circumferential bands.

### 2.4.5.2 Frozen rotor

The second steady-state method is the “multiple frames of reference – frozen rotor” model (MFR-FR). This approach works with a frame change at the interface without averaging the fluxes. The individual domains can have different rotational or translational speed. The relative orientation of the moving and stationary components is fixed or “frozen”. It is important to model more than one section per component and the domain angles must be approximately equal. The conservation equations for the moving parts are solved in a moving reference system, the equations of the stationary parts in a static frame of reference. Subsequently, the frozen rotor interface compares and adjusts the results obtained. These relations are illustrated Figure 2.20. The frozen rotor model must be used for non-axisymmetric flow domains, such as impeller to volute or propeller to ship cases but it can also be used for axial compressors, turbines or electrical machines. The MFR-FR model has the advantage of being robust and well suited for high blade counts. The drawbacks of the approach include an inadequate prediction of local flow values and the sensitivity of the results to the chosen relative position of the rotor and the frozen stator for tightly coupled components [96].

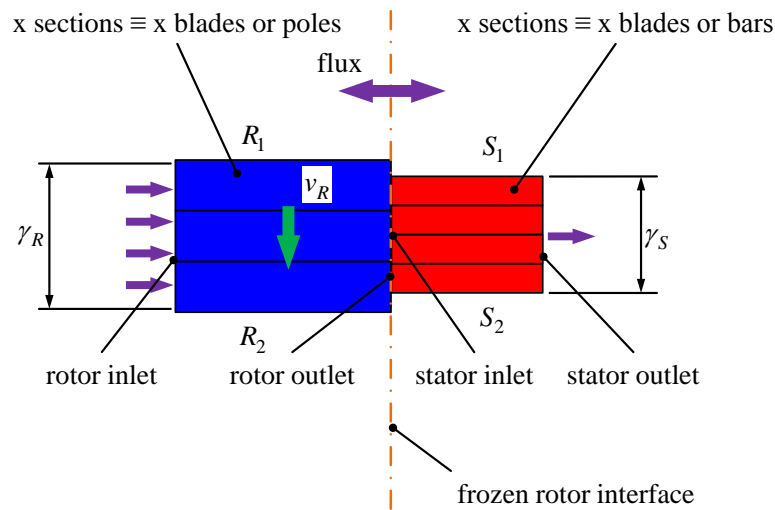


Figure 2.20: Frozen rotor approach.

The MFR-FR formulation of the interface depends on the velocity equations used. The interface treatment is only applied to the velocity and velocity gradients, because these vector quantities are converted when changing the reference frame. The scalar quantities (such as temperature, pressure, density, turbulent kinetic energy, ...) have no special treatment and they pass the interface locally without any change. Figure 2.21 shows the velocity distribution of the frozen rotor method for the same example as above. The velocity is not averaged on circumferential bands and vortices and local velocity differences can be taken into account.

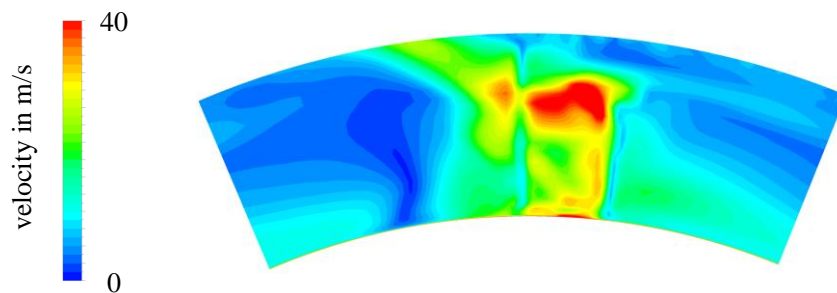


Figure 2.21: Frozen rotor example.

The flow in each rotating domain is solved using the rotating reference frame equations. There are two different formulations possible, the absolute and relative ones. The absolute equation is derived from the relative definition and uses the absolute velocity as the dependent variable. The relative velocity formulation is the

default solution method for a rotating domain. It is obtained by transforming the Navier-Stokes equations in a stationary frame into a rotating reference frame and using the relative velocity as the dependent variable. Such a system is illustrated in Figure 2.22.

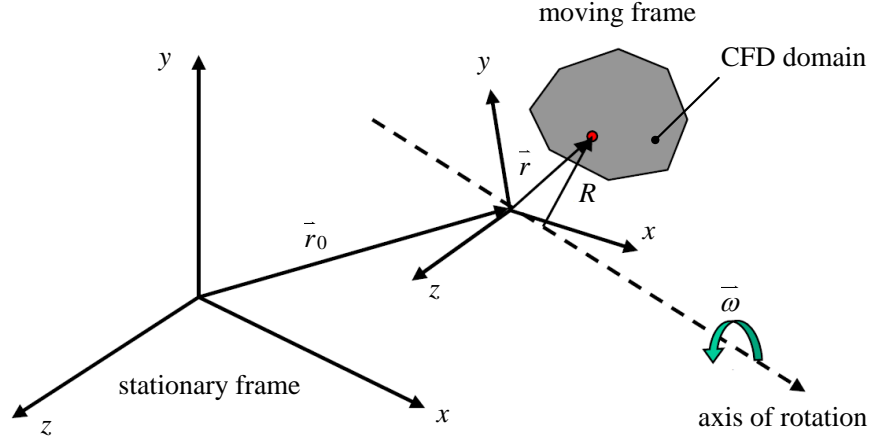


Figure 2.22: Stationary and moving reference frames.

The velocity viewed from the moving frame is the relative velocity  $\bar{v}_r$  which can be transformed with the absolute velocity  $\bar{v}$  (viewed from the stationary frame) and the velocity of the moving frame relative to the inertial reference frame  $\bar{u}_r$  as

$$\bar{v}_r = \bar{v} - \bar{u}_r \quad (2.95)$$

where

$$\bar{u}_r = \bar{v}_t + \bar{\omega} \times \bar{r} \quad (2.96)$$

with the translational frame velocity  $\bar{v}_t$  and the angular velocity  $\bar{\omega}$ . The governing equations in a rotating reference frame can be written in the relative velocity formulation for the continuity as

$$\frac{\partial u}{\partial t} + \nabla \cdot \rho \bar{v}_r = 0 \quad (2.97)$$

and the momentum as

$$\frac{\partial \bar{v}_r}{\partial t} + \nabla \cdot (\bar{v}_r \bar{v}_r) + \underbrace{2 \cdot \bar{\omega} \times \bar{v}_r}_1 + \underbrace{\bar{\omega} \times \bar{\omega} \times \bar{r}}_2 + \underbrace{\bar{\alpha} \times \bar{r}}_3 + \underbrace{\bar{a}}_4 = -\frac{\nabla p}{\rho} + \frac{\nabla \tau}{\rho} + \bar{f}^B \quad (2.98)$$

where

$$\bar{\alpha} = \frac{\partial \bar{\omega}}{\partial t} \quad \text{and} \quad \bar{a} = \frac{\partial \bar{v}_t}{\partial t}. \quad (2.99)$$

The momentum equation (2.98) has four additional acceleration terms. The first one is the Coriolis acceleration 1 and the second term is the centripetal acceleration 2. The two other terms 3, 4 are due to the unsteady change of the rotational speed and linear velocity and vanish for constant translational or rotational speeds. If the zone is stationary ( $\omega = 0$ ), the equations are reduced to the normal stationary forms. At the MFR-FR interfaces between two zones, a local reference frame transformation is performed to enable flow variables in one domain to be used to calculate fluxes at the boundary of the adjacent domain [96].

## 3 Numerical models

### 3.1 Investigated ventilation schemes

Large hydro generators are usually cooled by air. The ventilation through the machine is realized by radial or axial fans mounted on the shaft or by an external ventilation system. Furthermore, the various parts of the generator can be cooled in series or parallel by a fan. As an example for the cooling of a hydro generator, a cut through the radial fan machine of Figure 2.2 is shown in Figure 3.1. Air enters the machine with a swirl from the fan at the inlet (a). The major part of the air (green path) flows directly into the pole region (b), whereas a minor one (blue path) streams through the end winding bars (c), makes a loop and passes the bars a second time to merge with the main air flow in the pole region. From there, the air flows to the air gap, enters the stator ventilation ducts (d) and exits the machine at the outlet (e) to an external heat exchanger.

The right quantity of air and its circulation through the machine depend on the design of the appropriate ventilation scheme consisting of three important components: the fan, the air guiding plates of the inlet frame and additional openings also called bypass openings.

A radial or axial fan is usually designed to maximize efficiency and power. The theory and fundamentals of the kinematics and construction of fans are described in detail in [97] and [98]. In [8], the specialties of fans in electrical machines and their technical realization are presented. The machine frame is designed to guide the air to hot components once it has left the fan.

In the present work, a parametric study has been carried out by varying the arrangement of the guiding to investigate their influence on the machine cooling, especially the temperature of the end winding bars. Bypass openings in the inlet frame are used to increase the suction effect in the inlet region. As a result, the velocity through the bars and the heat transfer coefficient increases and the temperature decreases at the end winding walls. Table 3.1 and Figure 3.2 illustrate these adaptations for different ventilation schemes. 15 different ventilation schemes have been investigated in the course of the parametric study.

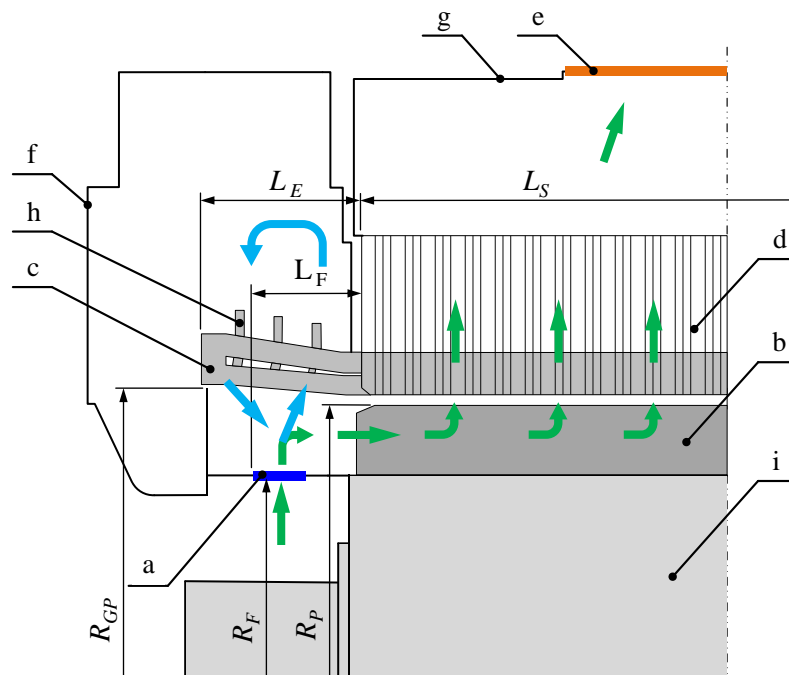


Figure 3.1: Layout of a large hydro generator with a radial fan and the main components for a CFD computation: a) boundary inlet, b) salient pole, c) end winding bars, d) stator ducts, e) boundary outlet, f) frame inlet, g) frame outlet, h) support rings, i) shaft.

$L_E$  ... length end winding bars,  $L_S$  ... length stator,  $L_F$  ... length fan position,  $R_F$  ... radius fan,  $R_P$  ... radius pole shoe,  $R_{GP}$  ... radius guiding plate.

Table 3.1 shows the geometrical details of the different ventilation schemes. Additionally, the main dimensions of the generator are shown as well. The geometry and the dimensions of the end winding bars are similar for all 15 schemes. This simplification has been adopted to limit the number of variations for the parametric study. A further scaling of the bar dimensions would have increased the extent of the parametric study many times over.

The investigated machine has 8 poles. The first three types are forced ventilated by an external cooling system with the third one having an additional serial cooling of the pole region. The schemes 4 and 5 have an axial fan located on the inner pole diameter. The remaining 10 schemes are equipped with a radial fan at different positions as well as various arrangements of the guiding plates or bypass openings mentioned above. The end winding, rotor and stator core geometry are the same in all cases. The fan geometry has not been modelled and, hence, an assumed outlet velocity of the fan has been used as an inlet boundary condition (see subsection 3.4.2).

Ventilation scheme	Fan type	Externally ventilated	Shaft mounted	Position fan	Bypass opening	End winding shield
1	radial	x	-	-	-	-
2	axial	x	-	-	-	-
3	radial	x	-	-	-	x
4	axial	-	x	-	-	-
5	axial	-	x	-	x	-
6	radial	-	x	CU	-	-
7	radial	-	x	LU	-	-
8	radial	-	x	RU	-	-
9	radial	-	x	CD	-	-
10	radial	-	x	LD	-	-
11	radial	-	x	CU	-	-
12	radial	-	x	LU	-	-
13	radial	-	x	CU	x	-
14	radial	-	x	CU	x	-
15	radial	-	x	LU	x	-

CU ... center up, LU ... left up, RU ... right up, CD ... center down, LD ... left down

Table 3.1: List of investigated ventilation schemes and dimensions.

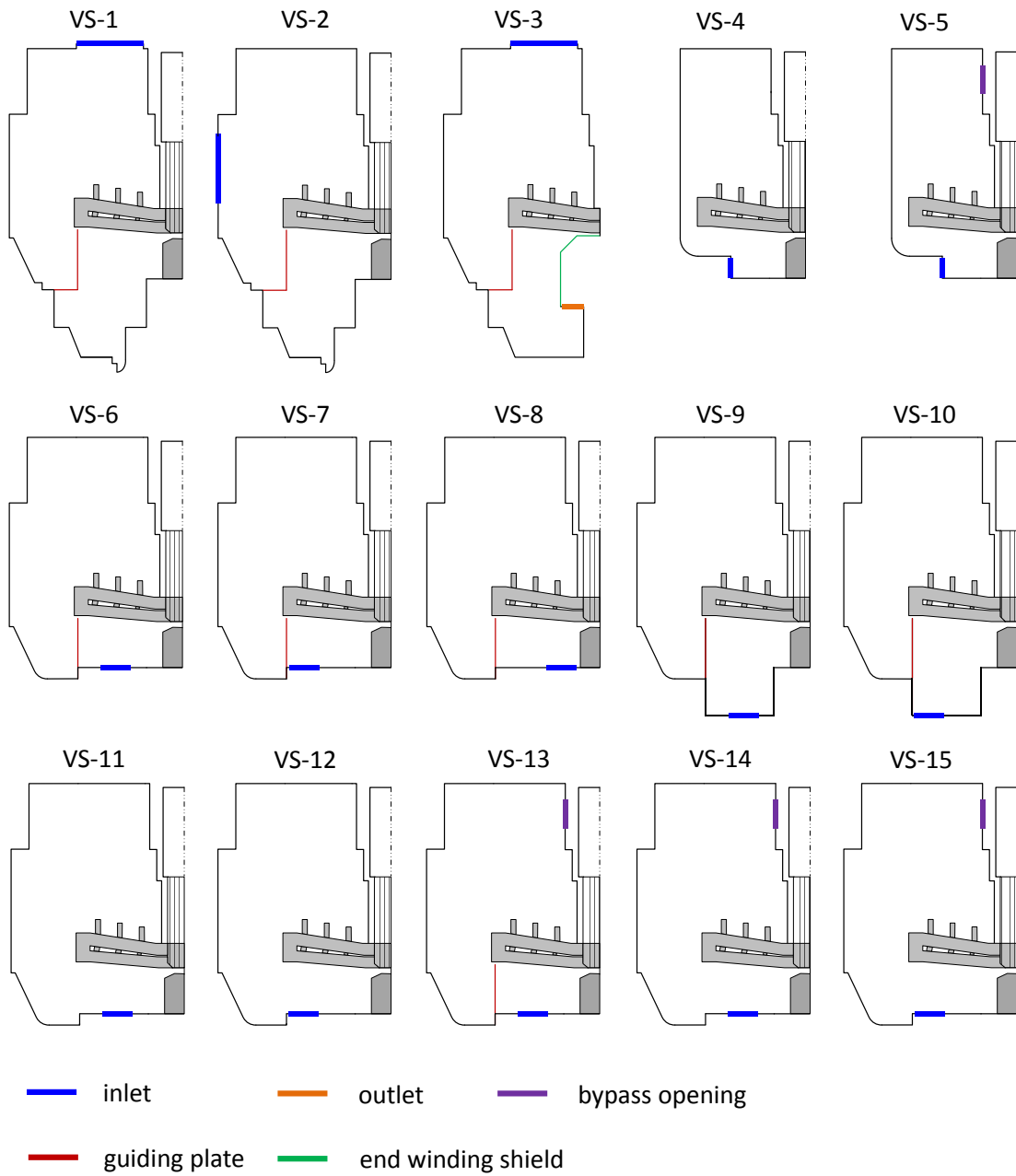


Figure 3.2: Inlet geometry and fan position of the different investigated ventilation schemes.

## 3.2 Pole sector model

The pole sector model is the state-of-the-art CFD simulation model for electrical machines. A PSM of a radial fan cooled machine is shown Figure 3.3. All components (domains) have been reduced to the angle of one pole. Consequently, the following PSM has a circumferential angle of  $45^\circ$ . The most important domains for a fluid flow computation are the inlet, the end winding top and bottom bar, the poles, the stator ducts and the outlet. Less important parts for a fluid dynamics simulation like frontal connections have been neglected.

Due to the large frame size of hydro generators it makes sense to use all simplifications mentioned in subsection 1.2. An assumed symmetry condition in axial direction (j) halves the mesh. Periodic boundaries (k, red dashed line) close the domains in circumferential direction and the interface method multiple frames of reference - frozen rotor (see section 2.4.5.2) connects the individual domains. Moreover, the geometry of the fan has not been modelled either.

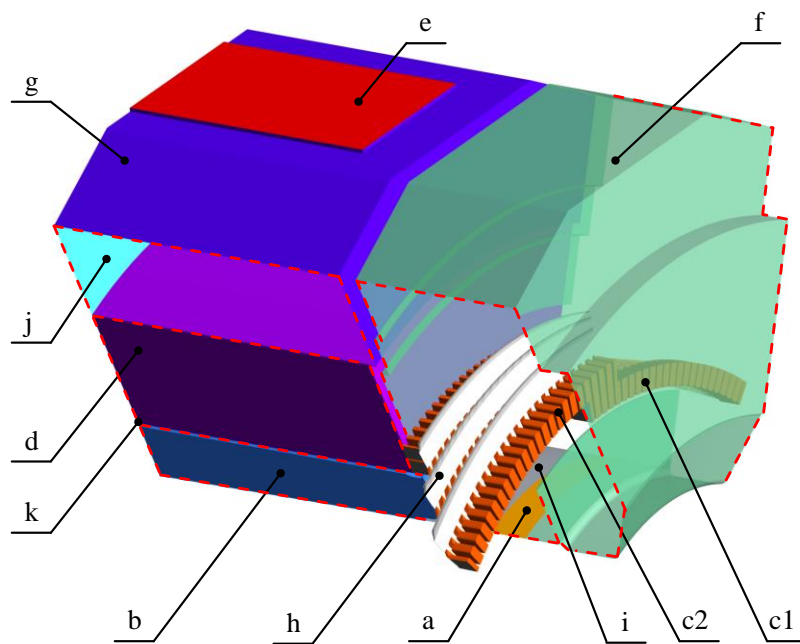


Figure 3.3: Pole sector model of a large hydro generator with a radial fan and the main components for a CFD computation: a) boundary inlet, b) salient pole, c1) top bars, c2) bottom bars, d) stator ducts, e) boundary outlet, f) frame inlet, g) frame outlet, h) support rings, i) shaft, j) symmetry plane, k) periodic boundaries.

The mesh of the model is rather coarse but the number of elements can still reach about 30 to 50 million. Therefore, the ribs on the surface of the poles have been neglected to simplify the model (see Figure 3.4). This is permissible since the heat flow at the pole surfaces does not substantially influence the heat transfer at the end windings which is in the focus of this work. For the same reason, all solid walls have been assumed to be smooth without a roughness.

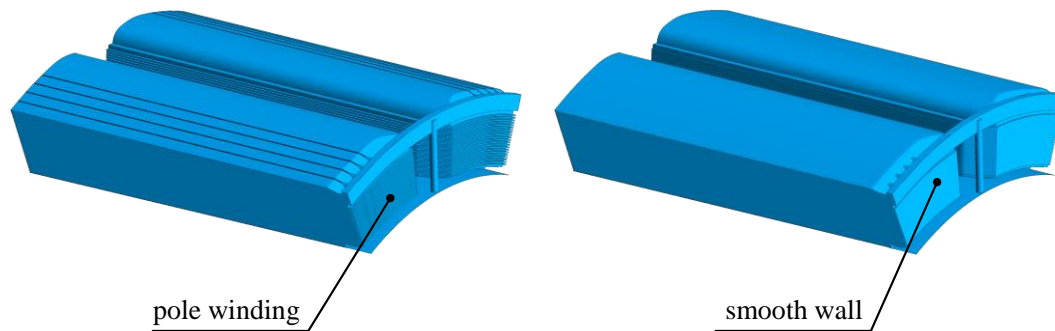


Figure 3.4: Simplification of pole geometry.

The most important components for this thesis are the end winding bars. Figure 3.5 presents a detailed view of the real and modelled bars. The support rings (r1 - r3) and the space brackets (sb1, sb2) provide a mechanical support of the end windings but they have not been considered for the heat transfer calculations, i.e. they have been assumed to represent adiabatic walls. Figure 3.5 also shows the classification of the bars into 6 zones whereby the lower case letters identify the bar walls. The first 2 zones are between the stator and support ring 1 (t1, b1), the next zones between support rings 1 and 3 (t2, b2) and the last 2 zones extend from ring 3 to the end of the bars (t3, b3). The notations W1-W3 and U1-U3 identify control surfaces between two bars at the inlet and outlet of the end winding region (see Figure 3.5c, purple lines). This classification will be made use of in sections 3.5.2 and 3.5.3 to define local HTC. Furthermore, Figure 3.5b shows the area between two bars. The flow can stream straight through the zones t1, b1 and t3, b3 but the top and bottom bars cross in the zones t2, b2. Due to this, the flow will be decelerated and deflected in this area.

The accuracy and reliability of the PSM have been verified with measurements and lumped parameter networks in several publications [18-20, 22-26]. However, the computational effort is too large for a comprehensive parametric study with several hundred boundary conditions and ventilation schemes. Due to this fact, a PSM can lead to unacceptably high computation times. Hence, a reduced model has been

developed to simplify the PSM and speed up the simulation. The PSM is only used as a reference computation model for the SSM described in the next subsection.

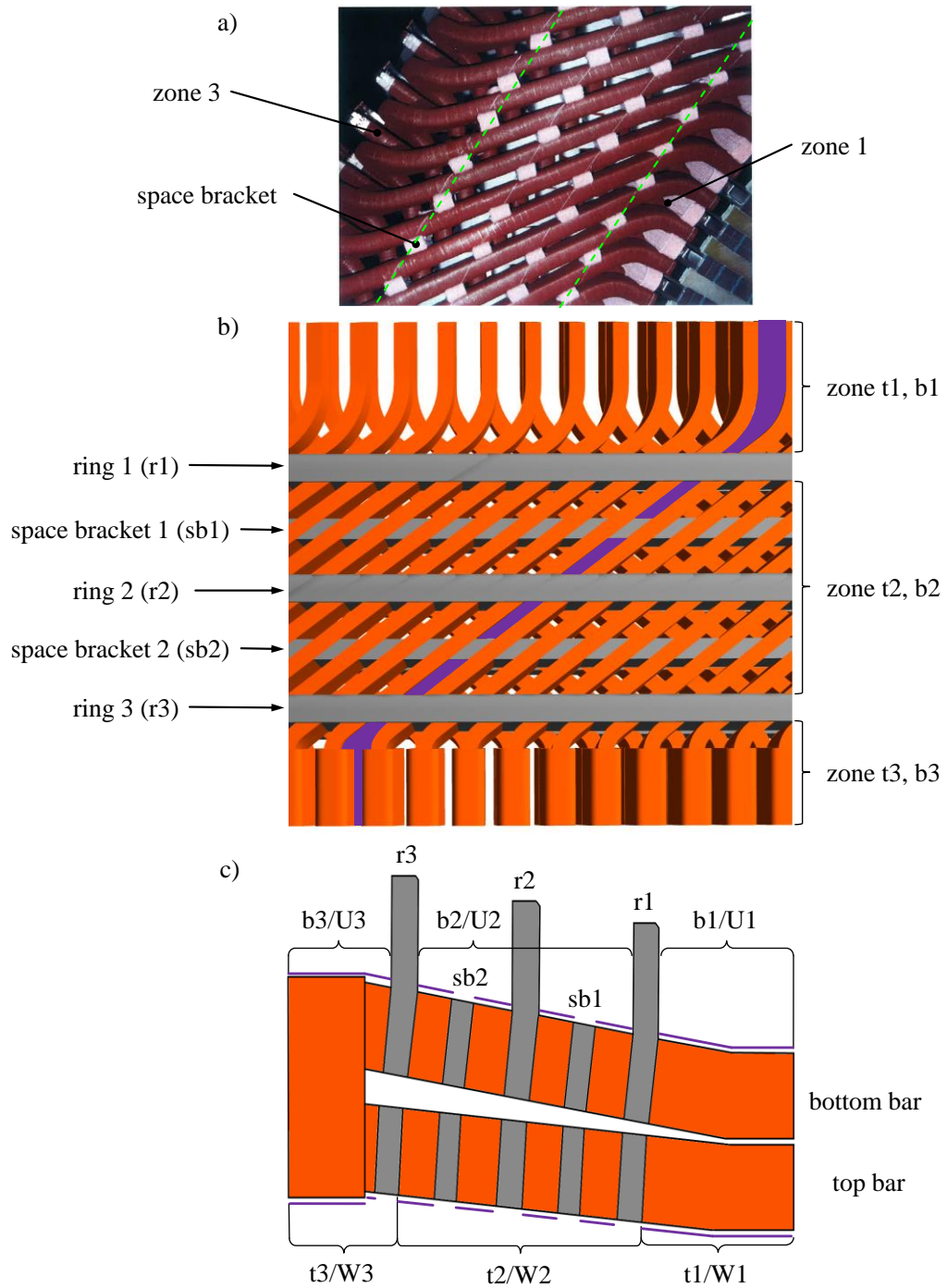


Figure 3.5: End winding geometry with classification: a) real arrangement, b) top view, c) side view.

### 3.3 Slot sector model

This reduced model is a further simplification of the pole sector model. Acceptable computation times can be achieved by reducing every component to its minimal periodic circumferential angle, i.e. the domains top bar, bottom bar, stator ducts and outlet area are reduced to the angle of one slot. The domains inlet and rotor have still a circumferential range of one pole. Periodic interfaces are used in circumferential direction and the method of multiple frames of reference – mixing plane (see section 2.4.5.1) is applied between the domains. This reduced model is illustrated in Figure 3.6.

A similar concept of reducing circumferential components of rotating machines has so far been published for the simulation of hydraulic fluid machines and thermal turbo machines [99-101]. These machines can be taken into account with the whole runner and all guide vanes or the simulation model is reduced to one section (blade) per component to save elements and calculation time. A further advantage is represented by the circumferentially averaged results which are often more important to know than the local maxima of pressure, velocity, turbulence or temperature.

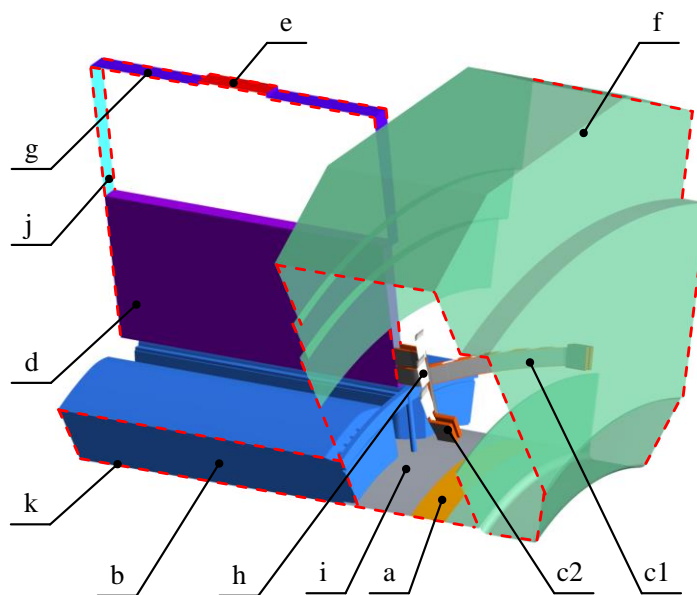


Figure 3.6: Slot sector model of a large hydro generator with a radial fan and the main components for a CFD computation: a) boundary inlet, b) salient pole, c1) top bar, c2) bottom bar, d) stator ducts, e) boundary outlet, f) frame inlet, g) frame outlet, h) support rings, i) shaft, j) symmetry plane, k) periodic boundaries.

## 3.4 Simulation set-up

### 3.4.1 Mesh generation

ANSYS ICEM CFD [102] has been used for the mesh generation. The advantage of this code is the easy way of meshing large and complex volumes with hexahedral elements which have been used for all grids.

The mesh density in near wall regions and especially the height of the first element at the wall is an important issue for the accurate prediction of the heat transfer coefficient. Furthermore, the appropriate near-wall formulation depends on the height of the first cell at the wall and influences the computation of the wall shear stress, the convective heat transfer and the flow separations. Relevant considerations of the mesh generation will be described for the example in Figure 3.7 showing a cross-section of the mesh through the end winding and inlet region. The locations of the mixing plane interfaces are also indicated in this figure. The numerical simulations have been carried out with a relatively fine mesh near the end winding bars and a coarse mesh for all other domains. The height of the first element at the wall as well as the number of elements at an edge have been appropriately defined and the growth from the wall is characterized by a Poisson distribution [102].

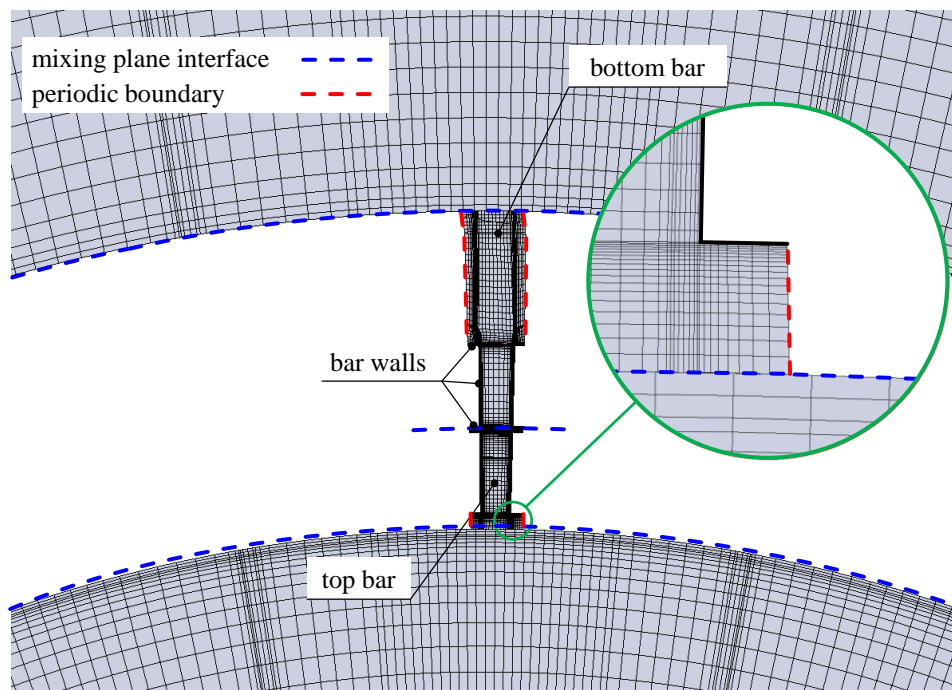


Figure 3.7: Mesh of the end winding and inlet domain with interfaces.

As mentioned in section 2.4.4, the non-dimensional distance from the wall is a crucial parameter for the near wall treatment. The authors in [86] have recommended that  $y^+$  should be around 1 for accurate heat transfer predictions. However, it is not possible to maintain a constant  $y^+$  of 1 along the bars because the velocity and hence the wall shear stress in the first element at the wall influence this parameter considerably. Figure 3.8 illustrates the relation between the wall shear stress, the velocity and the non-dimensional distance from the wall. A very small  $y^+$  results at zones with a low velocity or wall shear stress (t2, b2) and a higher  $y^+$  at the walls in the zones t1 and b1 where the velocity is much higher due to the rotating poles. Nevertheless, the average  $y^+$  along the bars is about 7 for this example which is sufficient. This will be shown in subsection 3.5.1 by presenting various grids for a mesh sensitivity study conducted to find the appropriate mesh size at the end winding region for the parametric study.

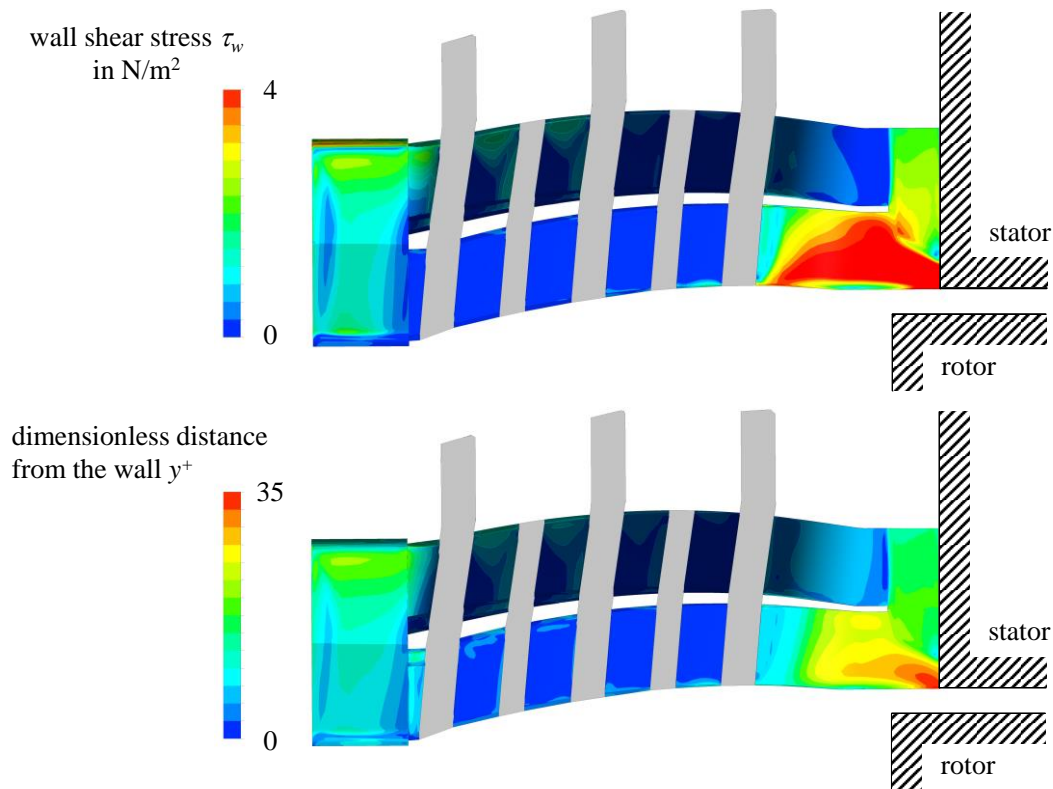


Figure 3.8: Relation between wall shear stress and non-dimensional distance from the wall.

The mesh of the domain inlet is coarse with  $y^+$  values of up to 200 (see Figure 3.7). A very coarse mesh is also used for the remaining parts, i.e. the poles, stator

ducts and outlet area. However, the surfaces of these domains are not investigated with respect to heat transfer predictions and the non-dimensional distance from the wall can therefore be rather high.

### 3.4.2 Boundary conditions and loss sources

The boundary conditions for the inlet and outlet have been estimated from measurements and the heat losses from electromagnetic loss computations. The solid domains have not been considered for the CFD simulations; their various surfaces have been set to different constant wall temperatures. Adiabatic walls are assumed at the space brackets and support rings. The poles and fans rotate with 500 – 1000 rpm. The inlet boundary conditions for the external ventilation schemes are a volume flow rate of 2.5 – 3.375 m<sup>3</sup>/s per pole section and a constant air temperature.

An additional input has been used for fan mounted schemes to ensure enforcing the appropriate angular momentum to enter the system: the absolute velocity at the fan outlet  $c_{F2}$  is specified. Depending on the fan type, axial or radial, this absolute velocity has been chosen between 20 and 100 m/s. The velocities at the outlet of a fan (= inlet generator) are defined by the velocity triangles of the blades as shown in Figure 3.9 [97].

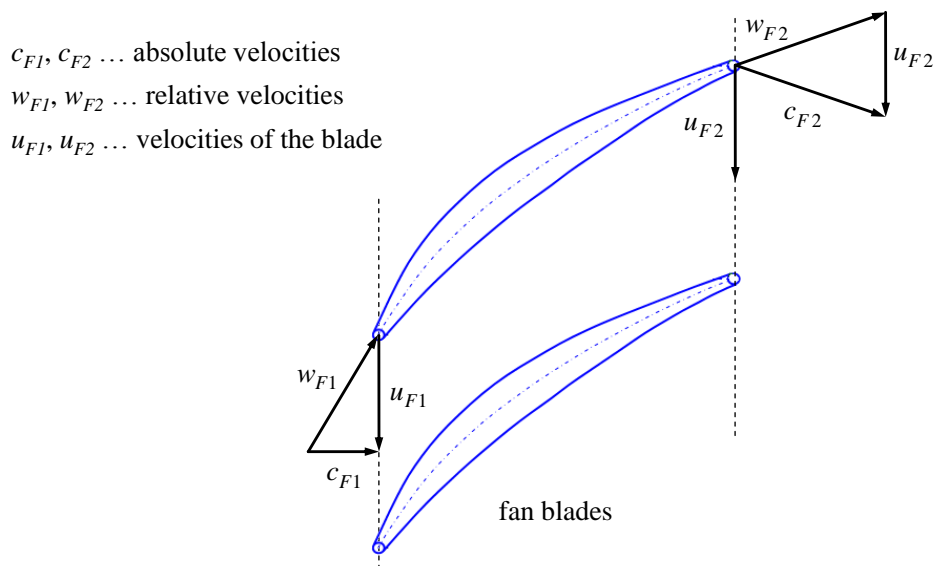


Figure 3.9: Velocity triangle.

The ambient pressure of 1 bar has been applied at the main outlet and a volume flow rate at the bypass outlet. The rotational speed, the volume flow rate and the

absolute fan velocity have been varied in the parametric study in chapter 4 to compute a range of different operational cases for each ventilation scheme.

### 3.4.3 Fluid properties

The cooling medium used in the hydro generator is air assumed to be an ideal gas for the numerical simulations. The fluid properties of air depend on the temperature (see Table A.1 in Appendix A) but the standard material properties in ANSYS-CFX for an ideal gas are temperature independent, i.e. the thermal conductivity  $\lambda$ , the specific heat capacity  $c_p$  and the dynamic viscosity  $\mu$  are constant. Hence, the fluid properties have been adjusted since such simplifications may lead to inaccurate results. The temperature dependence of the fluid properties is approximated by means of the Sutherland model [103]. This model is obtained from the kinetic gas theory with an idealized characterization of the intermolecular interactions. The dynamic viscosity varies with temperature only as

$$\mu = \mu_0 \cdot \frac{T_R + S_\mu}{T + S_\mu} \cdot \left( \frac{T}{T_R} \right)^{n_\mu} \quad (3.1)$$

where  $\mu_0$  is the reference molecular viscosity,  $S_\mu$  is the Sutherland constant which is a characteristic of the gas and  $n_\mu$  is the temperature exponent. The reference temperature  $T_R$  is 325 K. A similar formula is used for the thermal conductivity in the form

$$\lambda = \lambda_0 \cdot \frac{T_R + S_\lambda}{T + S_\lambda} \cdot \left( \frac{T}{T_R} \right)^{n_\lambda} \quad (3.2)$$

where  $\lambda_0$  is the reference molecular conductivity,  $S_\lambda$  is the Sutherland constant for the thermal conductivity and  $n_\lambda$  is the temperature exponent. The numerical values of these constants are

$$\begin{aligned} S_\mu &= 77.8 \text{ K}, & S_\lambda &= 60.7 \text{ K}, \\ \mu_0 &= 1.97 \cdot 10^{-5} \text{ Pa s}, & \lambda_0 &= 2.74 \cdot 10^{-2} \text{ W / m K}, \\ n_\mu &= 1.574, & n_\lambda &= 1.676. \end{aligned}$$

The reference values  $\mu_0$  and  $\lambda_0$  have been chosen for the temperature of 313K from the measured thermodynamic properties of dry air shown in Table A.1 and gathered from [5]. The temperature dependence of the specific heat capacity is defined by the

thermodynamic data used in the NASA chemical equilibrium code [104]. In this case the zero pressure polynomial approximates the specific heat capacity at a constant pressure as

$$c_p = R_s \cdot \left[ a_1 + a_2 \cdot T + a_3 \cdot T^2 + a_4 \cdot T^3 + a_5 \cdot T^4 \right] \quad (3.3)$$

where the gas constant  $R_s$  is 287.058 J/ kgK and the coefficients are

$$\begin{aligned} a_1 &= 3.574, & a_2 &= -4.2691 \cdot 10^{-4} \text{ K}^{-1}, \\ a_3 &= -4.1854 \cdot 10^{-8} \text{ K}^{-2}, & a_4 &= 3.0986 \cdot 10^{-9} \text{ K}^{-3}, \\ a_5 &= -2.3848 \cdot 10^{-12} \text{ K}^{-4}. \end{aligned}$$

The unknown coefficients  $a_1$  to  $a_5$  have been found by fitting them to values of the material properties in Table A.1. These values are valid in a temperature range from 273 K to 673 K.

## 3.5 Validation of the reduced model

The reduced model has been investigated and optimized for accurately simulating the convective wall heat transfer coefficient at the end winding bars of large hydro generators. To this end, different SSMs have been developed and compared to a reference PSM. Similarly to a CFD study of a 15 stage axial compressor in [99], the results are analyzed regarding mesh size, turbulence models, rotor-stator interface models and fluid properties. Particular details of the validation have been presented at several conferences or have been published in scientific journals [105-107].

### 3.5.1 Mesh sensitivity study

As mentioned in subsection 3.4.1, the mesh density study aims at establishing the necessary mesh size near the end winding walls and the relation between the HTC and  $y^+$ . An appropriately fine mesh size near to walls and, consequently, a small enough  $y^+$  value are the most important aspects to calculate an accurate HTC. Furthermore, the influence of the turbulence model with its suitable wall treatment method cannot be neglected.

8 meshes for the end winding bars are described in Table 3.2 and Figure 3.10 illustrates four grids at the topside of two bars.  $n$  indicates the number of elements between two bars in circumferential direction and  $\Delta y$  the height of the first element at the walls. The rest of the volume is automatically meshed with a defined ratio of

growth and a Poisson distribution in the direction normal to the wall [102]. Attention has also been paid to generating a homogeneous mesh along the whole bar in axial direction. Table 3.2 illustrates vividly the fast increase in the number of elements for a very fine mesh with an averaged  $y^+$  of about 1. Hence, it is hardly possible to carry out a parametric study with around 20 times more elements that would result for a PSM.

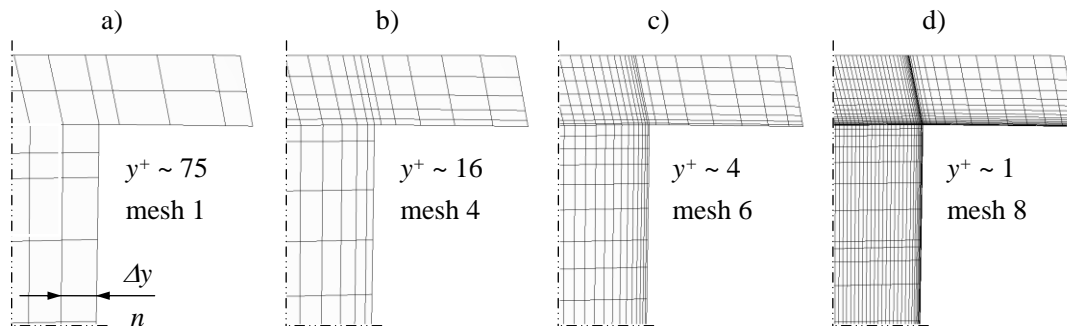


Figure 3.10: Grids for mesh density study.

Mesh	$\Delta y$ in mm	Average $y^+$ at bars	Number of elements
1	5,00	75	45000
2	3,00	46	65000
3	2,00	32	81000
4	1,00	16	146000
5	0,50	8	318000
6	0,25	4	693000
7	0,12	2	989000
8	0,05	1	1682000

Table 3.2: Different mesh size at end winding domains.

The heat transfer is quantitatively described by the Nusselt number  $Nu$  and the results are normalized to the maximum  $Nu$  value to facilitate a general comparison.

Figure 3.11 shows the results of the mesh sensitivity study for the external ventilation scheme VS-1. The simulations have been carried out both with the SST and  $k-\varepsilon$  turbulence models described in Appendix D, to establish the appropriate turbulence model for the parametric study and heat transfer predictions.  $Nu$  increases

with a decreasing  $y^+$  and reaches its maximum at about  $y^+ = 8$  in Figure 3.11a. At lower  $y^+$  values, it just fluctuates around the maximum value. The non-dimensional distance from the wall is very sensitive to the variation of the near wall velocity  $u_\tau$  which especially depends on the volume flow rate and the rotational speed. The results of the  $k-\varepsilon$  turbulence model in Figure 3.11b do not settle down at a specific  $y^+$  and  $Nu$  is increasing nearly linearly in all zones. As a result, all following simulations have been carried out with the SST turbulence model because the  $k-\varepsilon$  model does not prove to be suitable for near wall flow computations [83]. This part of the parametric study has also been presented in [105].

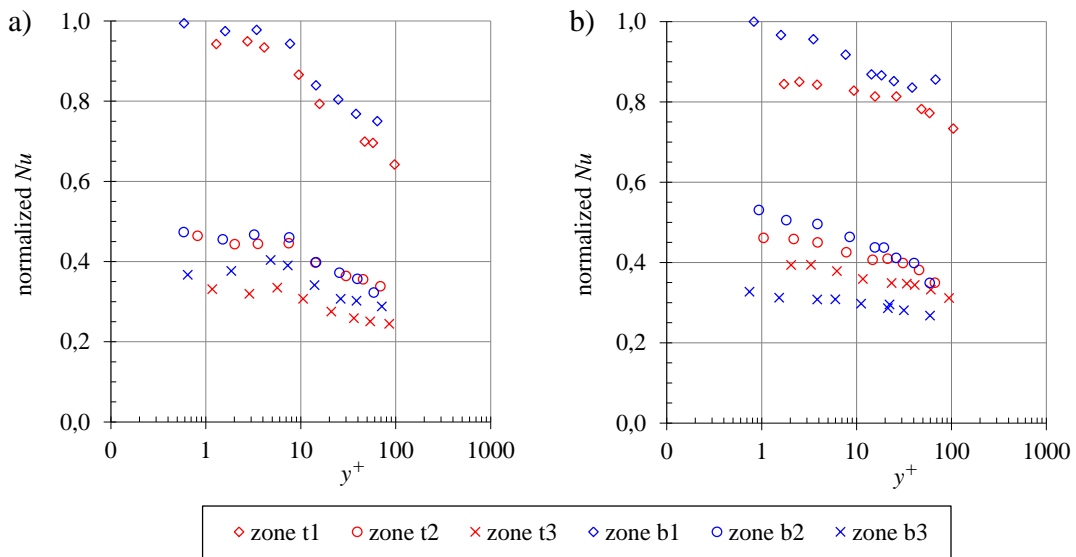


Figure 3.11: Mesh sensitivity study of VS-1 with different turbulence models: a) SST, b)  $k-\varepsilon$ .

The radial fan scheme VS-6 with the end winding grids 3 – 8 of Table 3.2 has been used as a second test case. The Nusselt numbers in Figure 3.12 also reach the maximum at a  $y^+$  value of about 8 and this fact confirms the above decisions. However, the near wall velocity  $u_\tau$  is additionally influenced by the swirl of the fan which has a great impact on the flow through the various zones and causes backflows, flow separations and velocity changes between the bars. These effects reduce the accuracy of the heat transfer computations especially in the zones t2 and b2. A preliminary version of this second part of the mesh sensitivity study has been published in [106] for the grids 5 and 8.

An average  $y^+$  value of about 8 results in sufficient accuracy for heat transfer predictions at the end winding bars, although  $y^+$  is in the range of 0.1 to 30 along the

bars because the velocity is not constant (see Figure 3.8). Moreover, very fine meshes with an averaged  $y^+ \approx 1$  can lead to convergence problems when using mixing plane interfaces in combination with a too fine mesh in regions with high velocity gradients (e.g. zone t1). Especially shaft mounted ventilation schemes with a high fan momentum have these problems at the connection between the inlet, end winding and rotor domains. This occurs particularly during the first hundred iterations and can be prevented by reducing the time step. The authors of [24] have also identified this numerical instability.

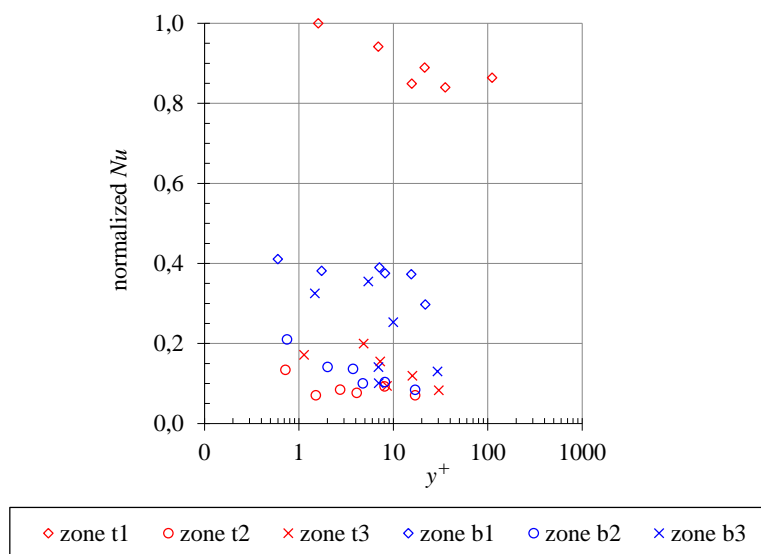


Figure 3.12: Mesh sensitivity study of VS-6 with the SST turbulence models.

### 3.5.2 Comparison to the steady state results

A further optimization of the SSM has been carried out by comparing different simulation settings of the SSM to two reference PSMs. These computations have been done for VS-1. The mesh of PSM 1 is coarse with about 30 million elements. PSM 2 is similar to PSM 1 except for the very fine mesh near the end winding walls ( $y^+ \approx 1$ ). In order to counteract the increase in the number of elements, the stator ducts and the outlet of PSM 2 have been reduced to one slot sector. The mesh sizes of the rotor and inlet domains are also much smaller for PSM 2. An MFR-MP interface connects the outlet with the ducts and the ducts with the rotor. The flow at the inlet region is not significantly affected by the simplifications between the rotor and stator ducts.

Furthermore, four different SSMs have been generated with the numerical setting varied. Details of the models are indicated in Table 3.3. The values of  $y^+$  represent an average quantity over the whole surface of the bars. The inlet, rotor, stator ducts and outlet domains of the model have been meshed relatively coarse in SSM 1, 3 and 4. Only SSM 2 has a finer mesh for these domains. A temperature dependent ideal gas model has been assumed in SSM 4. The following graphs in this section show the area averaged values of  $Nu$  at the bar walls and the area averaged values of  $Re$  in the appropriate surfaces between two bars. The Nusselt and Reynolds numbers have been normalized to the maxima of PSM 1 to compare the various SSMs to the reference PSMs.

	PSM 1	PSM 2	SSM 1	SSM 2	SSM 3	SSM 4
Frame change model	MFR-FR	MFR-FR	MFR-ST	MFR-ST	MFR-ST	MFR-ST
Mesh end winding	coarse	fine	coarse	coarse	fine	fine
Mesh global	medium	coarse	coarse	medium	coarse	coarse
Average $y^+$ at bars	30	1	30	30	1	1
Number of elements						
End winding	5.2 mio	31.2 mio	0.25 mio	0.25 mio	1.5 mio	1.5 mio
Other parts	23.7 mio	1.7 mio	1.6 mio	7.0 mio	1.6 mio	1.6 mio
Total	28.9 mio	32.9 mio	1.9 mio	7.2 mio	3.1 mio	3.1 mio
Fluid properties	TI	TI	TI	TI	TI	TD

TI ... temperature independent    TD ... temperature dependent

Table 3.3: Numerical setting of different steady-state models.

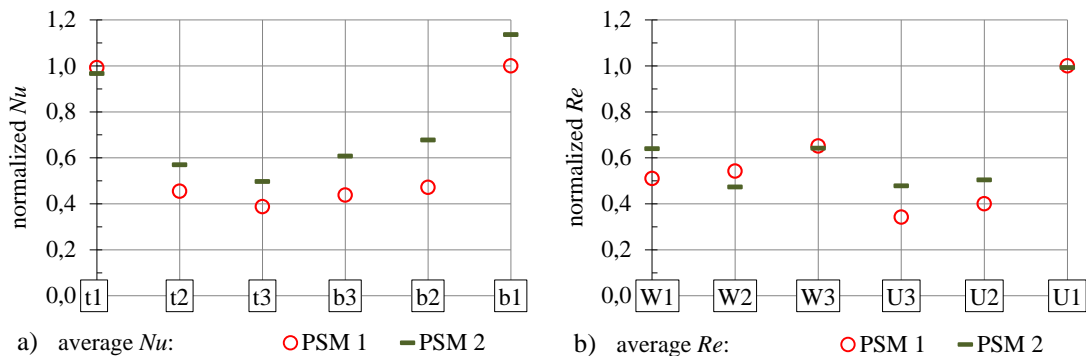


Figure 3.13: Comparison of PSM 1 and PSM 2: a)  $Nu$  distribution, b)  $Re$  distribution

The comparisons for the two PSMs are shown in Figure 3.13. The difference between the Reynolds numbers in Figure 3.13b is low and this indicates that the simplifications for PSM 2 do not much influence the flow and heat transfer in the bar region. The values of the Nusselt numbers in Figure 3.13a are higher for PSM 2 because the non-dimensional distance at the bar walls is very small for this model.

Figure 3.14 presents the distributions of the turbulent kinetic energy in front of the rotor (interface 2) and under the end winding bars (interface 1). The MFR-FR interface computes areas with high energy and local vortices in front of the poles. The use of a SSM with the MFR-ST method leads to characteristic circumferential bands and may underestimate the pressure, velocity and turbulent kinetic energy.

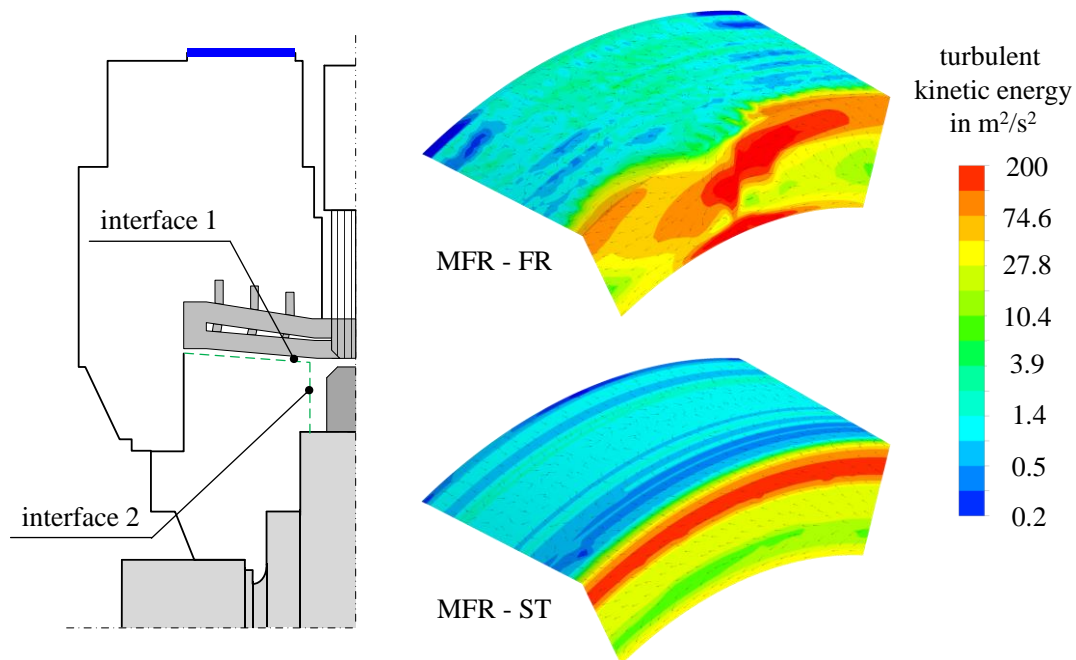


Figure 3.14: Turbulent kinetic energy on selected interfaces.

The comparison of results obtained by PSM 1 and SSM 1 are shown in Figure 3.15. The Nusselt numbers of PSM 1 are mostly higher than those of SSM 1. This is a plausible effect due to the higher computed velocities of the PSM. More particularly, there is a good agreement in zones with a straight downstream flow as in zones t1/ b1 and t2/ b2. A larger difference in zones t3/ b3 is present because of vortices at the end of the bars. These differences can also be seen very well in the velocity plots of the inlet and end winding region of PSM 1 and SSM 1 in Figure 3.16.

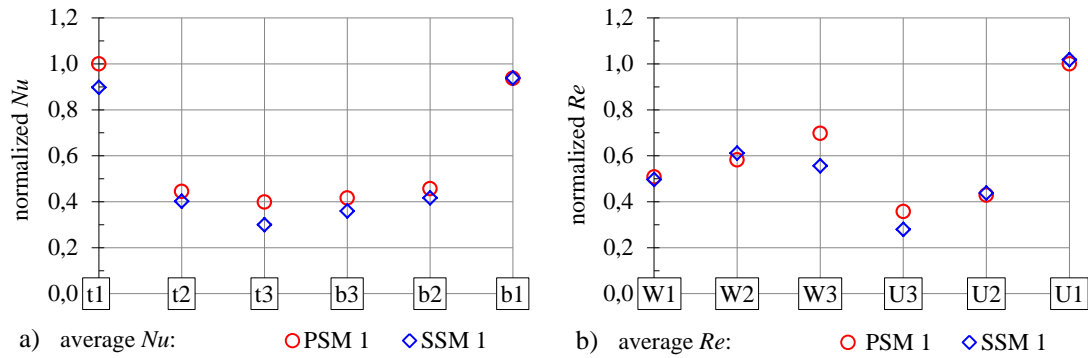


Figure 3.15: Comparison of PSM 1 and SSM 1: a)  $Nu$  distribution, b)  $Re$  distribution.

Figure 3.17a and 3.17b show a comparison of SSM 1 and 2. The mesh of the end winding domain is the same for both, but all other parts are meshed coarse (SSM 1) or in a medium quality (SSM 2) (see Table 3.3). Nearly no deviation between these two models can be seen in either graph. As a consequence, it is possible to use a coarser mesh in domains less influencing the HTC at the end winding bars. This saves elements and calculation time.

Figure 3.17c and 3.17d present the comparison of SSM 1 and 3. SSM 1 has a coarse mesh in the bar domain and SSM 3 a very fine one. The remaining parts are meshed coarse. According to Figure 3.11a and Figure 3.13a, a small  $y^+$  results in higher Nusselt numbers but it increases the amount of elements enormously.

The influence of the fluid properties is illustrated in Figure 3.17e and 3.17f. Two settings of materials have been used in this study, the standard ideal gas in ANSYS CFX and an adjusted one with temperature dependent fluid properties. The graphs show only a slight difference between the two models. Although this variation is negligible, the computational effort is the same for both models; therefore, the adjusted ideal gas is recommended to be used for further investigations of hydro generators.

Figure 3.17g and 3.17h depict the discrepancies between PSM 2 and SSM 3. Both models include a fine mesh in the end winding domain and a coarse mesh for the remaining components as well as the standard ideal gas without the adjusted fluid properties to get comparable results at the same conditions. The deviation of the Nusselt number between PSM 2 and SSM 3 in the zones t1/ b1 and t2/ b2 is in an acceptable range. The bars overlap in the zones t3/ b3 and the area between two bars is open in axial direction. The flow streams straight through the bar domain in PSM 2, but one part of the flow moves out in axial direction in SSM 3. Therefore, less mass flow is cooling the zones t3 and b3 in the SSM and the differences in these

zones are larger. Nevertheless the results in the other zones agree well. Figure 3.17h shows the same deviation for the Reynolds numbers in W3 and U3. Furthermore, the flow in the control surfaces W1 and W2 differs between the PSM and SSM because of higher velocities near the poles influencing the flow path in this region. Figure 3.16 shows the vector plot of the inlet and end winding regions with the different flow directions in the zones t3/ b3 and the higher velocity in front of the poles.

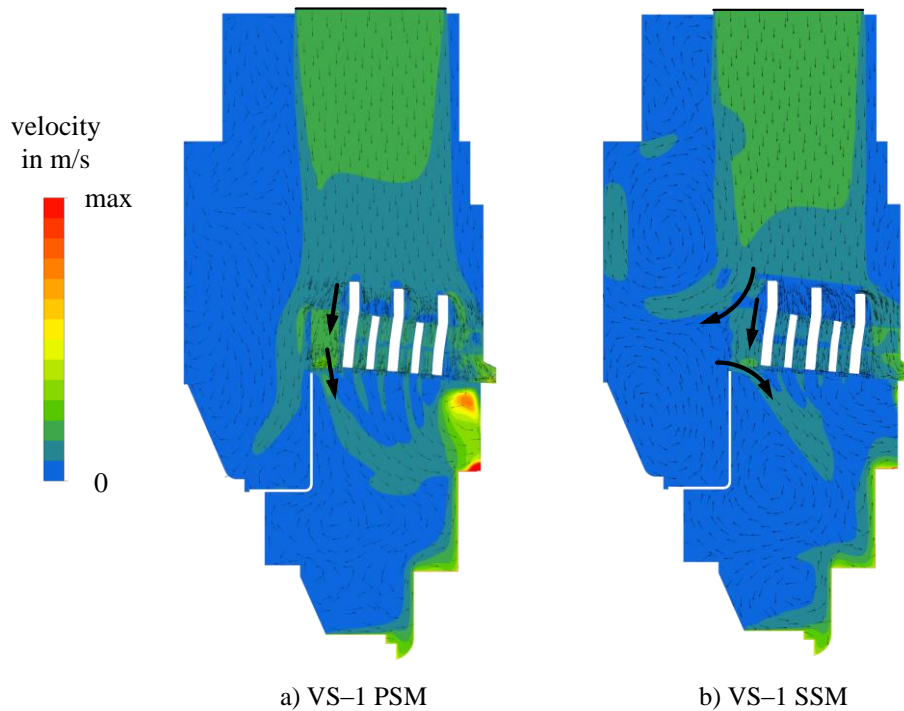


Figure 3.16: Comparison of PSM 1 and SSM 1: flow distribution at the inlet and end winding region.

The above investigations suggest the reduced model to be appropriate as an alternative simulation model for heat transfer investigations of large hydro generators. The MFR-ST interface averages all physical values which is an advantage for the evaluation of the results. The mesh of the end winding region results in sufficient accuracy for heat transfer predictions with an averaged  $y^+$  value of around 8 and the mesh for all other domains can be rather coarse to save elements. Furthermore, it is recommended to use an adjusted ideal gas and the SST turbulence model. The comparison of the SSM to a reference PSM has been also presented in [105].

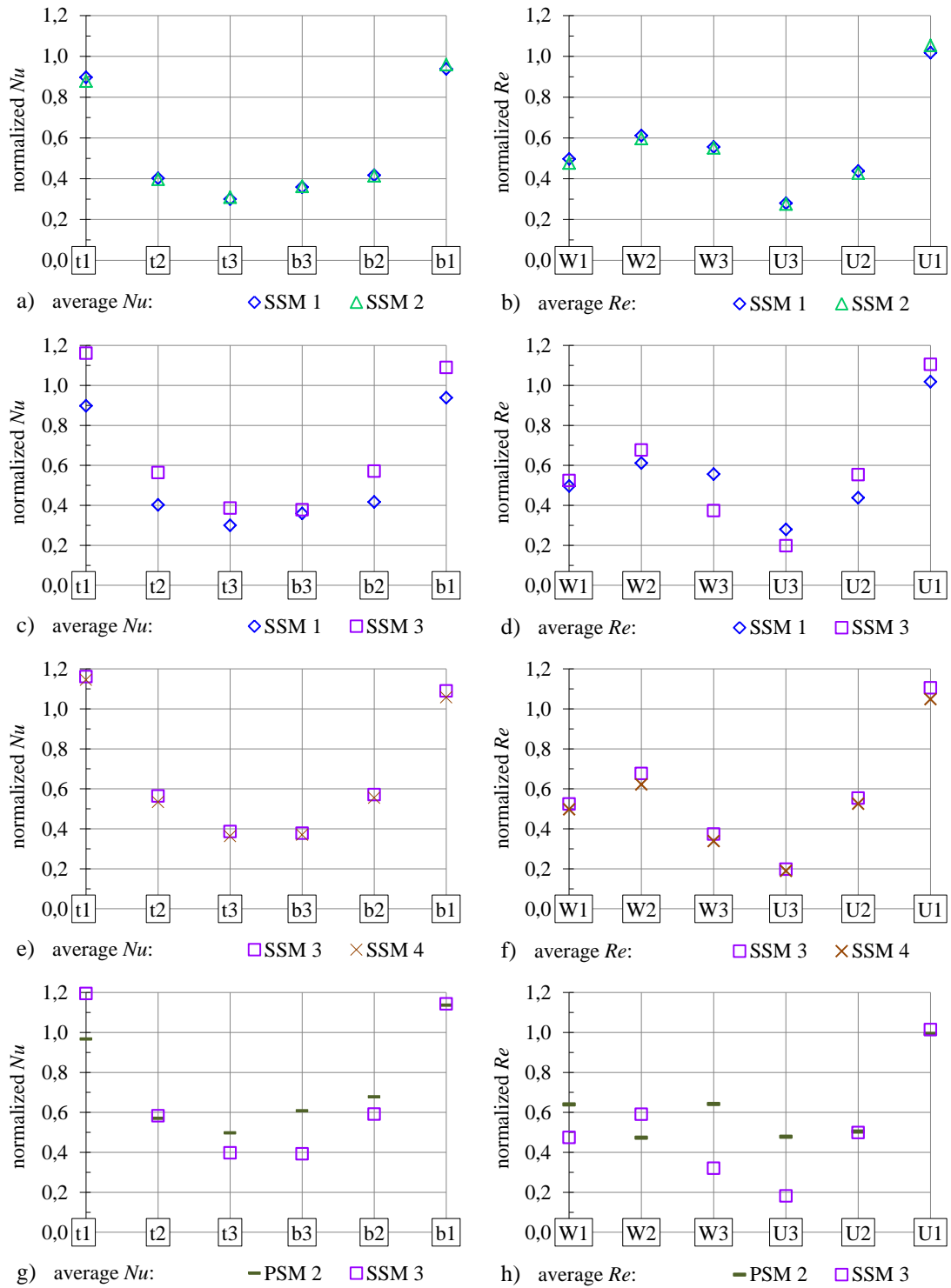


Figure 3.17: Comparison of various models:  $Nu$  distribution,  $Re$  distribution.

### 3.5.3 Comparison to transient results

Subsection 3.5.2 has described and compared the different CFD settings of the SSM for the cooling scheme VS-1. This ventilation scheme has the drawback of no fan swirl which substantially influences the cooling at the end winding bars. Hence, this section presents further comparisons of the SSM to MFR-FR employing transient simulations in VS-1, VS-4 and VS-6.

Figure 3.18 shows the values of  $Nu$  evaluated along an end winding bar. The curves in Figure 3.18a and 3.18b have the same shape along the whole bar. These results indicate that the reduced model computes the same flow conditions with the SSM for VS-1 and VS-4 as the larger PSMs. The velocity distributions of the cooling scheme VS-1 is illustrated in Figure 3.19a – 3.19c. All velocity plots look identical as regards the overall velocity magnitude and flow direction. The same applies to VS-4 in Figure 3.19d – 3.19f. Here, too, there is no large deviation between the PSMs and the SSM. Accordingly, these results confirm the very good agreement of the curves in Figure 3.18a and 3.18b.

The shapes of the curves in Figure 3.18c are similar in most zones. Only the zones t3 and b3 have a higher  $Nu$  value in the SSM simulations. These deviations can be attributed to different flows through the bars as obtained by the transient and steady-state analyzing methods. The velocity plots of VS-6 are shown in Figure 3.19g – 3.19i. The flow runs up in the zones t1 and b1 and down in t2 and b2. Furthermore it streams also down in t3 and b3 when using the steady-state computing approaches (see Figure 3.19h and 3.19i). The transient results in Figure 3.19g show more distinct vortices under the end winding bars as well as much lower velocities in the area above the bars. Another deviation between the transient and steady-state results is the flow direction in the zones t3 and b3. The air streams down in the zone t3 but slightly up with a sweep in the zone b3. Hence the graph in Figure 3.18c shows lower values in t3 and b3 for the transient approach. This validation has been also published in [107].

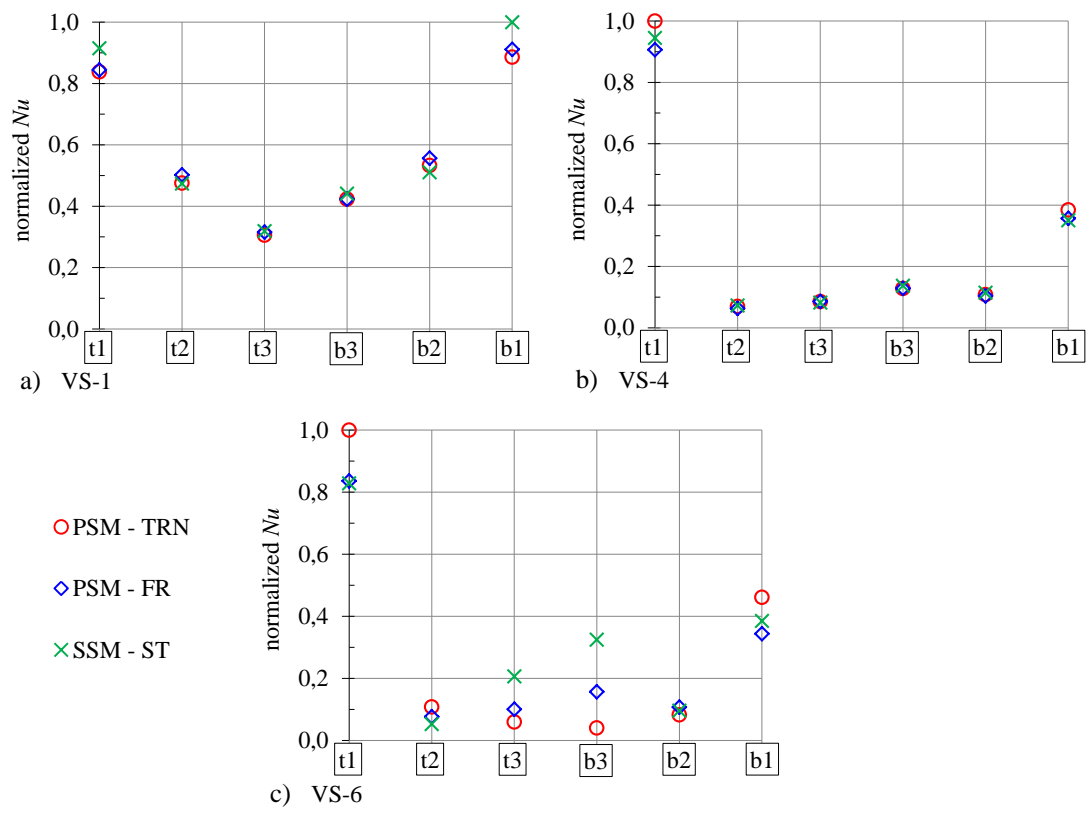


Figure 3.18: Normalized Nusselt number along a bar: a) VS-1, b) VS-4, c) VS-6.

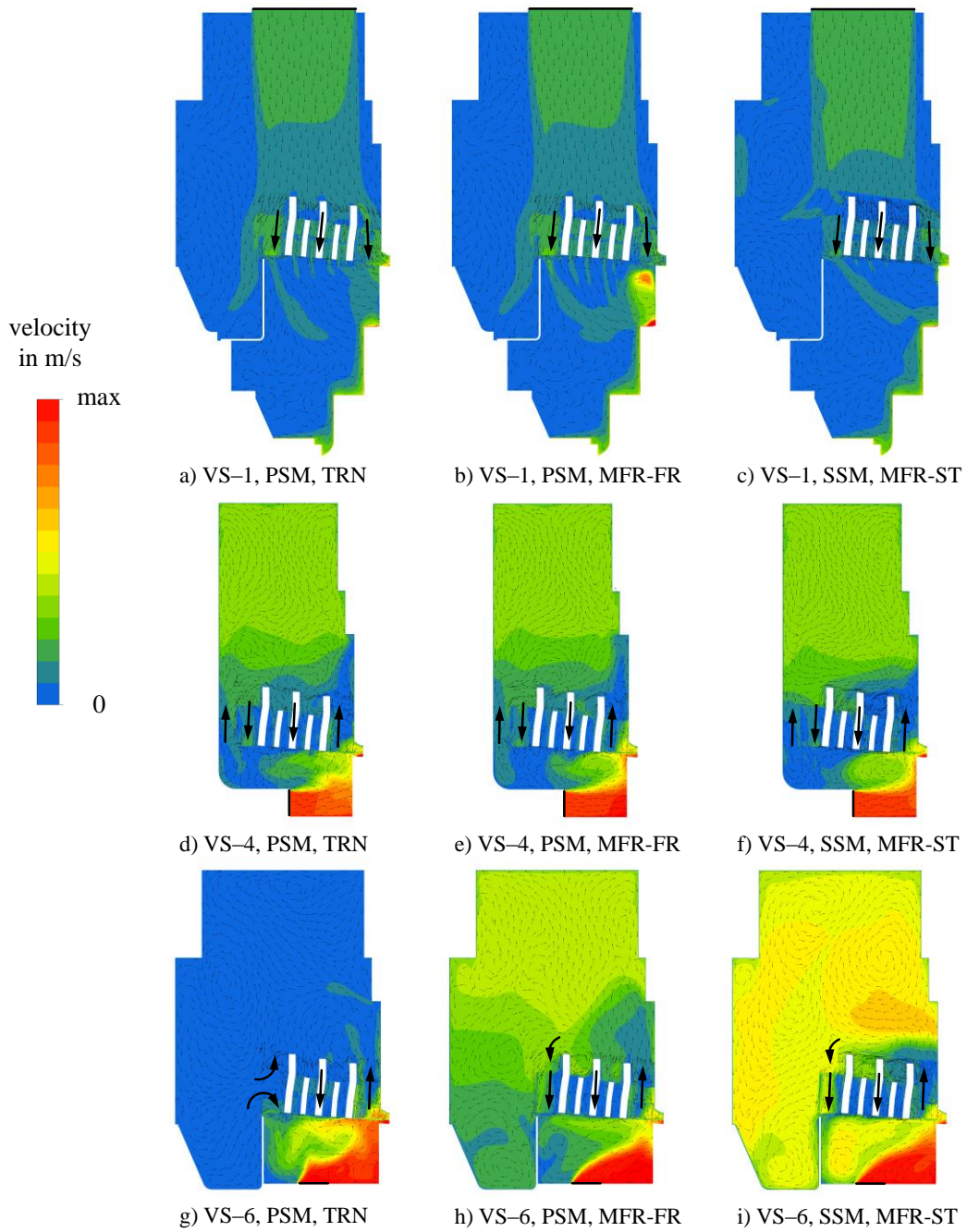


Figure 3.19: Velocity at the inlet and end winding region for different simulation methods and ventilation schemes.

### 3.5.4 Comparison of the computational time

One important objective of this work is finding a simple and accurate simulation model to speed up the CFD computation of electrical machines. This is essential for the parametric study requiring several hundred different variations of the ventilation schemes, mass flow rate, rotational speed or absolute fan velocity. The average computing times of the three numerical models of section 3.5.3 are presented in Table 3.4. The SSM reduces the analysis time per iteration to about one third compared to the conventional PSM with MFR-FR. The most time expensive approach is the transient PSM. This is not surprising, since transient simulations require huge computing resources.

The CFD simulations have been carried out with the same computer to ensure comparability of the analysis times. The server setup was an Intel Xeon 12 cores/ 3.47GHz/ 192GB RAM/ 64-bit, using 4 cores per simulation.

	Analysis time per iteration
PSM – TRN	5 min 45 sec
PSM – MFR-FR	5 min
SSM – MFR-ST	1 min 30 sec

Table 3.4: Average analysis time per iteration for the various simulation approaches.

## 3.6 Heat conduction models

The validation of the approximate model of chapter 5 has been carried out by heat conduction computations as well as comparisons with measurements in chapter 6. On the one hand, heat conduction (HC) simulations are performed with the solid domain of the bar only and on the other hand, a fluid simulation of the complete SSM of section 3.3 including the solid domain of the end winding in addition to the fluid region can be used to identify the wall temperatures of the bars. This combination of CFD and HC is called conjugate heat transfer in ANSYS CFX.

### 3.6.1 Heat conduction of the end winding bar

The heat conduction model of the end winding bars has a simple design and the corresponding simulations are hence also very fast. This model is built up of the solid domain only shown in Figure 3.20. The composite structure of the bar is illustrated in Figure 2.10a. This composite material with conductors and coating has been reduced to one homogenized part with an anisotropic thermal conductivity described in subsection 2.3.1. The homogenized composite material with the thin insulation surrounding it is presented in Figure 2.10b. Both parts have been separately meshed with hexahedral elements in ANSYS ICEM CFD [102]. The bar walls with contact to the support rings or the space brackets are modelled as adiabatic surfaces (see Figure 3.20).

ANSYS CFX is also capable of analyzing such simple heat conduction problems without a fluid domain [46]. Therefore, a convective heat transfer coefficient has been calculated with the HTM of chapter 5 and used as a boundary condition for the walls of the HC model. Indeed, it is sufficient to solve the heat conduction equation (2.52) with the Cauchy boundary condition:

$$-\lambda \cdot \frac{\partial T}{\partial n} = \alpha \cdot (T_w - T_\infty) \quad (3.4)$$

where  $n$  is the direction normal to the wall,  $T_w$  is the temperature at the wall and  $T_\infty$  a reference temperature which has been the air inlet temperature for these cases. The heat source is a constant heat loss density.

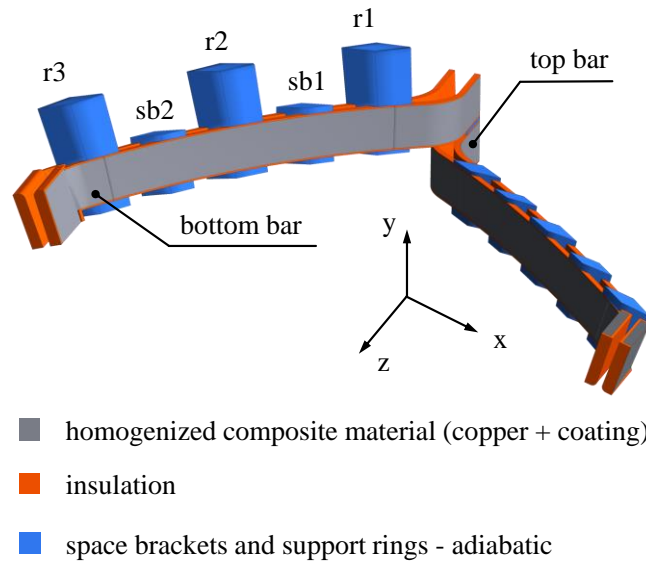


Figure 3.20: Heat conduction model of the end winding bar.

### 3.6.2 Conjugate heat transfer model

In addition to the pure heat conduction or the pure fluid dynamics simulations the reduced model of Figure 3.6 has been assembled with the HC model of Figure 3.20 to the conjugate heat transfer model (CHT). The CHT application in ANSYS CFX enables the computation of the heat transfer in solid domains in conjunction with the flow domains [46]. The fundamentals of heat conduction have been described in subsection 2.3.1 and the theory of fluid dynamics is given in section 2.2.

The boundary conditions of the SSM for CHT are the same as for the CFD computations described in section 3.4.2, except that the end winding wall temperature is not assumed to be constant any longer. However, a constant heat loss has been applied as the thermal source in the solid domain. Due to that, the temperature of the wall is computed by the heat conduction equation (2.52) simultaneously to solving the Navier-Stokes equations of the fluid, i.e. the thermal source is heating the bar by conduction and the flow through the end winding bars is cooling them by convection. This interaction requires far more iterations steps to find a convergent solution of the numerical equation system. For example, a CFD computation of the SSM takes about one and a half day and the appropriate CHT simulation 7 to 10 days. Hence, the CHT simulations have been carried out in section 6.2 for three different ventilation schemes only (VS-1, VS-4 and VS-6).

---

## 4 Results of the parametric study

The parametric study has been carried out for the 15 different ventilation schemes presented in Table 3.1. Every scheme has been computed with up to 20 different variations of the boundary conditions to get sufficient data to establish the correlation between the HTM and the CFD results in chapter 5. All in all, more than 230 different CFD simulations have thus been carried out. This section presents some essential results to give an overview of the advantages and disadvantages of the schemes regarding cooling.

### 4.1 Comparison of the ventilation schemes

The values of the Nusselt numbers along the end winding bars have been normalized by the maximal  $Nu$  value obtained for VS-3. This serial ventilated scheme is not influenced by a fan or pole rotation and hence it is suitable to illustrate the impact of the cooling air flow on the end winding region without rotating parts. To show such impacts, velocity vector plots illustrating the flow directions in the inlet and end winding region are presented below for each ventilation scheme. To facilitate comparison, similar boundary conditions have been prescribed in each test case shown in Figure 4.1 to Figure 4.6.

Figure 4.1 presents  $Nu$  along the bars and Figure 4.2 the velocity plots of VS-1, VS-2 and VS-3, respectively. VS-3 has the most homogenous flow to the bars and therefore a homogenous  $Nu$  distribution is observed along the bar in axial direction. This scheme is shielded from the poles. As a consequence, the flow of the rotor does not influence the ventilation of the bars and  $Nu$  near the stator is much lower than for

the two other schemes. The external ventilation is radial in VS-1 and axial in VS-2 with no shielding present in either case. Hence the normalized Nusselt number near the stator is much higher than in VS-3. The four other zones have nearly the same  $Nu$  values. Furthermore, these three schemes produce a straight flow through the bars with no larger vortices in the end winding region.

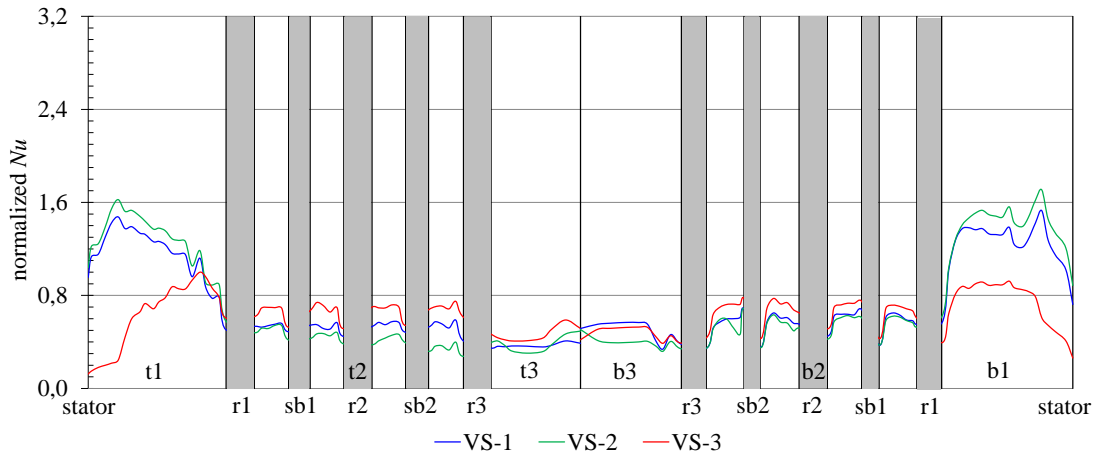


Figure 4.1:  $Nu$  comparison of VS-1, VS-2 and VS-3.

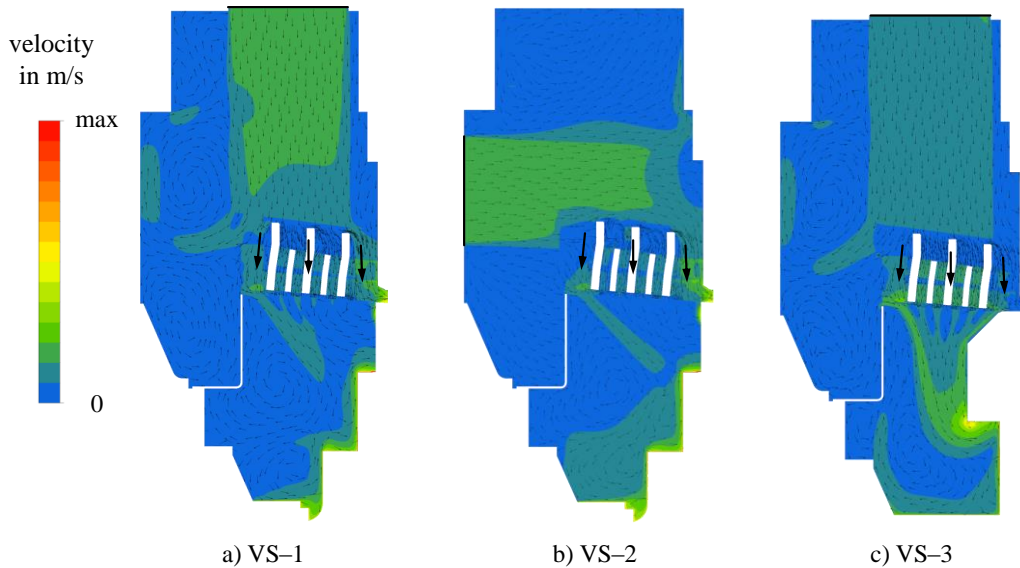


Figure 4.2: Velocity plots of VS-1, VS-2 and VS-3.

The next velocity plots and  $Nu$  graphs are shown in Figure 4.3 and Figure 4.4 for the two axial fan mounted schemes. Due to the bypass opening, more mass flow

streams through the end winding bars and hence, VS-5 has a higher flow velocity at the bars than VS-4 and  $Nu$  along the bars is larger. Substantial differences can be also seen in zone t1 comparing the axial fan schemes with VS-3. On the one hand the fan generates a high swirl and accelerates the flow at the zone t1 enormously. On the other hand the momentum causes vortices, flow separations and backflow in the zones t2 and b2 where the bars cross each other and have a large drag. Due to this,  $Nu$  is very small in these two zones.

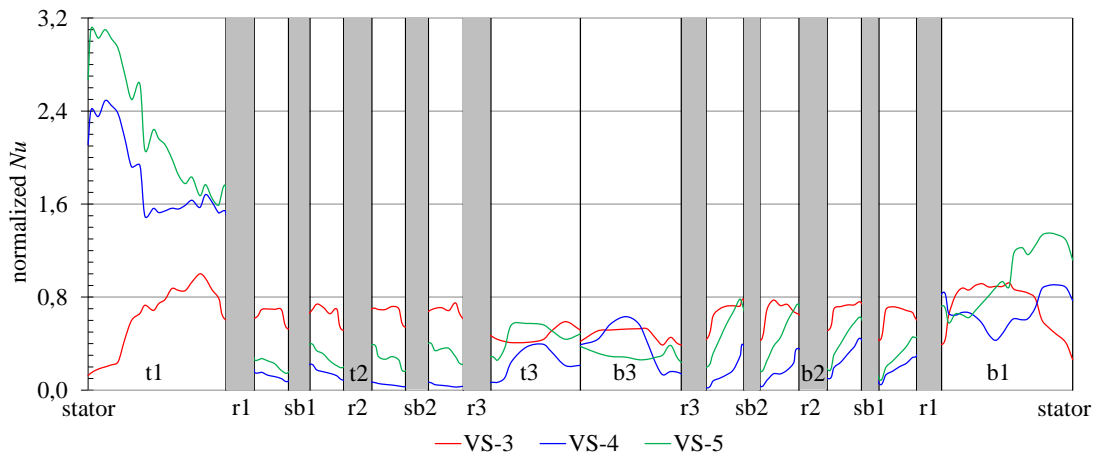


Figure 4.3:  $Nu$  comparison of VS-3, VS-4 and VS-5.

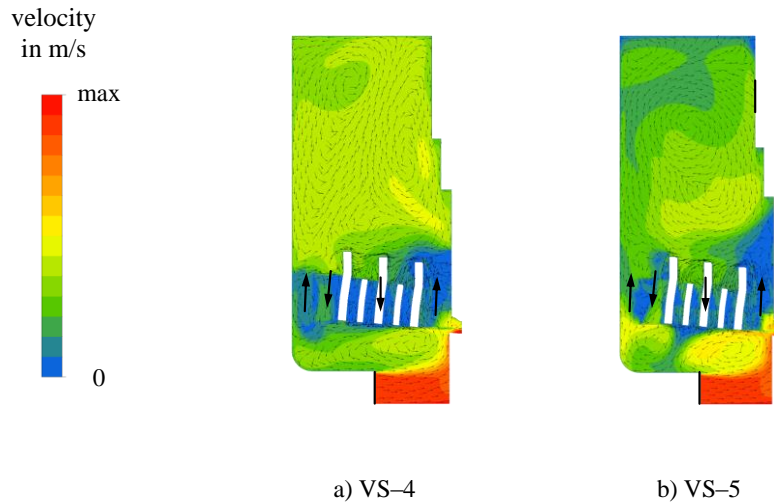


Figure 4.4: Velocity plots of VS-4 and VS-5.

The comparison of the radial shaft mounted ventilation schemes is shown in Figure 4.5 and Figure 4.6. These investigations of the cooling schemes VS-6 – VS-

15 have revealed the alternating flow directions of the radial fan ventilation. The flow streams normally from the fan to the poles or up through the zones t1 and b1. However, the main flow tends to occur in the zones t3 and b3 or beside the end of the bars if the fan is located close to the guiding plate and the absolute fan velocity is very high (see Figure 4.6g and 4.6j). An estimation introduced in subsection 4.2 describes these phenomena in more detail.

The axial location of the fan has an influence on the heat transfer in the zones t1 and b1 only (see VS-6, VS-7 and VS-8 in Figure 4.5). The inclusion of a guiding plate does not influence the cooling much if the flow streams to the poles. This can be seen very well at the nearly similar shapes and velocity plots of VS-6 and VS-11. Furthermore, a lower fan diameter affects the cooling of t1, wherefore  $Nu$  is higher in this zone for VS-9 and VS-10 compared to VS-6 and VS-7. The best cooling has been reached in t1 with VS-14 and in all other zones with VS-3 if we ignore the different flow direction of VS-12 and VS-15. Nevertheless, the overall  $Nu$  of VS-12 and VS-15 is higher than VS-3 because the flow streams up with a high momentum along the end winding and down through the bars. This indicates that VS-12 and VS-15 are very efficient cooling schemes.

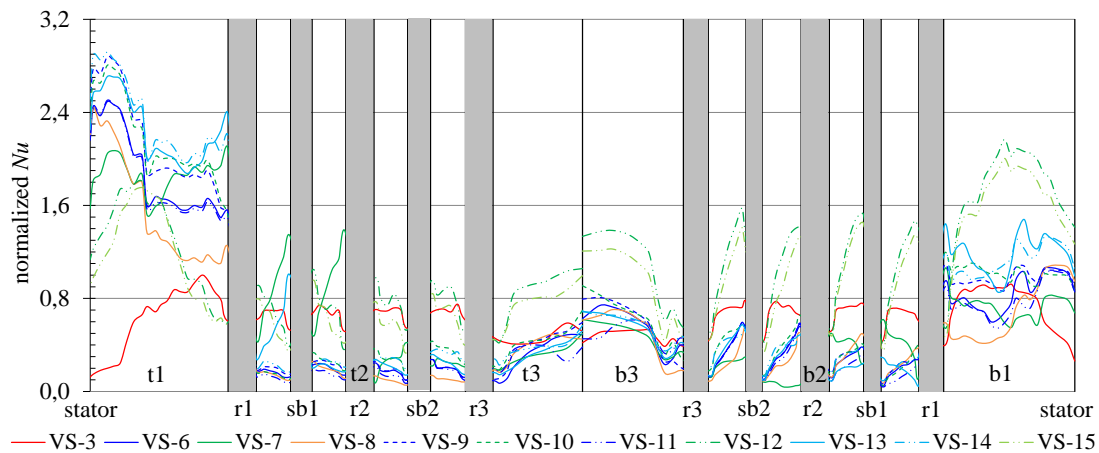


Figure 4.5:  $Nu$  comparison of VS-3, VS-6 to VS-15.

In summary it can be said, that VS-3 has the most homogeneous averaged heat transfer along the bars. The highest local  $Nu$  has been reached with VS-5 and VS-14 in zone t1. Both schemes have a bypass opening. An overview of this parametric study as well as the advantages and disadvantages of the various ventilation schemes have been presented in [108].

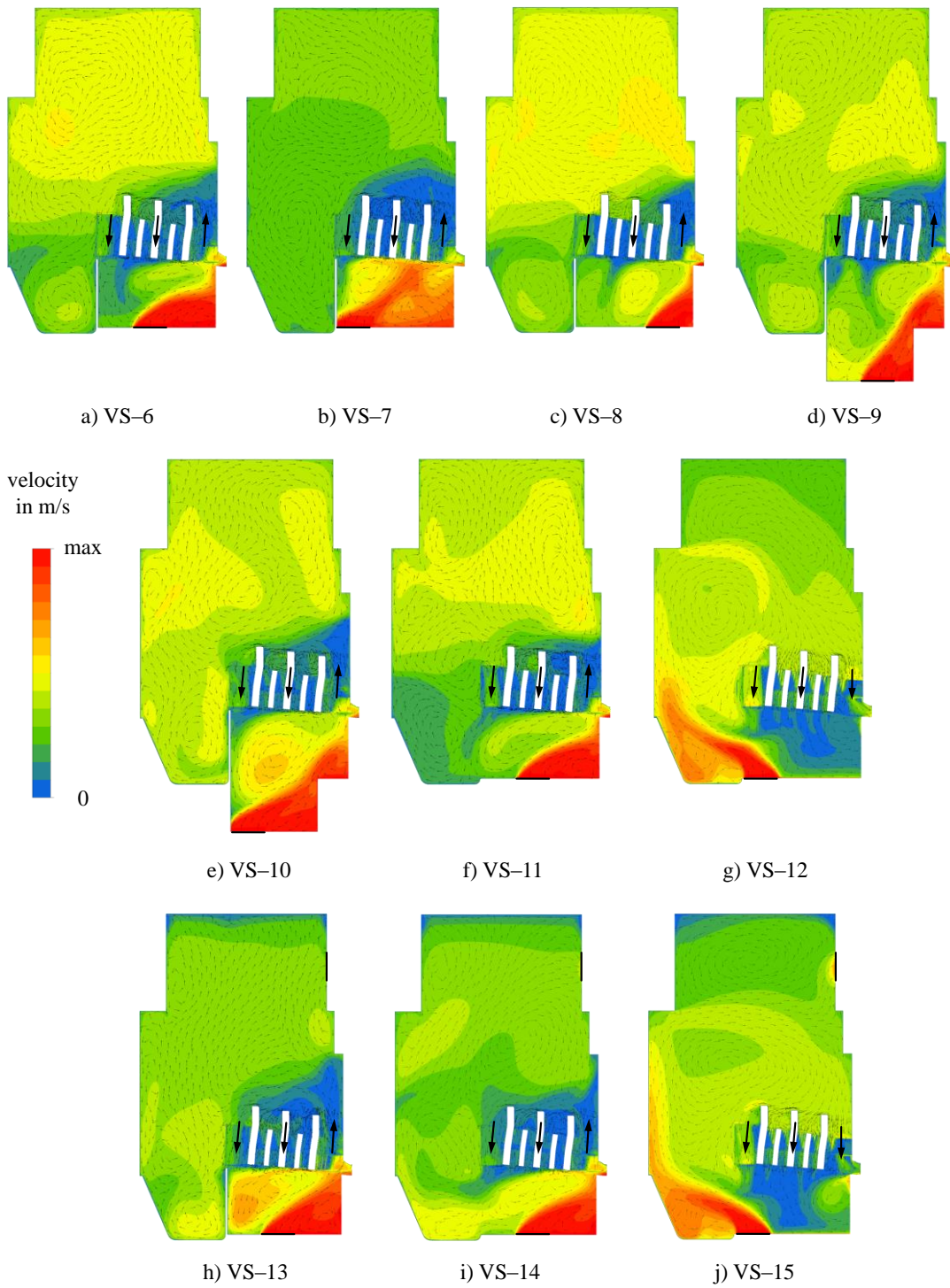


Figure 4.6: Velocity plots of VS-6 to VS-15.

In summary, the decision on the appropriate ventilation scheme is very difficult and must be chosen in coordination with the entire project. For example, an external ventilation system requires a lot of space around the generator for the fan and the heat exchangers which is not always structurally possible. It must also be kept in mind that the air flow has to transport the heat away from the pole and stator duct walls too after cooling the end winding bars. Another point is that most hydro generators are unique machines having to comply with diverse customer requirements.

## 4.2 Flow direction for radial fan schemes

The phenomenon of an alternating flow direction by radial shaft mounted schemes has been pointed out in the previous section. A very high absolute velocity  $c_{F2}$  at the fan outlet and/or a large length of the fan position  $L_F$  can lead to a change of the flow direction, i.e. most of the flow streams up at the end of the bar or besides and down near the stator. The CFD results of the parametric study have shown that the likelihood of a flow from the inlet to zone t3 is very high under the conditions  $c_{F2} > 70$  m/s,  $L_F / L_E \approx 1$  which especially fit VS-7, VS-12 and VS-15. However, the likelihood for such a flow phenomenon is very low for all other schemes because the ratio  $L_F / L_E$  is smaller than 1. Figure 4.8 shows examples for the two different flow directions at the schemes VS-7, VS-12 and VS-15.

A quantity characteristic for the flow direction for radial fan schemes can be estimated as

$$\theta_{flow} = \Psi_3 \cdot \Phi_1 \cdot \Phi_2 \cdot \Phi_{GB} \quad (4.1)$$

with the geometry ratios  $\Phi_1$  and  $\Phi_2$ , the geometry coefficient  $\Phi_{GB}$  and the velocity ratio  $\Psi_3$ .  $\Phi_1$  is defined with the length of the fan and the end winging bar and  $\Phi_2$  includes the fan and pole radius. The constant  $\Phi_{GB}$  considers the arrangement of the guiding plate with the radius  $R_{GB}$ . The relevant velocity parameter  $\Psi_3$  in (4.1) is determined with the absolute and circumferential fan velocity.

The flow tendency is governed by the following considerations:

$$\begin{aligned}
 \theta_{flow} \leq \theta_{flow.min} & \rightarrow \text{main flow t1/ b1} \\
 \theta_{flow.min} < \theta_{flow} < \theta_{flow.max} & \rightarrow \text{transition zone} \\
 \theta_{flow} \geq \theta_{flow.max} & \rightarrow \text{main flow t3/ b3}
 \end{aligned} \tag{4.2}$$

Both directions are possible in the transition zone whereby the velocity  $c_{F2}$  has to be very high. Equation (4.1) is used in developing the HTM in section 5 to estimate the flow path and determine the proper mass flow rate through the bars.

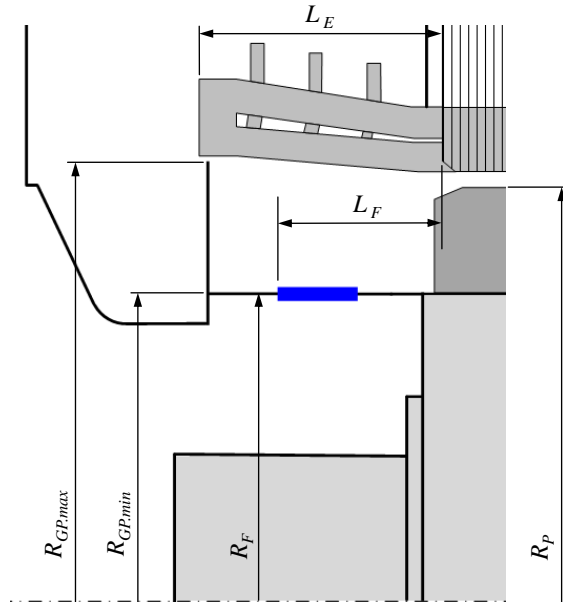


Figure 4.7: Important dimensions at the inlet region.

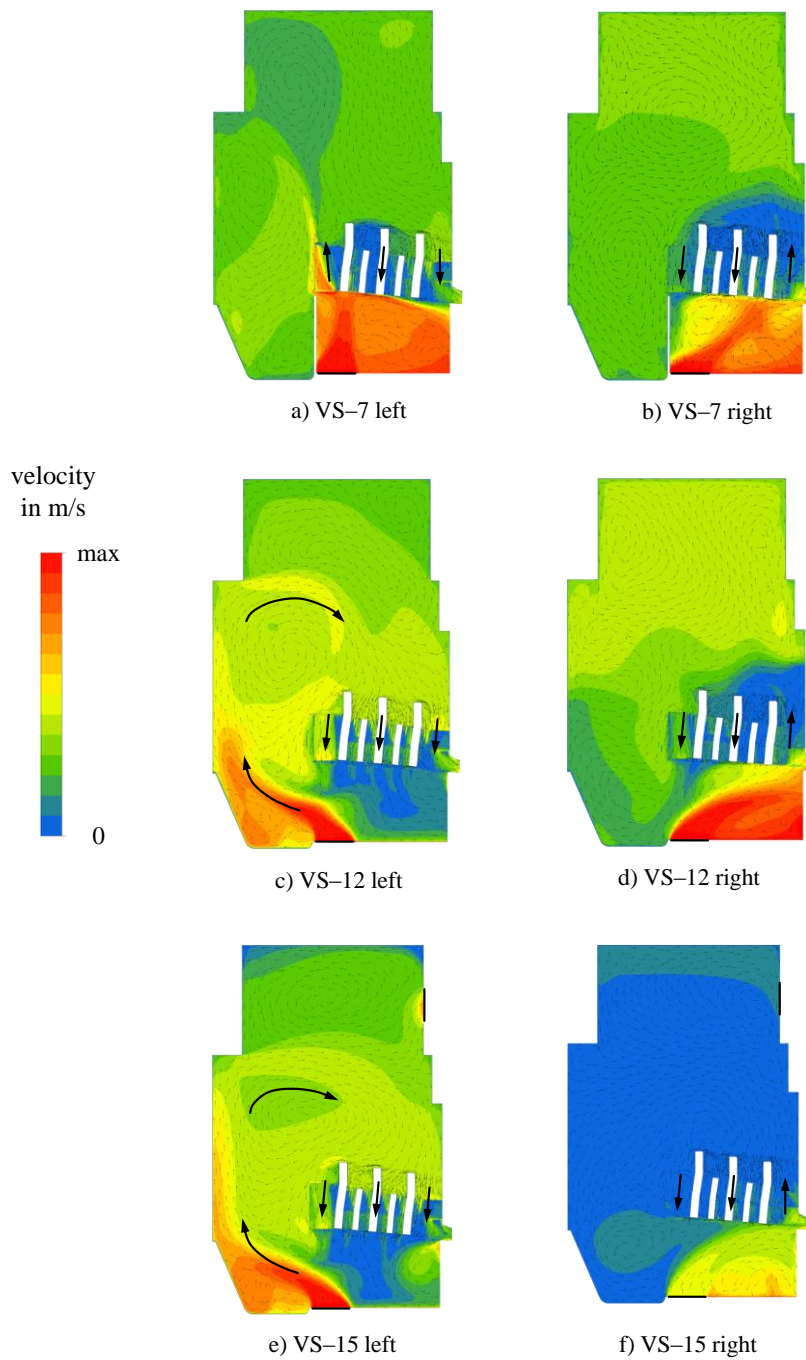


Figure 4.8: Velocity plots of VS-7, VS-12 and VS-15 with different flow directions.

## 5 Heat transfer model

The heat transfer model (HTM) is an approximate model for calculating the HTC at the end winding bars of large hydro generators with the fluid properties, important dimensions and inflow parameters as input variables resulting finally in the HTC for the end winding bars. This model will be implemented in a thermal lumped parameter network at ANDRITZ HYDRO GmbH to predict the thermal behaviour of large hydro generators in the first design step. Due to the complexity of the thermal problem in electrical machines, numerical simulation methods like electromagnetic FEM or CFD are not used in the initial phase of the design process. For this reason, flow and thermal networks are the state-of-the-art approaches in the first design step. Airflow networks calculate the cooling airflow through the whole machine and the computation of the thermal flow and surface temperatures is carried out by thermal networks. Analytical lumped parameter thermal models are simple and very fast but necessitate input parameters like the average convective wall heat transfer coefficient (HTC), a reference air temperature or the machine losses to calculate the temperatures of the various parts [21, 109].

This following chapter describes the estimation HTM based on a mass flow rate at the inlet, calculating the velocity through the bars to determine Reynolds numbers and characterize a Nusselt number formula of (2.62). Furthermore, the influence of the different ventilation schemes on the cooling of the end winding bars has been taken into account by setting up a polynomial expression of dimensionless numbers. Finally, the bars are divided into 6 zones (see Figure 5.1) to predict local HTCs and optimize the thermal network.

Some examples of Nusselt number formulations for the end winding bars of different electrical machines have been described in subsection 2.3.2. The non-

dimensional formulation is used to enable the scalability with specific characteristic dimensions and flow conditions. Non-dimensional values can be the Reynolds, Prandtl and Nusselt numbers, but also geometry and velocity ratios or relevant material properties.

The necessary input parameters for the HTM are the fluid properties at the ventilation inlet, the dimensions of the end winding bars and the inlet guiding frame as well as several mass flow rates and fan velocities. Table 5.1 shows all input variables of the HTM.

fluid properties	geometry	flow
<ul style="list-style-type: none"> <li>• air temperature <math>T_{Air}</math>,</li> <li>• density <math>\rho_{Air}</math>,</li> <li>• thermal conductivity <math>\lambda_{Air}</math>,</li> <li>• dynamic viscosity <math>\mu_{Air}</math>,</li> <li>• specific heat capacity <math>c_{p,Air}</math>.</li> </ul>	<ul style="list-style-type: none"> <li>• radius fan <math>R_F</math>,</li> <li>• length fan <math>L_F</math>,</li> <li>• length bar <math>L_E</math>,</li> <li>• radius pole <math>R_P</math>,</li> <li>• height bar <math>H_{Bar}</math>,</li> <li>• width bar <math>B_{Bar}</math>,</li> <li>• distance of 2 bars <math>B_{Gap}</math>,</li> <li>• area bar walls <math>A_W</math> (b1, b2, b3, t1, t2, t3),</li> <li>• area between 2 bars <math>A_L</math> (U1, U2, U3, W1, W2, W3).</li> </ul>	<ul style="list-style-type: none"> <li>• mass flow rate inlet <math>\dot{m}_I</math>,</li> <li>• mass flow rate bypass <math>\dot{m}_{By}</math>,</li> <li>• mass flow rate finger ducts <math>\dot{m}_F</math>,</li> <li>• rotational speed <math>n</math></li> <li>• absolute fan velocity, <math>c_{F2}</math>.</li> </ul>

Table 5.1: Input parameters HTM.

The following subsection 5.1 presents the final HTM for a thermal network to calculate the HTC in dependence of the inlet dimensions and velocities. Subsequently, section 5.2 describes the calculation process of the Nusselt number  $Nu_0$ .

## 5.1 Characterization of the heat transfer coefficient

The parametric study in chapter 4 has identified large differences in the cooling air flow through the machine between setups using various ventilation methods. Due to this, four separate HTMs have been developed for the ventilation schemes:

- HTM-e ... external → VS-1, VS-2,
- HTM-s ... serial → VS-3,
- HTM-a ... axial fan → VS-4, VS-5,
- HTM-r ... radial fan → VS-6 – VS-15.

Nevertheless, the HTM formulation is similar for every cooling method and a variation of the model will be explained in the following paragraphs. Furthermore, the definition of the HTM for the top and bottom bar is identical and differs only in the values of the coefficients and exponents. As mentioned above, the HTM is based on the non-dimensional approach of (2.62) in combination with a polynomial and can be written for the axial and radial fan schemes as

$$Nu = Nu_0 \cdot \underbrace{\left(1 + C_{\Psi_1} \cdot \Psi_1^{\varepsilon_1} + C_{\Psi_2} \cdot \Psi_2^{\varepsilon_2}\right)}_{\text{velocity influence}} \cdot \underbrace{\left(C_{\Phi_0} + C_{\Phi_1} \cdot \Phi_1 + C_{\Phi_2} \cdot \Phi_2\right)}_{\text{geometry influence}}. \quad (5.1)$$

$Nu_0$  is an independent Nusselt number, i.e. it is not affected by the fan location or the geometry of the inlet frame (guiding plates, bypass and finger openings). The second term describes the influence of the fan velocities on the bar cooling.  $\Psi_1$  is the velocity parameter to show the influence of the fan and the pole momentum.  $\Psi_2$  is defined by the pole speed and the velocity between two bars  $w_L$ . The velocity  $w_L$  is described in (5.15) and the pole speed can be written as

$$u_p = \frac{n \cdot \pi}{30} \cdot R_p. \quad (5.2)$$

The third term characterizes the fan location and the inflow geometry.  $\Phi_1$  and  $\Phi_2$  have been defined in subsection 4.2.

The parametric study has yielded area averaged HTC values for the top and bottom bar of every ventilation scheme and boundary condition. These HTCs are expressed as Nusselt numbers and then used as the reference parameter for the least

squares method to identify the constants  $C_{\Psi_1}$ ,  $C_{\Psi_2}$ ,  $C_{\Phi_0}$ ,  $C_{\Phi_1}$  and  $C_{\Psi_2}$  by minimizing the error  $R$  between the calculated values of (5.1) and the CFD results [110]:

$$\sum_{i=1}^n (Nu_{HTM} - Nu_{CFD})^2 = R. \quad (5.3)$$

The exponents  $\varepsilon_1$  and  $\varepsilon_2$  have been randomly changed between 0 and 1.

Since the external ventilation schemes have no shaft mounted fan the coefficients  $\Psi_1, \Phi_1$  and  $\Phi_2$  are 0 and (5.1) is simplified to

$$Nu = Nu_0 \cdot (1 + C_{\Psi_2} \cdot \Psi_2^{\varepsilon_2}). \quad (5.4)$$

Furthermore, the ratio  $\Psi_2$  is also 0 for the serial ventilation scheme because of the shielding between the end winding region and the rotor. An alternative equation with the Reynolds number between two bars ( $Re_L$ ) considers an adjustment of  $Nu$  for this cooling scheme with

$$Nu = Nu_0 \cdot (1 + C_{\Psi} \cdot Re_L). \quad (5.5)$$

The final Nusselt number of (5.1) is an average value of the top or bottom bar along the length  $L_E$ . The distribution of  $Nu$  over the various zones is obtained by the coefficients  $f_{ij}$  which have been determined from the CFD results:

$$Nu_{ij} = Nu \cdot f_{ij} \quad (5.6)$$

The subscript  $i$  stands for the top ( $t$ ) or bottom ( $b$ ) bar and  $j$  for the zones along the bar (1, 2, 3).

Consequently, the required HTC for a thermal network is obtained for each zone at the end winding as

$$\alpha_{ij} = \frac{Nu_{ij} \cdot \lambda_{Air}}{2 \cdot B_{Gap}}. \quad (5.7)$$

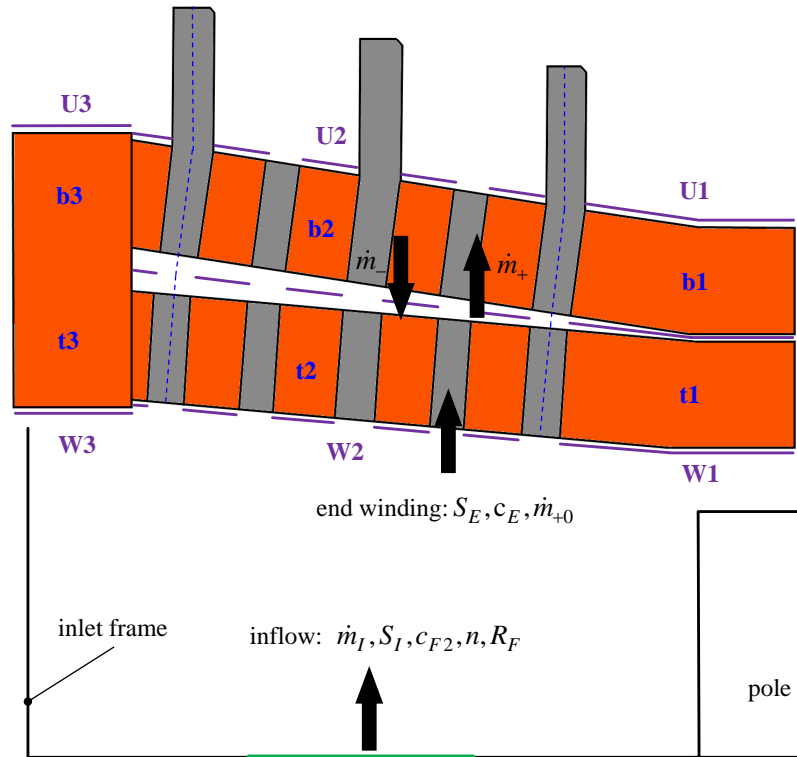


Figure 5.1: Flow parameters and dimensions at the end winding and inlet region.

## 5.2 Calculation of the independent Nusselt number

The definitions and relations in this subsection 5.2 are based on report [111]. A scaling of the bar dimensions  $H_{Bar}$ ,  $B_{Bar}$  and  $B_{gap}$  has not been done while performing the parametric study. As mentioned above, the Nusselt number  $Nu_0$  is unrelated to the fan location and the inlet frame geometry and can be defined with the area average heat transfer coefficient  $\alpha_0$  similar to (2.58) as

$$Nu_0 = \frac{\alpha_0 \cdot 2 \cdot B_{Gap}}{\lambda_{Air}}, \quad (5.8)$$

where  $\alpha_0$  depends on the bar dimensions and flow conditions through the bars and is then defined as

$$\alpha_0 = \frac{\frac{1}{2} \cdot B_{Bar} \cdot (\alpha_{up} + \alpha_d) + H_{Bar} \cdot \alpha_L}{B_{Bar} + H_{Bar}}. \quad (5.9)$$

The subscript  $L$  indicates the flow through the bars,  $up$  the inflow between the bars at the upstream side and  $d$  the outflow at the downstream side (see Figure 5.2). The heat transfer coefficients  $\alpha_L$ ,  $\alpha_{up}$  and  $\alpha_d$  are related to the specific walls in Figure 5.2 and can be determined similarly to (2.62) with the Reynolds and Prandtl numbers:

$$\alpha_L = a \cdot Pr^b \cdot Re_L^c, \quad \alpha_{up} = a \cdot Pr^b \cdot Re_{up}^c \quad \text{and} \quad \alpha_d = a \cdot Pr^b \cdot Re_d^c \quad (5.10)$$

where  $Pr$  is determined by the inlet fluid properties

$$Pr = \frac{\mu_{Air} \cdot c_{p,Air}}{\lambda_{Air}}. \quad (5.11)$$

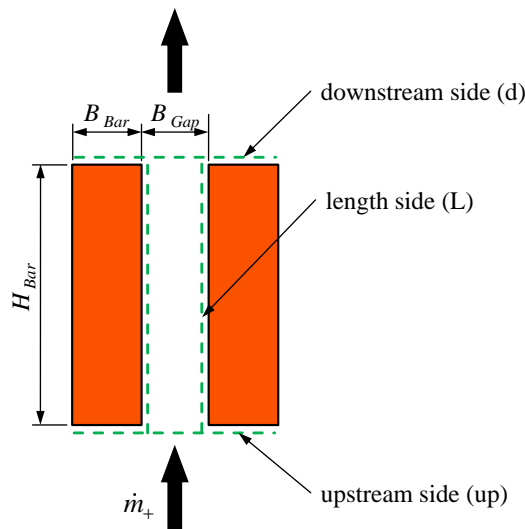


Figure 5.2: Control surfaces of a bar.

The Reynolds numbers in (5.10) will be obtained by means of the mass flow rate through the bars  $\dot{m}_L$  which in turn can be obtained with assumptions of the air flow in the inlet region in subsection 5.2.1 and 5.2.2, respectively. These Reynolds numbers for the various control surfaces around a bar are defined with the formula of (2.19) for the upstream side as

$$Re_{up} = \frac{\rho_{air} \cdot w_{up} \cdot B_{Bar}}{\mu_{Air}}, \quad (5.12)$$

for the length side as

$$Re_L = \frac{\rho_{air} \cdot w_L \cdot 2 \cdot B_{Gap}}{\mu_{Air}} \quad (5.13)$$

and for the downstream side as

$$Re_d = \frac{\rho_{air} \cdot w_d \cdot B_{Bar}}{\mu_{Air}} \quad (5.14)$$

The radial velocity between two bars is determined by the mass flow rate of (5.19) for external ventilation and (5.27) for shaft mounted fan cooling as

$$w_L = \frac{\dot{m}_L}{\rho_{Air} \cdot A_L} \cdot f_L \quad (5.15)$$

$A_L$  is the area of the control surfaces between the bars (U1 – U3 and W1 – W3 in Figure 5.1):

$$A_L = \sum_{i=1}^3 A_{Ui} \text{ or } A_L = \sum_{i=1}^3 A_{Wi} \quad (5.16)$$

$f_L$  is an adjustment coefficient found by correlating  $w_L$  of the HTM to the CFD results. The velocity at the upstream side of the bars is obtained by

$$w_{up} = w_L \cdot \frac{B_{Gap}}{B_{Bar} + B_{Gap}} \quad (5.17)$$

and the velocity at the downstream side is assumed to fulfil

$$w_d = w_L \quad (5.18)$$

Figure 5.1 also illustrates the inlet region with the end winding bars for a radial fan cooled generator. Note that the mass flow rates are all absolute quantities. The flow direction through the bars is specified for the mass flow with the subscripts + and -. This sign rule applies for external ventilated generators as well.

### 5.2.1 Mass flow through bars with external cooling

The calculation of  $\dot{m}_L$  is very simple for the external and serial ventilation schemes. The whole mass flow at the inlet streams down ( $\dot{m}_-$ ) through the bars and the upstream mass flow of the poles  $\dot{m}_+$  is negligibly small. Therefore, the total mass flow rate can be assumed to satisfy

$$\dot{m}_L = \dot{m}_- = \dot{m}_I. \quad (5.19)$$

### 5.2.2 Mass flow through bars with shaft mounted cooling

The estimation of  $\dot{m}_L$  for the axial and radial fan cooled schemes is more complex. We start with the calculation of the momentum of the fan. The given parameters at the inlet of the system are the mass flow rate  $\dot{m}_I$ , the rotational speed of the rotor  $n$  and the absolute velocity  $c_{F2}$  at the fan outlet. The momentum of the fan can be written with these three variables as

$$S_F = \dot{m}_I \cdot c_{F2} \cdot u_{F2} \quad (5.20)$$

where the circumferential velocity of the fan is defined as

$$u_{F2} = \frac{n \cdot \pi}{30} \cdot R_F. \quad (5.21)$$

The momentum of the fan introduced into the system decreases and loses energy with increasing radius because the flow decelerates due to the friction of the air molecules. Therefore, the velocity through the bars is lower and the HTC decreases. Linear relations between the fan momentum and the momentum in front of the end winding bars have been established by means of the parametric study in chapter 4.

The first linear function in Figure 5.3a describes the relation between the two velocity ratios  $\Psi_1$  and  $\Psi_E$  defined below in (5.24). The ratio of the absolute fan velocity to the pole velocity is introduced above and the ratio of the velocity in front of the top bars  $c_E$  to the pole speed  $u_p$  is  $\Psi_E$ .

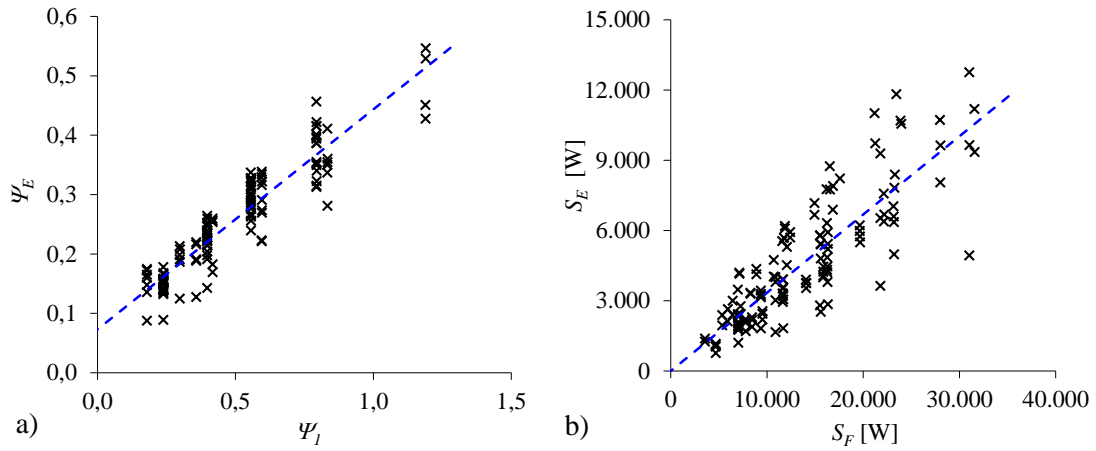


Figure 5.3: Linear functions for the momentum in front of the top bar.

Due to the high number of data resulting from the parametric study, a separate function is introduced for the axial and radial fan scheme in the form of

$$\Psi_E = C_{\Psi.E} \cdot \Psi_I + D_{\Psi.E} \quad (5.22)$$

where  $C_{\Psi.E}$  is the slope and  $D_{\Psi.E}$  is the displacement. A similar method is used for the calculation of the momentum in front of the top bar:

$$S_E = C_{S.E} \cdot S_F \quad (5.23)$$

where  $C_{S.E}$  is the slope of the function of Figure 5.3b. With (5.22) and (5.23) we can obtain the upstream (positive) mass flow rate in front of the top bars  $\dot{m}_{+,0}$ :

$$\dot{m}_{+,0} = \frac{S_E}{\Psi_E \cdot u_{F2}^2} \cdot \quad (5.24)$$

The total positive mass flow  $\dot{m}_+$  through the bars is higher if the ventilation scheme has a bypass opening  $\dot{m}_{By}$  and/or finger ducts  $\dot{m}_F$ . In this case, the mass flow rate is defined by the function

$$\dot{m}_+ = \max \left[ \dot{m}_{+,0} + (\dot{m}_{By} + \dot{m}_F) \cdot C_{By}, \dot{m}_{By} + \dot{m}_F \right] \quad (5.25)$$

where  $C_{By}$  is the slope of a linear function between  $\dot{m}_{+,0}$  and  $(\dot{m}_{By} + \dot{m}_F)$ . The upstream mass flow  $\dot{m}_+$  must stream down (reduced by  $\dot{m}_{By}$  and  $\dot{m}_F$ ) as a negative mass flow  $\dot{m}_-$ :

$$\dot{m}_- = \dot{m}_+ - (\dot{m}_{By} + \dot{m}_F). \quad (5.26)$$

The total mass flow streaming through the bars is finally obtained as

$$\dot{m}_L = \dot{m}_+ + \dot{m}_-. \quad (5.27)$$

Since the flow path of radial fan schemes can alternate under the top bar (see subsection 4.2) the calculation process of  $\dot{m}_L$  is carried out for both directions and an assumed mass flow is interpolated for the transition zone of (4.2).

## 6 Validation of the HTM

The heat transfer model of section 5 is an approximation tool. The coefficients and the adjustment parameters have been defined by means of CFD results of the parametric study and a validation of the HTM is required to show the accuracy, reliability and applicability of the model in the design process of large hydro generators. The verification has been done by simulations and by measurements to demonstrate the efficiency of the HTM.

### 6.1 Validation with CFD results

The following graphs in Figure 6.1 to Figure 6.5 show the Nusselt numbers calculated with the various HTMs in comparison to the CFD results of the parametric study.

The external and serial ventilation schemes confirm a very good accuracy of the HTM with a deviation of less than 10 %. Especially the HTM for serial ventilation yields excellent results over a wide range of different mass flow rates.

The HTM for the shaft mounted fans produces still acceptable results with a variance of  $\pm 30\%$ . The axial scheme VS-4 is more accurate than the one with a bypass opening (VS-5) because the estimation of the flow through the bars is more complex with an additional boundary condition. Nevertheless, the radial schemes with a bypass are more precise. Especially the HTM for the top bars in Figure 6.4a and Figure 6.5a agree very well since 10 different geometries are considered in this model. It can also be seen in Figure 6.3b, Figure 6.4b and Figure 6.5b that the bottom

bar results have a broader scattering and do not fit as well as the findings for the top bar.

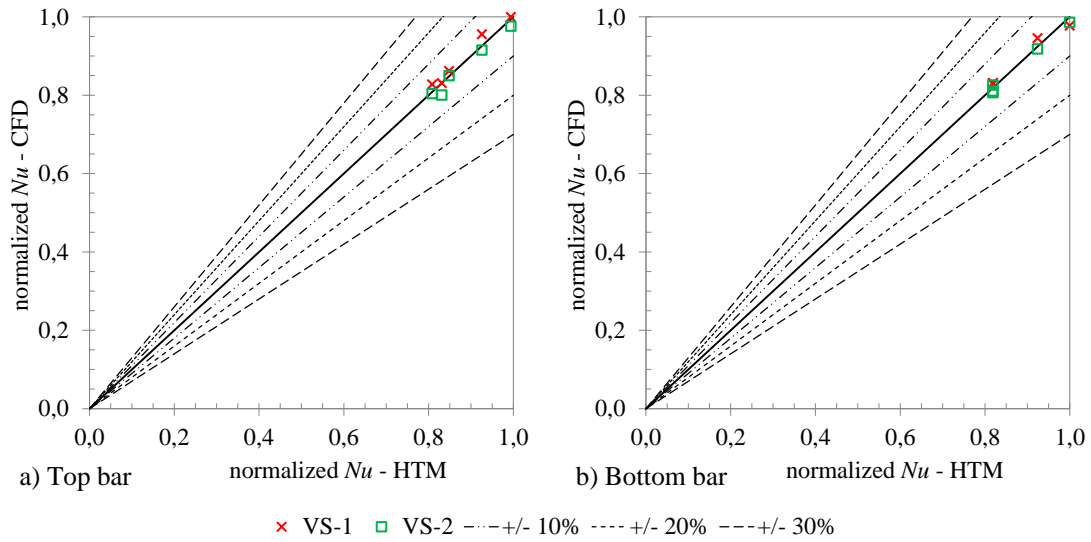


Figure 6.1: Normalized  $Nu$  of the HTM to the CFD results for external ventilation.

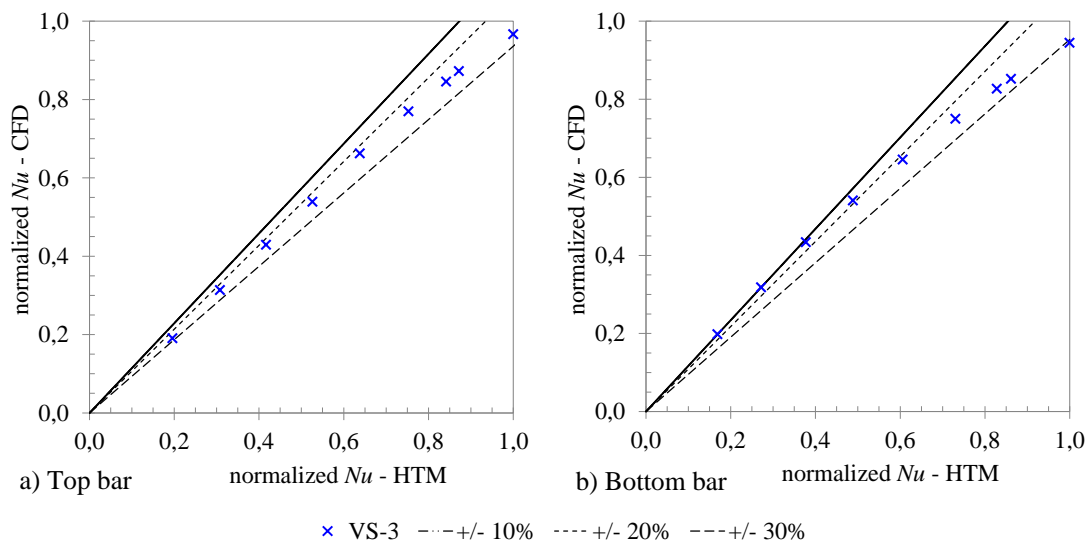


Figure 6.2: Normalized  $Nu$  of the HTM to the CFD results for serial ventilation.

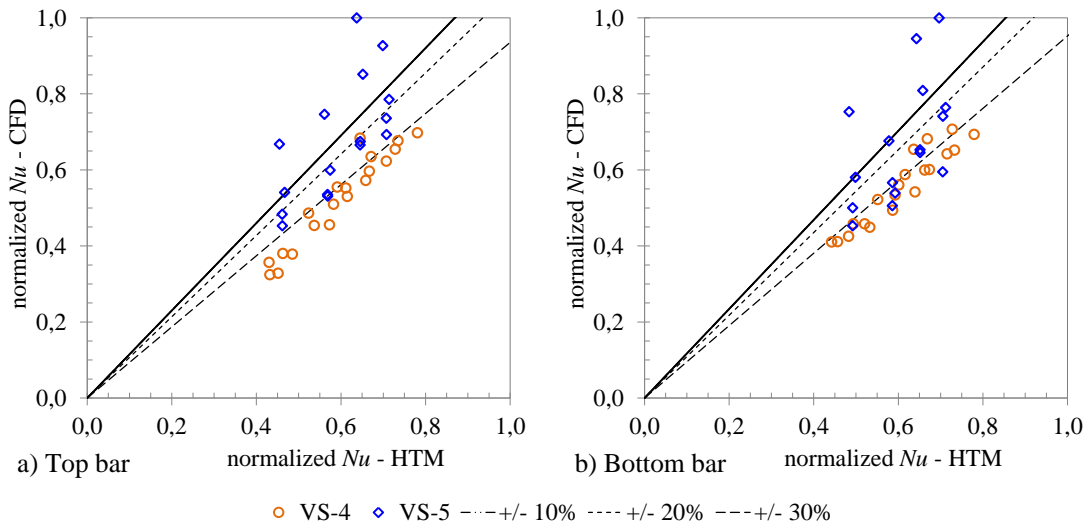


Figure 6.3: Normalized  $Nu$  of the HTM to the CFD results for axial fan ventilation.

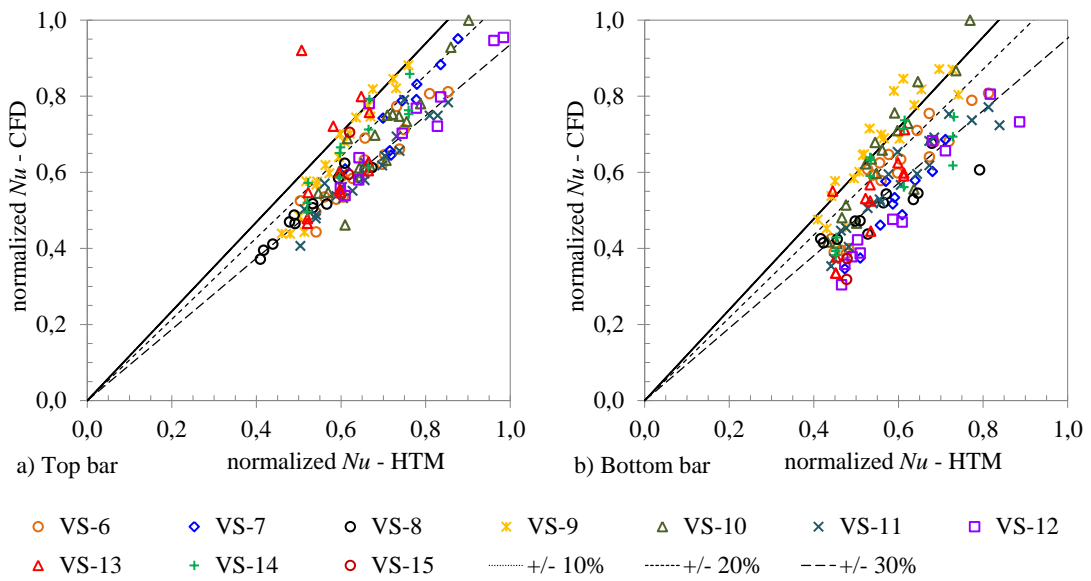


Figure 6.4: Normalized  $Nu$  of the HTM to the CFD results for radial fan ventilation; main flow through zone t1/b1.

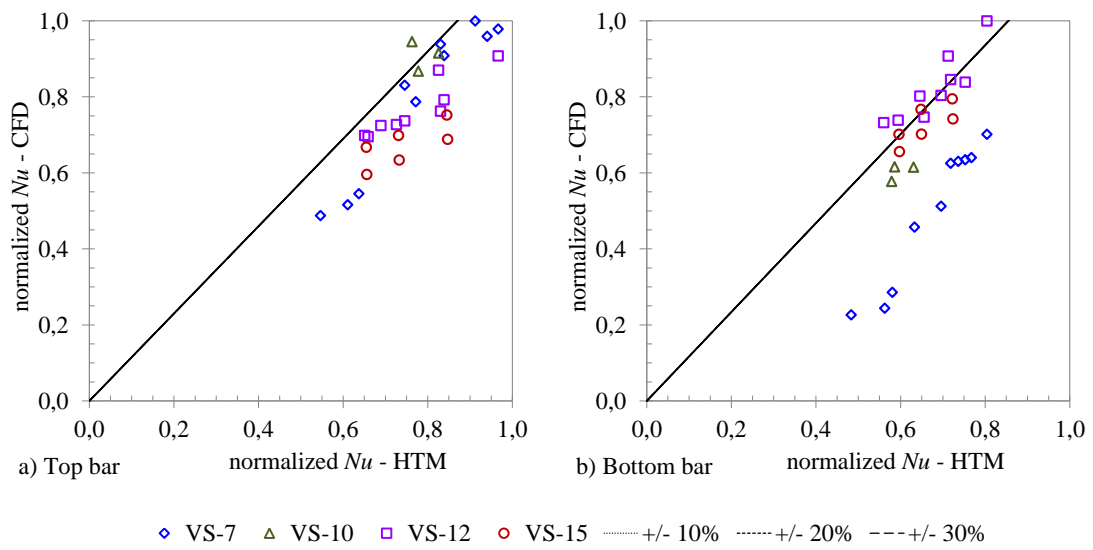


Figure 6.5: Normalized  $Nu$  of the HTM to the CFD results for radial fan ventilation; main flow through zone t3/b3 or besides the bars.

## 6.2 Validation with heat conduction calculations

We start the validation by examining a random inflow boundary condition for the cooling schemes VS-1, VS-4 and VS-6. In Figure 6.6, comparison of the temperatures obtained by a reference CHT computation with those stemming from three different HC simulations illustrates the accuracy of the HTM. The HC computations differ in the way the HTC has been derived. HC 1 uses the HTC of the CHT results of each wall element. HC 2 applies the averaged HTC of the CHT results for the various zones at the end winding bars and the use of the HTM for the appropriate scheme leads to the HTC for HC 3. The temperatures have been normalized to the constant wall temperature of the CFD parametric study to get comparable graphs.

Some aspects of the results are common for all three temperature curves obtained by an HC model in Figure 6.6. The temperature rises rapidly at the walls of the ring and space brackets connecting with the bar walls because these support parts insulate the bar. The temperature changes abruptly at the transition of t3 to b3 because of the different HTC values in these zones. HC 1 has nearly the same distribution as the CHT simulations since the HTC is transferred for each element. Furthermore, HC 2 follows the CHT curves also very well, although the HTC of the CHT results has been averaged.

The temperature distribution of the model HC 3 has a very good agreement with the results of the CHT simulation for VS-1 (Figure 6.6a). The temperature distribution along the bar is more homogeneous for this generator type since the inflow of the external cooling has no swirl. The curves in Figure 6.6b and 6.6c agree also very well considering that the HTM is a simplified approach compared to the CHT simulations. These graphs show also that the best cooled zones are t1 and b1 followed by t3 and b3. The gap between two bars is similar to a channel where the flow can directly stream through. Therefore, these sections result in lower wall temperatures. The geometry of the bars in the zones t2 and b2 is comparable with a wire frame whereby the direction of the flow is varying and the cooling of these zones is hence worse.

In summary, this validation shows a satisfactory agreement of the results obtained by the HTM with those resulting from heat conduction computations and the values of the calculated HTC are remarkably accurate for an approximate formulation. This validation of the HTM has been published in [112].

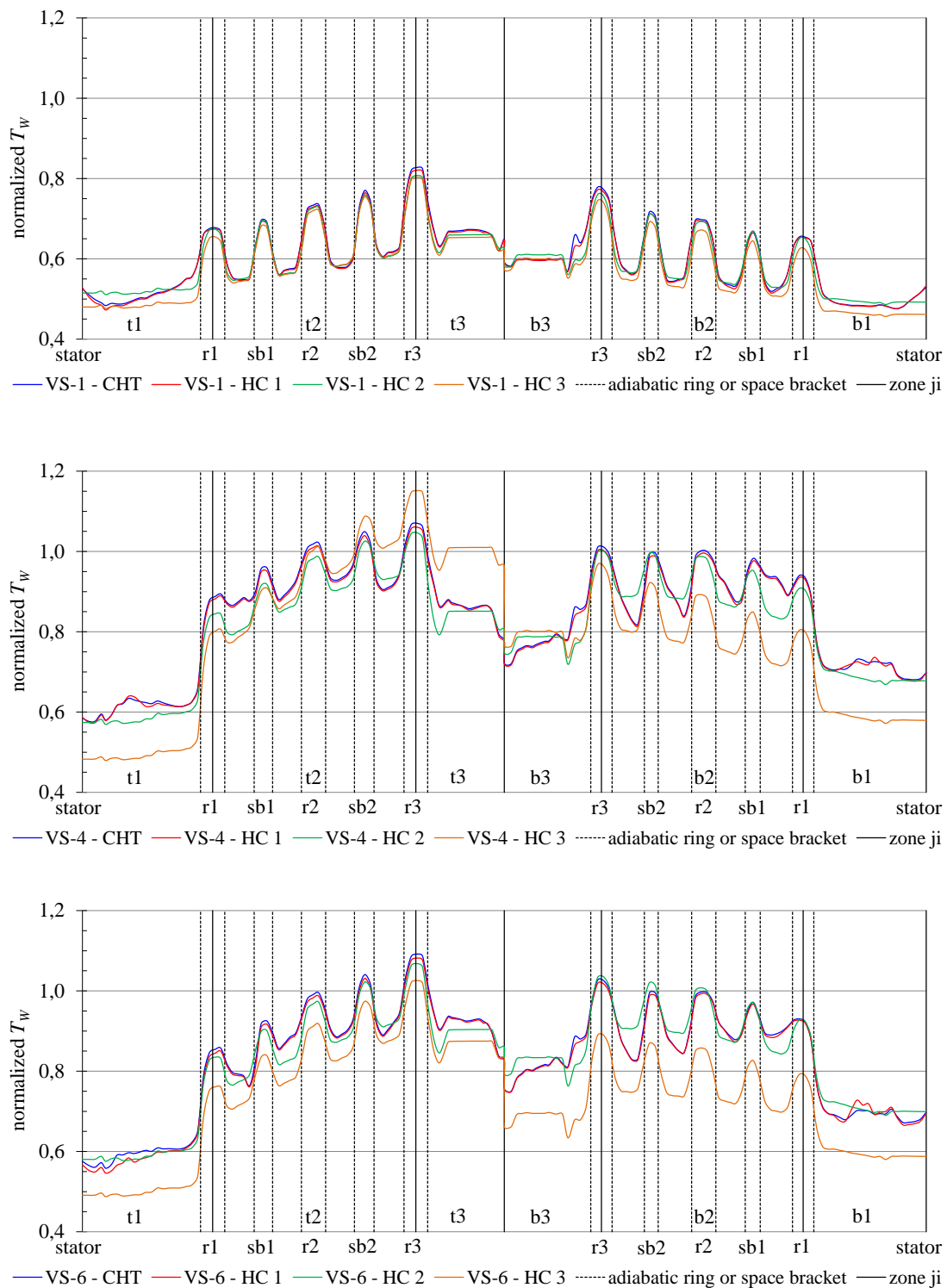


Figure 6.6: Comparison of the CHT and HC simulations.

### 6.3 Validation with measurements

The final validation step is the comparison of numerical results to temperature measurements at the end winding walls. The measurements have been obtained from tests of hydro generators in power plants which have been supplied by ANDRITZ HYDRO GmbH. To facilitate a validation for all measured cases, a simplified parametric bar model has been designed to calculate the temperature of each specific end winding geometry. The structure of the cooper and insulation is the same as shown in Figure 2.10 and the design with space brackets and support rings is similar to the curved bar in Figure 3.20. A simple hexahedral mesh is used for the composite and insulation parts. The heat loss in the copper is given as a heat source, the thermal conductivity is anisotropic and the boundary conditions are defined by the reference temperature and the HTC at the walls.

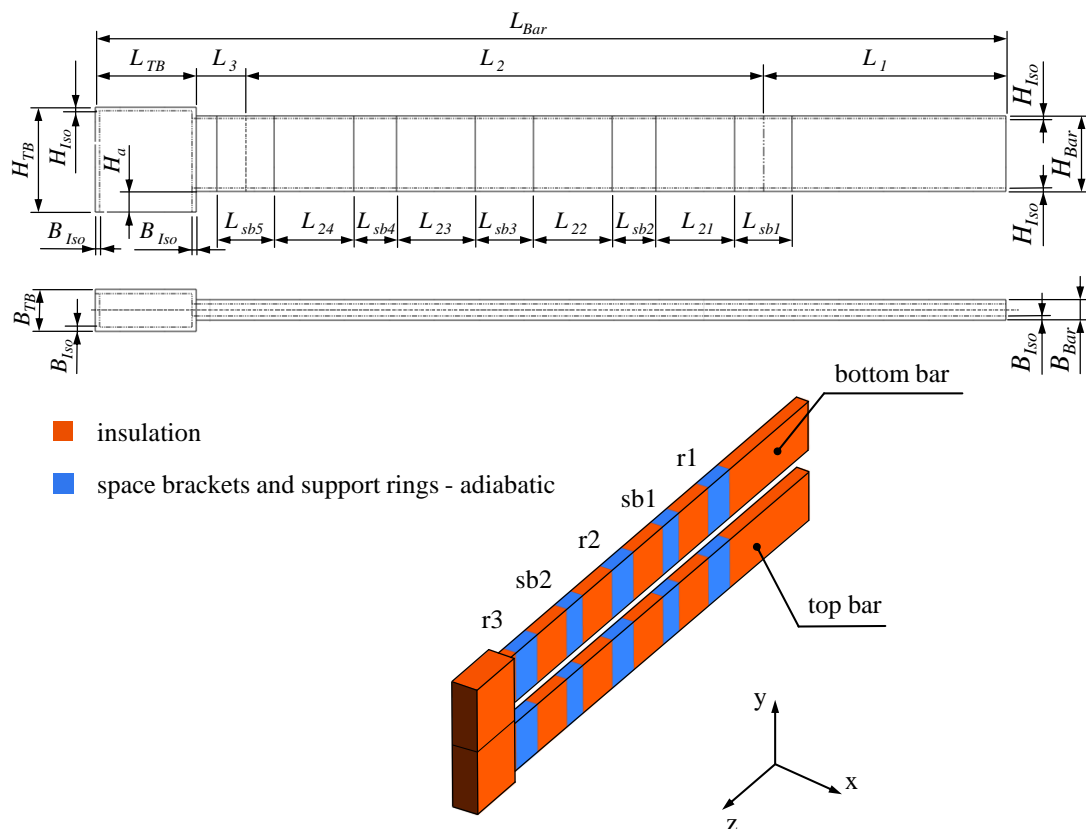


Figure 6.7: Parametric bar model with dimensions.

### 6.3.1 Accuracy of the parametric bar model

First of all, the parametric model has been validated by comparing to results of HC 3 in Figure 6.6. To this end, the boundary conditions, sources and material parameters of HC 3 for the schemes VS-1, VS-4 and VS-6 have been applied to the parametric model. The results from the curved geometry have been converted into the straight one to get comparable conditions. The parametric model shows a very good agreement in Figure 6.8 to the original bar (see Figure 3.20) with the differences negligible.

Further validations of the parametric bar model are presented in Figure 6.9 to Figure 6.11 where the wall temperature of the top and bottom bars is illustrated for the CHT and HC 3 simulations of subsection 6.2 as well as the temperature distribution of the parametric model using the boundary conditions of HC 3. Figure 6.9 shows very low temperatures and hence an excellent cooling of VS-1 in comparison to Figure 6.10 and Figure 6.11. Although, different CFD models, boundary conditions and sources have been used, the temperature plots of the bars are nearly identical in Figure 6.9a, 6.9b and 6.9c.

The highest local temperatures can be identified in Figure 6.10b and 6.10c in the zone t3, a fact pointed out in Figure 6.6b, too. The heat transfer coefficients have been calculated with the HTM and used as boundary conditions for these simulations. For this reason, the HTM overestimates the HTC in the zone t3. Nevertheless, the temperature plots are similar in the other zones in Figure 6.10a to 6.10c.

Finally, Figure 6.11a to 6.11c present the same results for VS-6. The temperature plots are similar but a lower temperature has been computed with the CHT model in Figure 6.11a. However, the temperature plots look identical for the HC simulations in Figure 6.11b and 6.11c which confirms the accuracy of the HTM as well as the reliability of the parametric bar model.

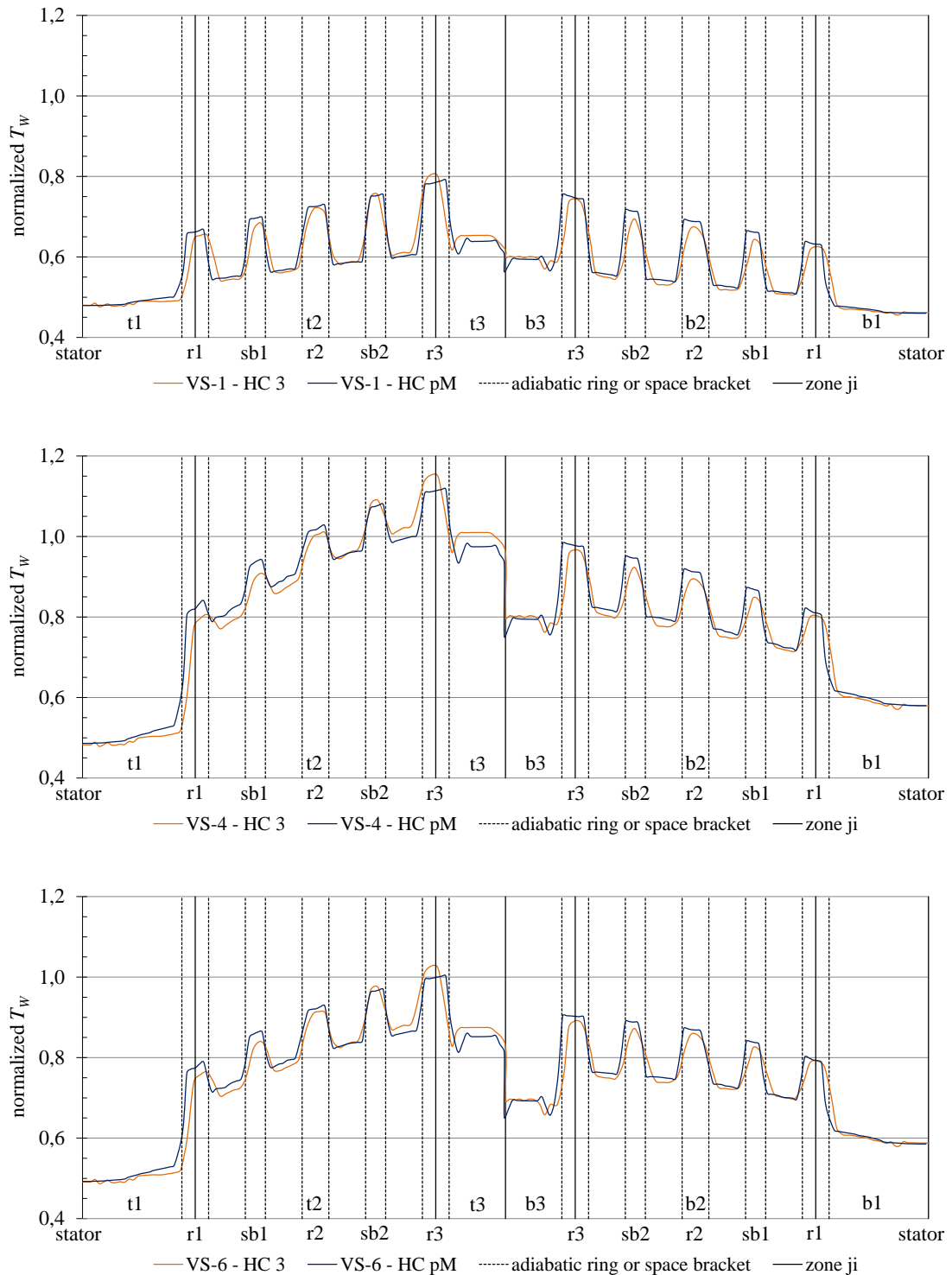


Figure 6.8: Comparison of the original curved bar to the parametric bar model..

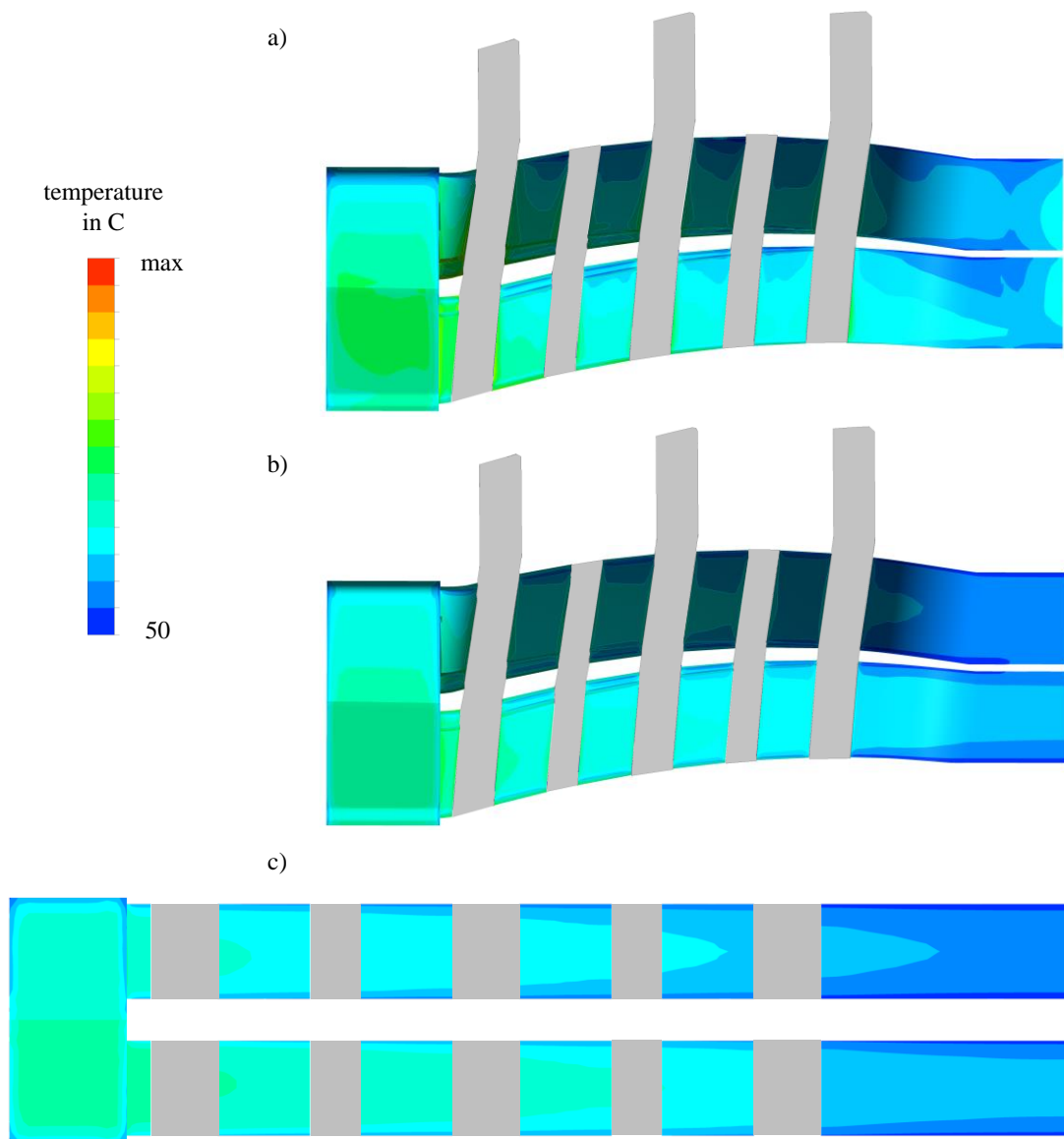


Figure 6.9: Temperature at the end winding bars of VS-1: a) CHT simulation, b) HC 3 simulation, c) parametric model.

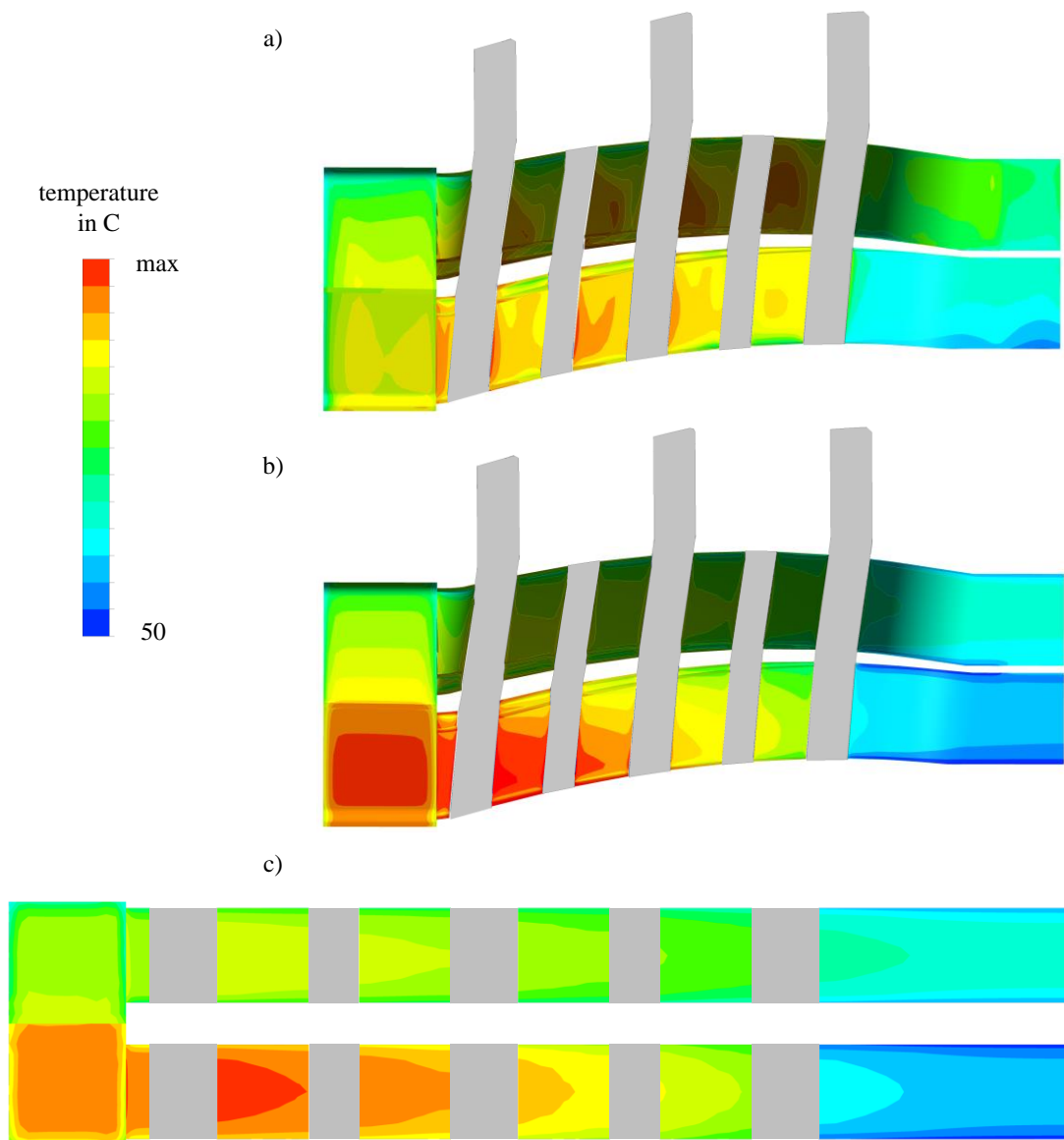


Figure 6.10: Temperature at the end winding bars of VS-4: a) CHT simulation, b) HC 3 simulation, c) parametric model.

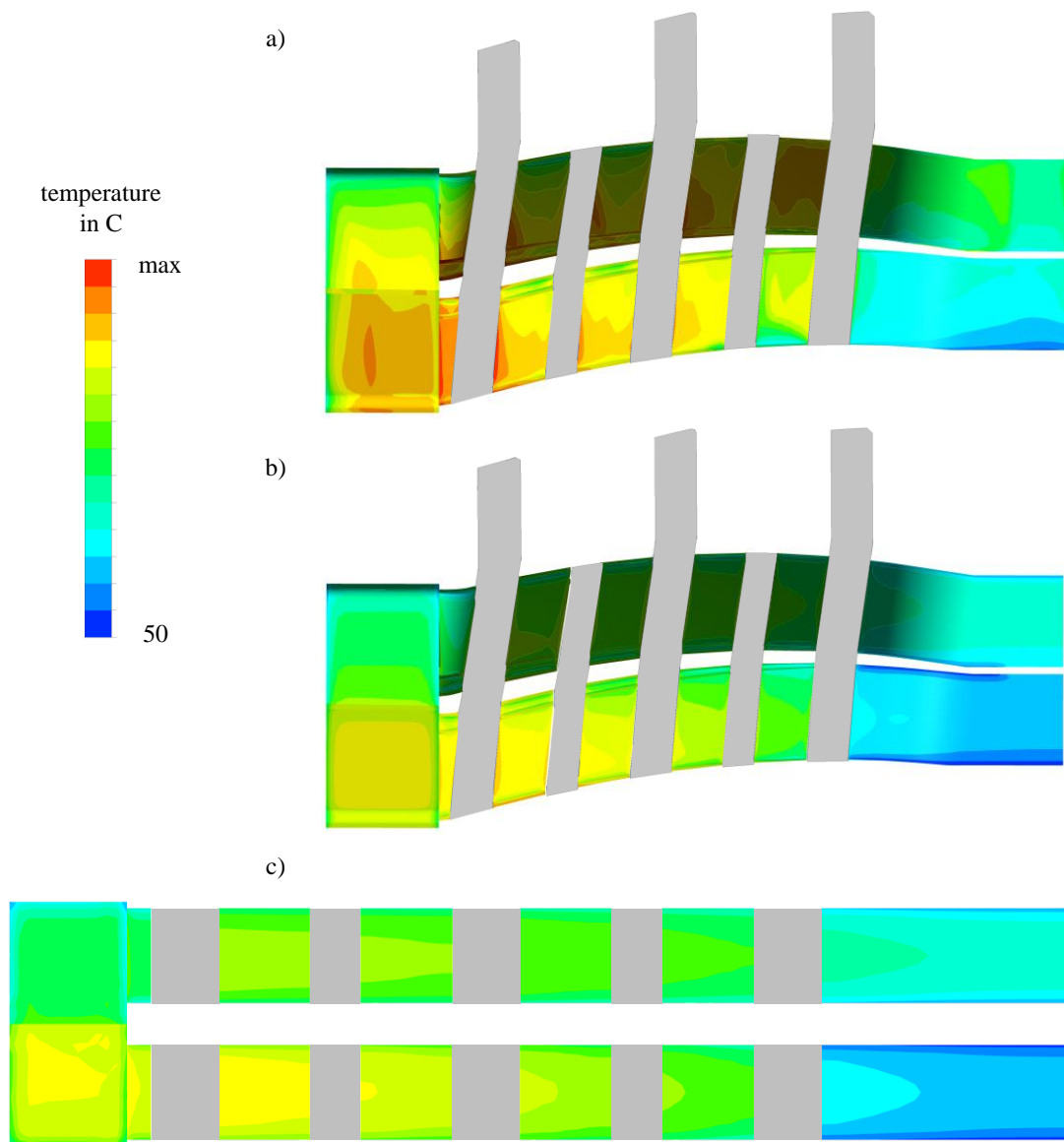


Figure 6.11: Temperature at the end winding bars of VS-6: a) CHT simulation, b) HC 3 simulation, c) parametric model.

### 6.3.2 Comparison with measurements

ANDRITZ HYDRO GmbH has supplied data of 5 different hydro generators to validate the HTM. The generators differ especially in the cooling scheme used which highly influences the heat transfer at the end winding bars:

- HG 1 – serial ventilation → equivalent to VS-3
- HG 2 – serial ventilation → equivalent to VS-3
- HG 3 – axial ventilation with bypass opening → equivalent to VS-5
- HG 4 – radial ventilation with bypass opening → equivalent to VS-13
- HG 5 – axial ventilation with bypass opening → equivalent to VS-5

Different measurement methods have been used for the various generators. The wall temperature of the bars has been measured by several temperature sensors on the surface along the bars for HG 1 and HG 2 (see Figure 6.12a). Furthermore, the temperatures at HG 2 have also been monitored by a thermo-graphic camera. These methods are not very accurate and can lead to large measurement errors. However, for HG 3, HG 4 and HG 5, only one value has been measured at the driving end (DE) and one at the non-driving end (NDE) of the generator. A small hole has been drilled into the bar between the zones t3 and b3 to add a temperature sensor and obtain the copper temperature (see Figure 6.12b).

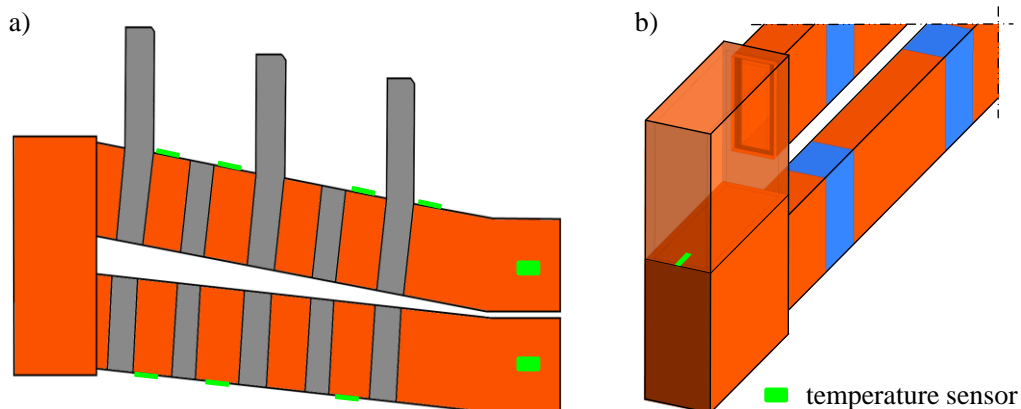


Figure 6.12: Location of the temperature sensors: a) HG 2, b) HG 3, HG 4 and HG 5.

The parametric bar model has been used for the heat conduction computations of the end winding bars. The heat loss in the bars, the reference temperature for the HTC and the thermal conductivity of the composite material have been obtained by

measurements and the HTM has been used to calculate the HTC in each bar zone for the various hydro generators.

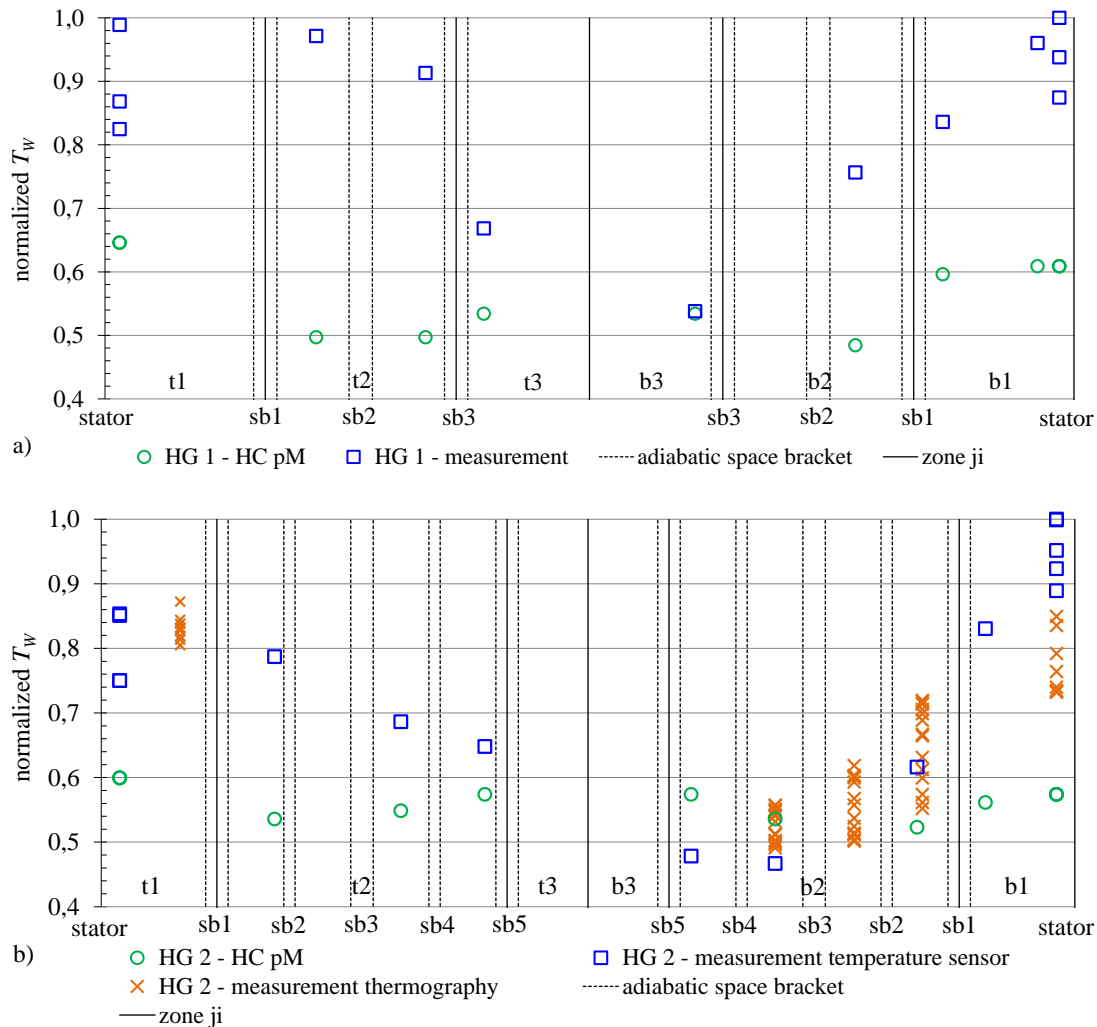


Figure 6.13: Comparison of measured and computed temperatures for HG1 and HG 2.

Figure 6.13a and 6.13b present the results for the machines HG 1 and HG 2. More temperature sensors have been added on the bars in the zones t1 and b1 in circumferential direction to pinpoint the differences between different bars. However, the computed temperatures of the HTM are just values averaged over the circumference for each zone. An important and obvious finding of this validation is that the calculated temperatures of the HTM are always lower than the measured temperatures of HG 1 and HG 2. A very good agreement has been attained in the zones t3 and b3, however, in the zones t2 and b2 of HG 1 the difference is very large.

Nevertheless, the HTM has turned out to be able to estimate appropriate and realistic temperatures for the end winding bars of HG 2, even in comparison with the detailed results of the thermo-graphic camera.

Since little empirical data are at disposal for the other three generators it is hardly possible to determine the accuracy of the HTM for the axial and radial shaft mounted schemes they represent. The deviation of the copper temperatures at the measured location between t3 and b3 shows an excellent agreement in Table 6.1. The calculated surface temperatures in these zones are acceptable in Figure 6.13a and 6.13b, too. Accordingly, it can be assumed that the HTM obtains plausible results along the bar in the other zones, too.

$\Delta T$ in C	HG 3	HG 4	HG 5
$\Delta T_{DE}$	4.0	11.2	7.7
$\Delta T_{NDE}$	14.3	2.1	21.7

Table 6.1: Temperature difference of HC computations to measurements.



## 7 Summary of new scientific results

The heat transfer model for the end winding bars of large hydro generators is a significant input quantity for lumped parameter thermal models. These models are used for the design of generators and calculate the temperature rise of the specific components. Generally, the convective heat transfer coefficients (HTC) are determined by measurements for small electrical machines or approximation equations are used for simple geometries as ducts or straight walls. Since temperature measurements of large generators are very rare, it makes sense to use computational fluid dynamics to obtain data of the fluid flow, cooling and heat transfer in such machines.

Many authors have investigated the heat transfer and cooling of small electrical machines by means of measurements, fluid dynamics or thermal networks as shown in the literature review in chapter 1. However, much fewer publications on this topic are available for large machines. Some authors have published measured or numerical results for the heat transfer at the pole surfaces and stator ducts or they present numerical methods for the analysis of these machines. Nevertheless, the influence of different ventilation schemes on the heat transfer of air-cooled hydro generators and especially the heat transfer at the end winding has not been investigated yet. Therefore, this work is dedicated to these less researched topics and finally, three major novel scientific results can be summarized:

- new reduced CFD model
- comprehensive parametric study of 15 ventilation schemes
- heat transfer model (HTM)

The first new scientific development is the simplification of the state-of-the-art simulation method in chapter 3. Since the standard pole sector model (PSM) has an enormous amount of elements leading to high computational costs, a new reduced model has been developed to decrease the simulation time of more than one week to about one day. The new model, called slot sector model (SSM), is a simplification of the PSM. Every component is reduced to its minimal required circumferential angle, wherefore the domains top bar, bottom bar, stator ducts and outlet area are simplified to the angle of one slot and the domains inlet and rotor have still a circumferential range of one pole. The multiple frames of reference – mixing plane application of ANSYS CFX connects the domains and periodic interfaces are used in circumferential direction. This SSM has been validated with respect to the component dimensions, mesh density, fluid properties and boundary conditions in section 3.5. The comparison of the SSM with steady-state and transient results of a PSM has shown an acceptable accuracy and a good reliability of the reduced model for the use in a parametric study. Still, it is important to keep in mind the assumptions, idealizations, and approximations made for the reduced model when the results of the parametric study are interpreted.

The realization of a parametric study with 15 ventilation schemes and different operational conditions constitutes the second important part of this work. Section 3.1 presents the different air-cooled hydro generators which can be ventilated by external or radial and axial shaft mounted fans. Furthermore, the location of the fans on the shaft, guiding plates of the inlet frame or bypass openings can be varied according to design and cooling requirements. The varied boundary conditions are the volume flow rate at the inlet, the rotational speed of the poles and the absolute velocity of the fan. The parametric study in chapter 4 is based on more than 230 CFD simulations with a wide range of numerical results.

On the one hand, this investigation with different operational cooling conditions has been used to compare the ventilation schemes and has shown their advantages and disadvantages. The end winding bars are split into 6 zones to carry out local results of the heat transfer and fluid flow. The cooling scheme VS-3 with a serial ventilation system has the most homogeneous heat transfer along the bar zones while the axial (VS-5) and radial (VS-14) shaft mounted fan cooling with a bypass opening have the highest local  $Nu$  value in zone t1. This zone is located at the top bar near the stator where the bars are forming a straight duct in radial direction and the flow has a low drag. Similar geometrical conditions are in the zones t3 and b3 at the end of the bars. An unusual phenomenon has been observed for the radial fan ventilation. Normally, one part of the flow streams up from the fan to the poles and another part

## 7 Summary of new scientific results

through the zones t1 and b1. However, the tendency of the flow to stream through t3 and b3 or beside the end of the bars (for schemes without guiding plates) is very high if the fan is located near the guiding plate and the absolute fan velocity is large. These conditions can lead to alternating flows with their directions difficult to predict.

Furthermore, the choice of the appropriate ventilation scheme is very difficult and depends on the properties of the entire project and customer requirements because most hydro generators are unique machines. Additionally, it has to be taken into account that the cooling air flow has also to dissipate the heat from the pole and stator duct surfaces.

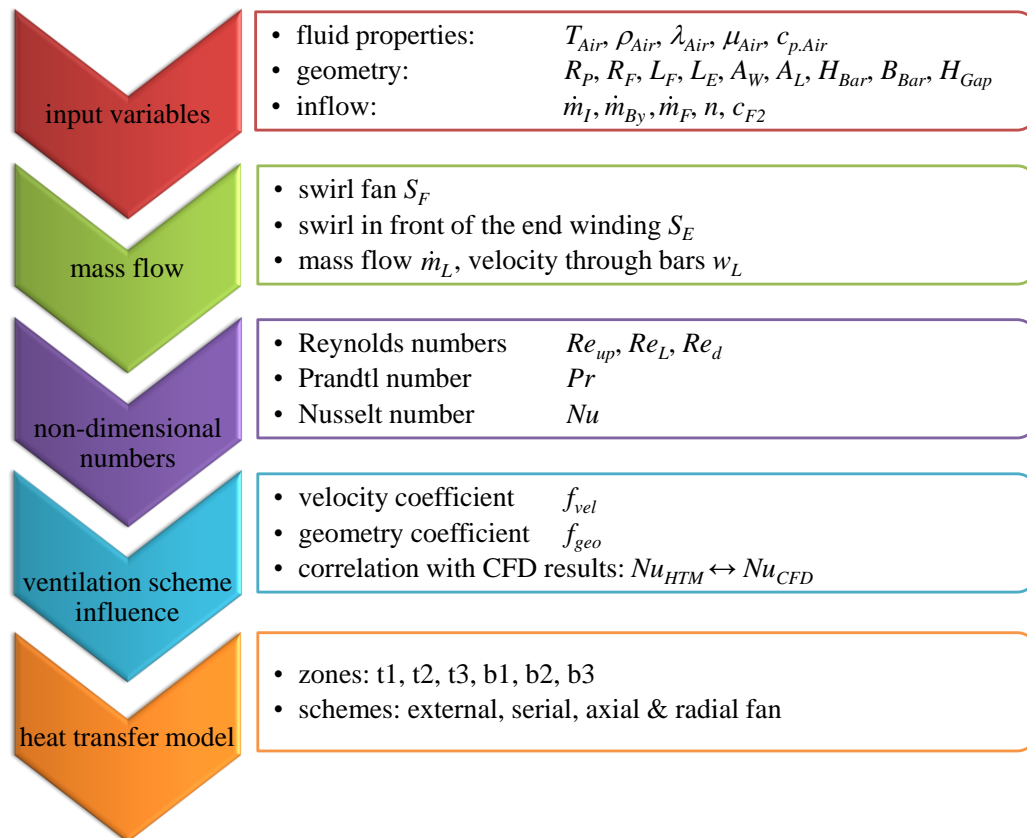


Figure 7.1: HTM procedure.

On the other hand, the enormous amount of data from the parametric study has been used for the definition and correlation of an approximation model of the convective heat transfer coefficient at the end winding bars in chapter 5. The heat transfer model is a network of approximation equations with fluid properties, bar and fan dimensions and flow parameters of the inlet as input variables, finally resulting in

the HTC for the 6 different zones at the end winding bars. A comprehensive overview of the HTM procedure is illustrated in Figure 7.1.

Furthermore, four HTMs have been defined for the different classifications of the ventilation schemes and, due to the possibly alternating flow of the radial fan scheme, two HTMs have been defined for these varying flow directions. The HTMs for the external and serial ventilation schemes have yielded excellent accuracy with a deviation of less than 10 % compared to CFD results. The HTM for the shaft mounted fans also show an acceptable agreement with a larger variance of  $\pm 30\%$ . The standard axial fan (VS-4) scheme is more accurate than the axial fan with a bypass opening (VS-5) since additional estimation of the mass flow through the bars is needed to define the boundary conditions. The HTM for the top bar of the radial fan schemes also results in a good accuracy of  $\pm 30\%$ , while the HTM for the bottom bar shows the largest inaccuracy among the various schemes.

Finally, the accuracy and applicability of the HTM for lumped parameter networks has been validated with heat conduction calculations and temperature measurements in chapter 6. The validation of the HTM by numerical simulations as well as measurements has proved to be successful. Especially the serial ventilation scheme could be validated by many measured temperatures. Unfortunately, less empirical data for the shaft mounted ventilation schemes are available, leading to an incomplete and less significant comparison.

To conclude, further investigations of modified ventilation schemes, e.g. changing the pole number and diameter, further variation of the fan location and guiding plates, different end winding geometry, are necessary to improve the HTM of the shaft mounted schemes. Furthermore, the validation and adjustment of the HTM with measurements is a continuing process increasing the accuracy of the whole approximation formulation.

## Bibliography

- [1] T. Stocker, D. Qin, G.-K. Plattner, M. Tignor, S. Allen, J. Boschung, A. Nauels, Y. Xia, V. Bex and P. Midgley (eds.), "Climate Change 2013: The Physical Science Basis. Contribution of Working Group I to the Fifth Assessment Report of the Intergovernmental Panel on Climate Change," Cambridge University Press, Cambridge, United Kingdom and New York, NY, USA, 2013.
- [2] W. Liebe, „Kühlung von Großmaschinen ETZ-A 87,“ No. 13, pp. 434-442, 1966.
- [3] G. Gotter, Erwaermung und Kühlung elektrischer Maschinen, Berlin/Göttingen/Heidelberg: Springer-Verlag, 1954.
- [4] J. Fourier, The Analytical Theory of Heat, Cambridge : Cambridge University Press, 1878.
- [5] VDI-Gesellschaft Verfahrenstechnik und Chemieingenieurwesen, VDI-Wärmeatlas, Berlin Heidelberg: Springer-Verlag, 2006.
- [6] W. Schuisky, Berechnung elektrischer Maschinen, Springer, 1960.
- [7] A. Binder, Elektrische Maschinen und Antriebe, Berlin Heidelberg: Springer , 2012.
- [8] S. Pal, Heat Transfer in Electrical Machines - A Critical Review, ERA Technology Ltd., 1971.
- [9] D. Gerling and G. Dajaku, "An improved lumped parameter thermal model for electrical machines," Institute for Electrical Drives, University of Federal Defence Munich, Neubiberg, Germany.

- 
- [10] A. Boglietti, A. Cavagnino and D. Staton, "Determination of Critical Parameters in Electrical Machine Thermal Models," *IEEE Transactions on Industry Applications*, vol. 44, no. 4, pp. 1150-1159, 2008.
- [11] A. Boglietti, A. Cavagnino, D. Staton, M. Shanel, M. Mueller and C. Mejuto, "Evolution and Modern Approaches for Thermal Analysis of Electrical Machines," *IEEE Transactions on Industrial Electronics*, vol. 56, no. 3, pp. 871 - 882, 2009.
- [12] A. Boglietti, A. Cavagnino, D. Staton, M. Popescu, C. Cossar and M. McGilp, "End Space Heat Transfer Coefficient Determination for Different Induction Motor Enclosure Types," *IEEE Transactions on Industry Applications*, vol. 45, no. 3, pp. 929-937, 2008.
- [13] A. Boglietti, A. Cavagnino, D. Staton und M. Popescu, „Experimental Assessment of End Region Cooling Arrangements in Induction Motor Endwindings,“ *IET Electric Power Applications*, Bd. 5, Nr. 2, pp. 203-209, 2011.
- [14] M. Hettegger, B. Streibl, O. Bíró and H. Neudorfer, "Measurements and Simulations of the Convective Heat Transfer Coefficients on the End-windings of an Electrical Machine," *IEEE Transactions on Industrial Electronics*, vol. 59, no. 5, pp. 2299 - 2308, 2012.
- [15] C. Mejuto, M. Mueller, M. Shanel, A. Mebarki and D. Staton, "Thermal modelling investigation of heat paths due to iron losses in synchronous machines," in *IET Conference on Power Electronics, Machines and Drives*, York, United Kingdom, 2008.
- [16] P. Mellor, D. Roberts and D. Turner, "Lumped Parameter Thermal Model for Electrical Machines of TEFC Design," *IEE Proceedings of Electric Power Applications*, vol. 138, no. 5, pp. 205-218, 1991.
- [17] C. Micallef, S. Pickering, K. Simmons and K. Bradley, "Improved Cooling in the End Region of a Strip-Wound Totally Enclosed Fan-Cooled Induction Electric Machine," *IEEE Transactions on Industrial Electronics*, vol. 55, no. 10, pp. 3517-3524, 2008.
- [18] M. Hettegger, "Cooling of the End-Windings in Electrical Traction Machines, PhD thesis," Graz University of Technology, Graz, Austria, 2012.
- [19] P. Moradnia, M. Golubev, V. Chernoray and H. Nilsson, "Flow of Cooling Air in an Electric Generator Model – An Experimental and Numerical Study," *Applied Energy*, vol. 114, pp. 644-653, 2014.

## Bibliography

---

- [20] R. Ujiie, R. Arlitt and H. Etoh, "Application of Computational Fluid Dynamics on Ventilation-Cooling Optimization of Electrical Machines," in *Colloquium on Large Electrical Machines CIGRE-EPFL*, Lausanne, Switzerland, 2005, September.
- [21] E. Farnleitner and G. Kastner, "Moderne Methoden der Ventilationsauslegung von Pumpspeichergeneratoren," *e&i*, vol. 127, pp. 24-29, 2010.
- [22] M. Shanel, S. Pickering and D. Lampard, "Application of Computational Fluid Dynamics to the Cooling of Salient Pole Electrical Machines," in *14th International Conference on Electrical Machines*, Espoo, Finland, 2000.
- [23] E. Schlemmer, J. Schoenauer, E. Farnleitner and F. Mueller, "Transient Electromagnetic and Coolant Flow Investigations of Synchronous Generators Using Numerical Approaches," in *16th International Conference on Electrical Machines*, Cracow, Poland, 2004.
- [24] K. Toussaint, F. Torriano, J. Morissette, C. Hudon and M. Reggio, "CFD Analysis of Ventilation Flow for a Scale Model Hydro-Generator," in *ASME 2011 Power Conference*, Denver, Colorado, USA, 2011, July.
- [25] R. Dépraz, R. Zickermann, A. Schwery and F. Avellan, "CFD Validation and Air Cooling Design Methodology for Large Hydro Generator," in *17th International Conference on Electrical Machines*, Chania, Crete Island, Greece, 2006.
- [26] B. Vogt and S. Lahres, "Calculation of Cooling and Ventilation of Large Hydro Generators with Advanced 3D Numerical Methods," in *International Conference on Hydropower and Dams*, Innsbruck, Austria, 2013.
- [27] E. Farnleitner, "Computational Fluid Dynamics Analysis for Rotating Electrical Machinery, PhD thesis," University of Leoben, Leoben, Austria, 1999.
- [28] W. Tong, "Numerical Analysis of Flow Field in Generator End-Winding Region," *International Journal of Rotating Machinery*, pp. 1-10, 2008.
- [29] S. Houde, C. Hudon and P. Vicent, "Simulation Strategies of the Cooling Flow for Large Hydro Generators," *Hydropower & Dams*, vol. 15, no. 6, pp. 93-99, 2008.
- [30] M. Fénot, E. Dorignac, A. Giret and G. Lalizel, "Convective heat transfer in the entry region of an annular channel with slotted rotating inner cylinder," *Applied Thermal Engineering*, pp. 345-358, 2014.

- 
- [31] N. Lancial, F. Torriano, F. Beaubert, S. Harmand and G. Rolland, "Study of a Taylor-Couette-Poiseuille Flow in an Annular Channel with a Slotted Rotor," in *21th International Conference on Electrical Machines*, Berlin, Germany, 2014.
- [32] F. Torriano, N. Lancial, M. Lévesque, G. Rolland, C. Hudon, F. Beaubert, J.-F. Morissette and S. Harmand, "Heat transfer coefficient distribution on the pole face of a hydrogenerator scale model," *Applied Thermal Engineering*, pp. 153-162, 2014.
- [33] E. Spring, *Elektrische Maschinen*, Heidelberg: Springer-Verlag, 2006.
- [34] A. Binder, "Großgeneratoren und Hochleistungsantriebe," Institut für Elektrische Energiewandlung, Darmstadt, 2013.
- [35] "IEEE Std C50.12 - Standard for Salient-Pole 50 Hz and 60 Hz Synchronous Generators and Generator/Motors for Hydraulic Turbine Applications Rated 5 MVA and Above," Institute of Electrical and Electronics Engineers, New York, 2006.
- [36] L. Böswirth, *Technische Strömungslehre*, 7 Hrsg., Wiesbaden: Vieweg & Sohn Verlag, 2007.
- [37] J. Spurk and N. Aksel, *Fluid Mechanics*, 2 ed., Berlin Heidelberg: Springer-Verlag, 2008.
- [38] F. White, *Fluid Mechanics*, 4 ed., United States: WCB/McGraw-Hill.
- [39] H. Oertel, *Prandtl's Essentials of Fluid Mechanics*, 2 ed., New York, USA: Springer-Verlag, 2004.
- [40] H. Schlichting und K. Gersten, *Grenzschichttheorie*, 10 Hrsg., Berlin Heidelberg: Springer-Verlag, 2006.
- [41] G. Brenn und W. Meile, „Vorlesungsskriptum Strömungslehre und Wärmeübertragung,“ Institut für Strömungslehre und Wärmeübertragung, Graz, 2006.
- [42] D. Wilcox, *Turbulence Modeling for CFD*, La Cañada, California: DCW Industries, Inc., 1994.
- [43] L. Prandtl, "Über Flüssigkeitsbewegung bei sehr kleiner Reibung," in *Verhandlungen des III. Internationalen Mathematiker Kongresses*, Heidelberg, 1904.
- [44] H. Blasius, „Grenzschichten in Flüssigkeiten mit kleiner Reibung,“ *Zeitschrift für Mathematik und Physik*, Bd. 56, Nr. 1, 1908.

## Bibliography

---

- [45] L. Prandtl, "Über die ausgebildete Turbulenz," *ZAMM*, vol. 5, pp. 136-139, 1925.
- [46] "ANSYS CFX Documentation," ANSYS, Inc., Canonsburg, USA, Release 14.5, 2012.
- [47] J. Schönauer, "FEM Modellrechnung mit ANSYS zur Nachbildung der Temperaturverteilung des Statorerwärmungsmodells," Nr. TB E 074/001, Andritz Hydro, Weiz, 1999.
- [48] F. Incropera, D. Dewitt, T. Bergman and A. Lavine, *Fundamentals of Heat and Mass Transfer*, 6 ed., Hoboken, NJ: John Wiley & Sons, 2007.
- [49] F. Kreith, R. M. Manglik and M. S. Bohn, *Principles of Heat Transfer*, 7 ed., Stamford, USA: Cengage Learning, 2011.
- [50] D. Staton, A. Boglietti and A. Cavagnino, "Solving the More Difficult Aspects of Electric Motor Thermal Analysis in Small and Medium Size Industrial Induction Motors," *IEEE Transactions on Energy Conversion*, vol. 20, no. 3, pp. 620-628, 2005.
- [51] E. Schubert, "Heat Transfer Coefficients at End Winding and Bearing Covers of Enclosed Asynchronous Machines," *Elektrie*, vol. 22, 1966.
- [52] M. Hettegger, A. Reinbacher-Köstinger and O. Bíró, "Characterizing the Convective Wall Heat Transfer on Convolute Shapes in the End-region of an Induction Machine," in *16th International Conference on Electrical Machines*, Marseille, France, 2012.
- [53] C. Fletcher, *Computational Techniques for Fluid Dynamics 1 - Fundamental and General Techniques*, 2 ed., Berlin Heidelberg: Springer-Verlag, 1991.
- [54] J. Anderson, *Computational Fluid Dynamics - The basics with applications*, USA: McGraw Hill, 1995.
- [55] C. Fletcher, *Computational Techniques for Fluid Dynamics 2 - Specific Techniques for Different Flow Categories*, Berlin Heidelberg: Springer-Verlag, 1991.
- [56] C. Hirsch, *Numerical Computation of Internal and external Flows Volume 1: Fundamentals of Numerical Discretization*, Chichester: John Wiley & Sons, 1988.
- [57] E. Laurien und H. Oertel, *Numerische Strömungsmechanik*, Wiesbaden: Vieweg+Teubner, 2009.

- 
- [58] J. Tannehill, D. Anderson and R. Pletcher, *Computational Fluid Mechanics and Heat Transfer*, 2 ed., Washington, DC, USA: Taylor & Frances, 1997.
- [59] S. Lecheler, *Numerische Strömungsberechnung*, Wiesbaden: Vieweg+Teubner Verlag, 2011.
- [60] P. Lax and B. Wendroff, "Systems of Conservation Laws," *Comm. Pure and Applied Mathematics*, vol. 13, pp. 217-237, 1960.
- [61] A. Jameson, W. Schmidt and E. Turkel, "Numerical simulation of the Euler equations by finite volume method using Runge-Kutta time stepping schemes," *AIAA Paper 1981-1259*, 1981.
- [62] R. Beam and R. Warming, "An implicit finite-difference algorithm for hyperbolic system in conservation law form," *Journal of Computational Physics*, vol. 22, pp. 87-109, 1976.
- [63] R. Courant, E. Isaacson and M. Reeves, "On the solution of nonlinear hyperbolic differential equations by finite differences," *Comm. Pure and Applied Mathematics*, vol. 5, pp. 243-255, 1952.
- [64] S. Godunov, "A difference scheme for numerical computation of discontinuous solution of hydrodynamic equations," *Math. Sbornik*, vol. 47, pp. 271-306, 1959.
- [65] B. Van Leer, "Towards the ultimate conservative difference scheme. A second order sequel to Godunov's method," *Journal of Computational Physics*, vol. 32, pp. 101-136, 1979.
- [66] P. Roe, "Some contributions to the modelling of discontinuous flows," *Lecture in Applied Mathematics*, vol. 22, pp. 357-372, 1985.
- [67] A. Kolmogorov, "Local Structure of Turbulence in Incompressible Viscous Fluid for Very Large Reynolds Number," *Dokl. Akad. Wiss. USSR*, vol. 30, pp. 299-303, 1941.
- [68] J. Smagorinsky, "General Circulation Experiments with the Primitive Equations," *Monthly Weather Review*, vol. 91, no. 3, pp. 99-164, 1963.
- [69] F. Menter and Y. Egorov, "Turbulence Models based on the Length-scale Equation," in *4th International Symposium on Turbulent Shear Flow Phenomena*, Williamsburg, USA, 2005.
- [70] J. Deardorff, "A numerical study of three-dimensional turbulent channel flow at large Reynolds numbers," *Journal of Fluid Mechanics*, vol. 41, no. 2, p. 453-480, 1970.

## Bibliography

---

- [71] D. Chapman, "Computational aerodynamics development and outlook," *AIAA Journal*, vol. 17, no. 12, pp. 1293-1313, 1979.
- [72] J. Boussinesq, «Theorie de l'Écoulement Tourbillant,» *Mem. Presentes par Divers Savants Acad. Sci. Inst. Fr.*, vol. 23, pp. 46-50, 1877.
- [73] S. Pope, *Turbulent Flows*, Cambridge, United Kingdom: Cambridge University Press, 2000.
- [74] B. Baldwin and H. Lomax, "Thin Layer Approximation and Algebraic Model for Separated Turbulent Flows," in *AIAA 16th Aerospace Science Meeting*, Huntsville, Alabama, 1978.
- [75] P. Spalart and S. Allmaras, "A One-Equation Turbulence Model for Aerodynamic Flows," in *Recherche Aerospatiale, No. 1*, 1994.
- [76] B. Launder and . B. Sharma, "Application of the Energy-Dissipation Model of Turbulence to the Calculation of Flow near a Spinning Disc," *Letters in Heat and Mass Transfer*, vol. 1, no. 2, pp. 131-137, 1974.
- [77] T. Shih, W. Liou, A. Shabbir, Z. Yang and J. Zhu, "A New k- $\epsilon$  Eddy Viscosity Model for High Reynolds Number Turbulent Flows - Model Development and Validation," *Computers Fluids*, vol. 24, no. 3, pp. 227-238, 1995.
- [78] V. Yakhot, S. Orszag, S. Thangam, T. Gatski and C. Speziale, "Development of turbulence models for shear flows by a double expansion technique," *A Physics of Fluids*, vol. 4, no. 7, pp. 1510-1520, 1992.
- [79] D. Wilcox, "Formulation of the k- $\omega$  Turbulence Model Revisited," *AIAA Journal*, vol. 46, no. 11, pp. 2823-2838, 2008.
- [80] F. Menter, "Two-Equation Eddy-Viscosity Turbulence Models for Engineering Applications," *AIAA Journal*, vol. 32, no. 8, pp. 1598-1605, 1994.
- [81] P. Durbin, "Separated flow computations with the k -  $\epsilon$  -  $\nu_2$  model," vol. 33, pp. 659-667, *AIAA Journal*.
- [82] B. Launder, G. Reece and W. Rodi, "Progress in the Development of a Reynolds-Stress Turbulent Closure," *Journal of Fluid Mechanics*, vol. 68, no. 3, pp. 537-566, 1975.
- [83] F. Menter, M. Kuntz and R. Langtry, "Ten years of industrial experience of the SST turbulence model," in *4th Symposium on Turbulence, Heat and Mass Transfer*, Antalya, Turkey, 2003.

- 
- [84] B. Launder and D. Spalding, "The Numerical Computation of Turbulent Flows," *Computer Methods in Applied Mechanics and Engineering*, vol. 3, pp. 269-289, 1974.
- [85] H. Grotjans and F. Menter, "Wall Functions for General Application CFD Codes," in *4th European Computational Fluid Dynamics Conference*, Athens, Greece, 1998.
- [86] W. Vieser, T. Esch and F. Menter, "Heat Transfer Predictions using Advanced two-equation Turbulence Models," *CFX Technical Memorandum*, vol. CFX-VAL10/0602, 2002.
- [87] F. Menter and T. Esch, "Elements of Industrial Heat Transfer Predictions," in *16th Brazilian Congress of Mechanical Engineering*, Uberlandia, Brazil, 2001.
- [88] B. Kader, "Temperature and Concentration Profiles in Fully Turbulent Boundary Layers," *International Journal of Heat Mass and Transfer*, vol. 24, no. 9, pp. 1541-1544, 1981.
- [89] J. Adamczyk, "Model equation for simulating flows in multistage turbomachinery," NASA Lewis Research Center, Cleveland, USA, 1984.
- [90] G. Adkins and L. Smith, "Spanwise Mixing in Axial-Flow Turbomachines," *Journal of Engineering for Power*, vol. 104, no. 1, pp. 97-110, 1982.
- [91] M. Mansour, J. Gunaraj and S. Goswami, "Validation of Steady Average-Passage and Mixing Plane CFD Approaches for the Performance Prediction of a Modern Gas Turbine Multistage Axial Compressor," in *ASME Turbo Expo*, Berlin, Germany, 2008.
- [92] N. Cumpsty, *Compressor Aerodynamics*, Harlow, England: Longman Scientific & Technical, 1989.
- [93] C. Wu, "A General Theory of Three Dimensional Flow in a Subsonic or Supersonic Torbumachines of Axial, Radial and Mixed Flow Type," NACA TN 2604, Washington, USA, 1952.
- [94] L. Smith, "The Radial-Equilibrium Equation of Turbomachinery," *Journal of Engineering for Power*, vol. 88, pp. 1-12, 1966.
- [95] J. Denton and U. Singh, "Time Marching Methods for Turbomachinery Flow Calculations," *VKI Lecture Series 1979-7*, 1979.
- [96] "ANSYS FLUENT Theory Guide," ANSYS, Inc., Canonsburg, USA, Release 14.5, 2012.

## Bibliography

---

- [97] T. Carolus, Ventilatoren: Aerodynamischer Entwurf, Schallvorhersage, Konstruktion, Wiesbaden: Springer Vieweg, 2013.
- [98] B. Eck, Ventilatoren, Berlin, Heidelberg, New York: Springer-Verlag, 2002.
- [99] T. Belamri, P. Galpin, A. Braune and C. Cornelius, "CFD Analysis of a 15 Stage Axial Compressor Part I: Methods," in *ASME Turbo Expo*, Reno-Tahoe, USA, 2005, June.
- [100] T. Belamri, P. Galpin, A. Braune and C. Cornelius, "CFD Analysis of a 15 Stage Axial Compressor Part II: Results," in *ASME Turbo Expo*, Reno-Tahoe, USA, 2005, June.
- [101] P. Galpin, R. Broberg and B. Hutchinson, "Three-dimensional Navier-Stokes Predictions of Steady State Rotor-Stator Interaction with Pitch Change," in *Proceedings of the 3rd Annual Conference of the CFD Society of Canada*, Banff, Albert, Canada, 1995, June.
- [102] "ANSYS ICEM CFD Help Manual," ANSYS, Inc., Canonsburg, USA, Release 14.5, 2012.
- [103] W. Sutherland, "The viscosity of gases and molecular force," *Philosophical Magazine*, vol. 5, pp. 507-531, 1893.
- [104] S. Gordon and B. McBride, "Computer Program for Calculation of Complex Chemical Equilibrium Compositions, Rocket Performance, Incident and Reflected Shocks and Chapman-Jouguet Detonations," NASA Report SP-273, NASA Lewis Research Center, 1971.
- [105] S. Klomberg, E. Farnleitner, G. Kastner and O. Bíró, "Implementation of a New Simulation Strategy for a Cooling Study of Large Hydro Generators," in *7th IET Int. Conf. on Power Electronics, Machines and Drives*, Manchester, United Kingdom, 2014.
- [106] S. Klomberg, E. Farnleitner, G. Kastner and O. Bíró, "Characteristics of the Convective Heat Transfer Coefficient at the End Winding of a Hydro Generator," *Journal of Thermal Science and Engineering Applications*, vol. 7, no. 1, pp. 1-8, 2014.
- [107] S. Klomberg, E. Farnleitner, G. Kastner and O. Bíró, "Comparison of CFD Analyzing Strategies for Hydro Generators," in *21th International Conference on Electrical Machines*, Berlin, 2014.

- [108] S. Klomberg, E. Farnleitner, G. Kastner and O. Bíró, "Numerical Study of the Cooling Air Flow in a Hydro Generator with various Ventilation Systems," in *6th European Conference on Computational Fluid Dynamics*, Barcelona, Spain, 2014.
- [109] G. Traxler-Samek, R. Zickermann and A. Schwery, "Cooling Airflow, Losses, and Temperatures in Large Air-Cooled Synchronous Machines," *IEEE Transactions on Industrial Electronics*, vol. 57, no. 1, pp. 172-180, 2010.
- [110] C. Czado and T. Schmidt, *Mathematische Statistik*, Heidelberg Dordrecht London New York: Springer , 2011.
- [111] E. Farnleitner, "Verbesserte Näherungsformel zur Berechnung eines mittleren Wärmeübergangskoeffizienten für Statorwickelköpfe," Nr. TB E 118/11, Andritz Hydro, Weiz, 2011.
- [112] S. Klomberg, E. Farnleitner, G. Kastner and O. Bíró, "Validation of a Heat Transfer Model for End Winding Bars of Large Hydro Generators," in *15th International IGTE Symposium on Numerical Field Calculation*, Graz, Austria, 2014.
- [113] A. Kolmogorov, "Equations of Turbulent Motion of an Incompressible Fluid," *Izvestia Academy of Sciences*, vol. 6, no. 1 and 2, pp. 56-58, 1942.

# Appendix

## A Fluid properties

$T$ in K	$T$ in °C	$\rho$ in kg/m <sup>3</sup>	$c_p$ in J/kgK	$\lambda$ in 10 <sup>-2</sup> W/mK	$\mu$ in 10 <sup>-6</sup> Ns/m <sup>2</sup>
273	0	1.2758	1005.9	2.4360	17.218
293	20	1.1885	1006.4	2.5873	18.205
313	40	1.1124	1007.1	2.7354	19.165
333	60	1.0455	1008.2	2.8040	20.099
353	80	0.9862	1009.7	3.0225	21.009
373	100	0.9333	1011.5	3.1620	21.896
393	120	0.8858	1013.6	3.2989	22.763
413	140	0.8428	1016.0	3.4336	23.610
433	160	0.8039	1018.8	3.5660	24.439
453	180	0.7684	1021.8	3.6964	25.251
473	200	0.7359	1025.2	3.8248	26.046
523	250	0.6655	1034.7	4.1382	27.970
573	300	0.6075	1045.4	4.4417	29.811
623	350	0.5587	1056.8	4.7367	31.579
673	400	0.5172	1068.8	5.0240	33.284

Table A.1: Measured thermodynamic properties of dry air [5].

## B Radiation of heat

Every surface with a higher temperature than the absolute zero limit of the thermodynamic scale emits energy in form of electromagnetic waves. The wavelength range is approximately between 0.1 and 100  $\mu\text{m}$  and can be subdivided in ultraviolet, visible and infrared light. When radiation is incident on a surface, a part will be absorbed in the material, another part will be reflected on the surface or transmitted through the body. The absorption coefficient  $\alpha_\lambda$ , the reflection coefficient  $\rho_\lambda$  and the transmission coefficient  $\tau_\lambda$  describe the distribution of the incident radiation:

$$\alpha_\lambda + \rho_\lambda + \tau_\lambda = 1. \quad (\text{B.1})$$

Another important radiation property is the behaviour of the reflection. Industrially plated, machined or painted surfaces have a diffuse reflection, i.e. an isotropic radiation from every point on the surface. This is in contrast to the specular reflection of a mirror [49]. An arbitrary surface with monochromatic properties emits only one single wavelength. This property is defined by the monochromatic emission coefficient

$$\varepsilon_\lambda = \frac{E_\lambda(T)}{E_{b\lambda}(T)}. \quad (\text{B.2})$$

$E_\lambda$  is the emissive power of a real body and  $E_{b\lambda}$  the emissive power of a black body, i.e. of a surface with the maximum emissive energy and therefore an ideal radiator. Planck's law describes the emission of electromagnetic waves by a black body as

$$E_{b\lambda} = \frac{C_1}{\lambda_w^2 \cdot \left[ e^{\left( \frac{C_2}{\lambda_w T} \right)} - 1 \right]} \quad (\text{B.3})$$

where  $\lambda_w$  is the wavelength and  $T$  the temperature of the surface. The constants have the values  $C_1 = 3.741 \cdot 10^{-16}$  [ $\text{Wm}^2$ ] and  $C_2 = 1.438 \cdot 10^{-2}$  [ $\text{mK}$ ]. The integration at a given temperature over the entire wavelength spectrum results in the total thermal radiation of a black body:

$$E_b = \int_0^\infty E_{b\lambda} d\lambda_w = \sigma \cdot T^4 \quad (\text{B.4})$$

## Appendix

---

where  $\sigma$  is the Stefan-Boltzmann constant with the value  $5.67 \cdot 10^{-8} \text{ [W/m}^2 \cdot \text{K}^4]$ . The radiative energy from a nonblack surface corresponds to the radiative heat flux density  $\dot{q}_w$  and is obtained from (B.2) and (B.4):

$$E = \varepsilon \cdot \sigma \cdot T^4 = \dot{q}_w. \quad (\text{B.5})$$

The total spectral emission coefficient  $\varepsilon$  is independent of the wavelength. Such a nonblack monochromatic surface is called a grey body. In practice, a grey body assumption is acceptable for engineering analysis, because real bodies emit less than a black body at the same temperature over the entire spectrum. However, a real surface radiates at any wavelength with  $\varepsilon(T)$ . Figure B.1 demonstrates the benefit of this simplification from a real surface to black and grey bodies [49]. Another important relation for the radiation of heat is Kirchoff's law of thermal radiation:

$$\alpha_\lambda = \varepsilon_\lambda. \quad (\text{B.6})$$

The spectral emissivity of a surface is equal to the spectral absorptivity for a diffuse grey body which is comparable to most technical surfaces [41].

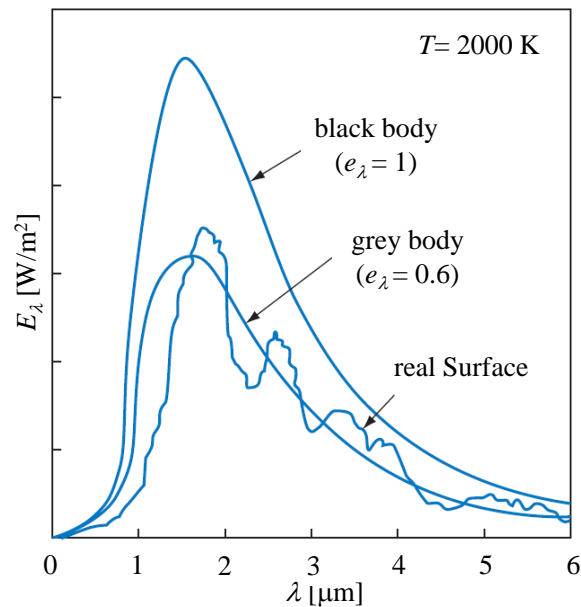


Figure B.1: Monochromatic emission of a black, grey and real surface [49].

## C Basics of discretization

### C.1 Spatial discretization

The partial derivatives  $\partial/\partial x$ ,  $\partial/\partial y$  and  $\partial/\partial z$  are generally substituted by finite differences (FD)  $\Delta/\Delta x$ ,  $\Delta/\Delta y$  and  $\Delta/\Delta z$  for the spatial discretization. As an example we will discretize the representative  $x$ -component of the velocity at the point  $P(i,j)$  in Figure C.1.

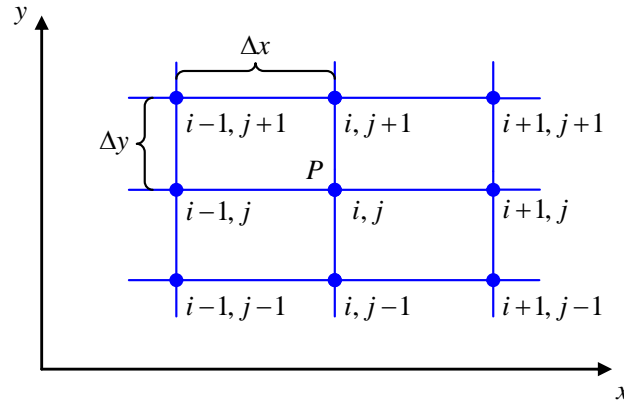


Figure C.1: Finite difference mesh.

The velocity  $u_{i+1,j}$  at the point  $(i+1,j)$  can be expressed by a Taylor series expanded around the point  $(i,j)$  as

$$u_{i+1,j} = u_{i,j} + \left(\frac{\partial u}{\partial x}\right)_{i,j} \Delta x + \left(\frac{\partial^2 u}{\partial x^2}\right)_{i,j} \frac{(\Delta x)^2}{2} + \left(\frac{\partial^3 u}{\partial x^3}\right)_{i,j} \frac{(\Delta x)^3}{6} + \dots \quad (\text{C.1})$$

with

$$\Delta x = x_{i+1,j} - x_{i,j} . \quad (\text{C.2})$$

Equation (C.1) is a mathematically exact expression for an infinite number of terms or  $\Delta x \rightarrow 0$  and can be transformed to

$$\left(\frac{\partial u}{\partial x}\right)_{i,j} = \frac{u_{i+1,j} - u_{i,j}}{\Delta x} - \left(\frac{\partial^2 u}{\partial x^2}\right)_{i,j} \frac{(\Delta x)}{2} - \left(\frac{\partial^3 u}{\partial x^3}\right)_{i,j} \frac{(\Delta x)^2}{6} + \dots \quad (\text{C.3})$$

The first term on the right side is the finite difference representation and the remaining terms exhibit a truncation error  $O(\Delta x)$ , i.e.

$$\left(\frac{\partial u}{\partial x}\right)_{i,j} = \frac{u_{i+1,j} - u_{i,j}}{\Delta x} + O(\Delta x) . \quad (\text{C.4})$$

The lowest term in the truncation error is  $\Delta x$  hence the finite expression in (C.4) is first-order-accurate. Furthermore, the discretization has been written for the forward point  $(i+1,j)$ , therefore (C.4) is called forward difference. The truncation error is constituted by the higher order terms in the Taylor series. A finite difference equation is consistent if the truncation error vanishes as the mesh is refined. A numerical scheme is stable if the errors (truncation and round-off) are not permitted to grow from one marching step to the next. Generally, a consistent and stable scheme is always convergent, i.e. the solution of the finite difference equations approaches the solution of the PDE (with the same initial and boundary conditions) as the mesh is refined [55, 57].

The same procedure with Taylor series can be carried out for the rearward point  $(i-1,j)$

$$u_{i-1,j} = u_{i,j} + \left(\frac{\partial u}{\partial x}\right)_{i,j} (-\Delta x) + \left(\frac{\partial^2 u}{\partial x^2}\right)_{i,j} \frac{(-\Delta x)^2}{2} + \left(\frac{\partial^3 u}{\partial x^3}\right)_{i,j} \frac{(-\Delta x)^3}{6} + \dots \quad (\text{C.5})$$

to yield the first-order backward difference

$$\left(\frac{\partial u}{\partial x}\right)_{i,j} = \frac{u_{i,j} - u_{i-1,j}}{\Delta x} + O(\Delta x) . \quad (\text{C.6})$$

First-order accuracy is not sufficient for the most CFD applications. Consequently, a FD quotient of second-order accuracy is subtracted from (C.1) and (C.5):

$$u_{i+1,j} - u_{i-1,j} = 2\left(\frac{\partial u}{\partial x}\right)_{i,j} \Delta x + 2\left(\frac{\partial^3 u}{\partial x^3}\right)_{i,j} \frac{(\Delta x)^3}{6} + \dots \quad (\text{C.7})$$

Equation (C.7) is transformed to approximate the partial derivative as follows:

$$\left(\frac{\partial u}{\partial x}\right)_{i,j} = \frac{u_{i+1,j} - u_{i-1,j}}{2\Delta x} + O(\Delta x)^2 . \quad (\text{C.8})$$

The lowest-order term in the truncation error is  $O(\Delta x)^2$  and hence this quotient is called second-order central difference [54].

The finite differences of (C.4), (C.6) and (C.8) are defined for the first-order derivatives of the conservation equations. However, the highest order in the momentum and energy equations are second-order partial derivatives, as e.g. in the viscous terms. With the summation of the Taylor series (C.1) and (C.5)

$$u_{i+1,j} + u_{i-1,j} = 2u_{i,j} + \left( \frac{\partial^2 u}{\partial x^2} \right)_{i,j} (\Delta x)^2 + \left( \frac{\partial^4 u}{\partial x^4} \right)_{i,j} \frac{(\Delta x)^4}{12} + \dots \quad (\text{C.9})$$

we obtain the second-order central second difference with respect to  $x$ :

$$\left( \frac{\partial^2 u}{\partial x^2} \right)_{i,j} = \frac{u_{i+1,j} - 2u_{i,j} + u_{i-1,j}}{(\Delta x)^2} + O(\Delta x)^2. \quad (\text{C.10})$$

For the case of mixed derivatives like  $\partial^2 u / \partial x \partial y$  the appropriate quotient is

$$\left( \frac{\partial^2 u}{\partial x \partial y} \right)_{i,j} = \frac{u_{i+1,j+1} - u_{i+1,j-1} - u_{i-1,j+1} + u_{i-1,j-1}}{4\Delta x \Delta y} + O\left[ (\Delta x)^2, (\Delta y)^2 \right]. \quad (\text{C.11})$$

It is important to note that differences with higher-order accuracy are also possible if we use more mesh points (e.g.: forward second order with  $(i,j)$ ,  $(i+1,j)$ ,  $(i+2,j)$ ). Second-order accuracy with the central discretization is the standard in commercial CFD codes. However, when the flow has discontinuities such as shock waves, the central spatial differences result in an error since they assume a continuous propagation of the flow. Therefore, modern CFD codes with upwind methods automatically change the discretization direction with the flow propagation. Single-sided differences are used for the boundaries of the mesh at the inlet, outlet and walls [54].

## C.2 Time discretization

The space and time variables are essentially decoupled and can be discretized independently to obtain an algebraic system. The discretization of the partial derivative  $\partial / \partial t$  is similar to the spatial differences described above. Figure C.2 shows three different time levels  $(n-1)$ ,  $(n)$  and  $(n+1)$  and one spatial direction of the mesh. The values at time  $(n+1)$  can be calculated once all previous values are known. Time marching variables are indicated by a superscript in the finite difference quotient [54].

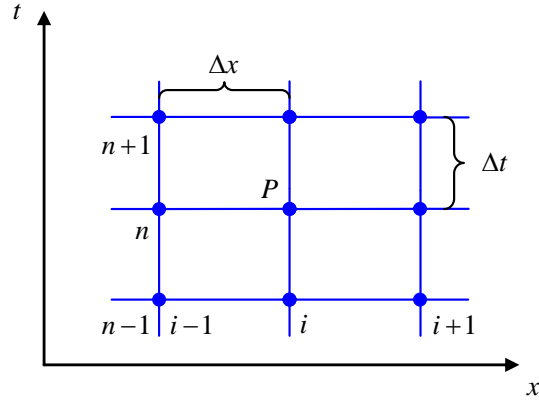


Figure C.2: Time levels for the temporal discretization.

The temporal first-order forward difference can be written as

$$\left(\frac{\partial u}{\partial t}\right)_i^n = \frac{u_i^{n+1} - u_i^n}{\Delta t} + O(\Delta t) \quad (\text{C.12})$$

and the temporal second-order central difference is

$$\left(\frac{\partial u}{\partial t}\right)_i^n = \frac{u_i^{n+1} - u_i^{n-1}}{2\Delta t} + O(\Delta t)^2. \quad (\text{C.13})$$

### C.3 Difference equations

A difference equation is the resulting algebraic equation once all partial derivatives of a PDE have been replaced by finite difference quotients. The difference quotients derived in subsection C.1 and C.2 are used to replace the partial derivatives of the conservation equations and solve the system of algebraic differences at each mesh point. The difference equations will be shown for the conservation equations (2.3), (2.15) and (2.16). For simplicity, the volume forces and external heat sources are neglected and the continuity equation (2.3) can be written for the 2-dimensional example as

$$\frac{\partial \rho}{\partial t} + \frac{\partial(\rho u)}{\partial x} + \frac{\partial(\rho v)}{\partial y} = 0. \quad (\text{C.14})$$

The Navier-Stokes equations (2.15) without the volume forces have the form

$$\begin{aligned} \frac{\partial(\rho u)}{\partial t} + \frac{\partial(\rho u^2)}{\partial x} + \frac{\partial(\rho uv)}{\partial y} &= -\frac{\partial p}{\partial x} + \frac{\partial \tau_{xx}}{\partial x} + \frac{\partial \tau_{xy}}{\partial y}, \\ \frac{\partial(\rho v)}{\partial t} + \frac{\partial(\rho uv)}{\partial x} + \frac{\partial(\rho v^2)}{\partial y} &= -\frac{\partial p}{\partial y} + \frac{\partial \tau_{xy}}{\partial x} + \frac{\partial \tau_{yy}}{\partial y}. \end{aligned} \quad (\text{C.15})$$

Furthermore, the volume forces and external heat sources are neglected for the conservation of energy in (2.16) and the equation is simplified to

$$\begin{aligned} \frac{\partial e_t}{\partial t} + \frac{\partial(ue_t)}{\partial x} + \frac{\partial(v e_t)}{\partial y} &= \\ -\frac{\partial(\rho u)}{\partial x} - \frac{\partial(\rho v)}{\partial y} + \frac{\partial}{\partial x}(u\tau_{xx} + v\tau_{xy}) + \frac{\partial}{\partial y}(u\tau_{xy} + v\tau_{yy}) + \bar{q}_Q. \end{aligned} \quad (\text{C.16})$$

The equations (C.14) - (C.16) have the same generic form and can be formulated in vector notation as

$$\frac{\partial}{\partial t} \bar{U} + \frac{\partial}{\partial x} \bar{E} + \frac{\partial}{\partial y} \bar{F} = 0, \quad (\text{C.17})$$

with the flux vectors:

$$\bar{U} = \begin{pmatrix} \rho \\ \rho u \\ \rho v \\ e_t \end{pmatrix}, \quad (\text{C.18})$$

$$\bar{E} = \begin{pmatrix} \rho u \\ \rho u^2 + p - \tau_{xx} \\ \rho uv - \tau_{xy} \\ e_t u + pu - \tau_{xx} u - \tau_{xy} v + \dot{q}_{Qx} \end{pmatrix}, \quad (\text{C.19})$$

$$\bar{F} = \begin{pmatrix} \rho v \\ \rho uv - \tau_{xy} \\ \rho v^2 + p - \tau_{yy} \\ e_t v + pv - \tau_{xy} u - \tau_{yy} v + \dot{q}_{Qy} \end{pmatrix}. \quad (\text{C.20})$$

Second-order central differences are used for the two spatial derivatives as

$$\begin{aligned} \left( \frac{\partial \bar{E}}{\partial x} \right)_{i,j} &= \frac{\bar{E}_{i+1,j} - \bar{E}_{i-1,j}}{2\Delta x} + O(\Delta x)^2, \\ \left( \frac{\partial \bar{F}}{\partial y} \right)_{i,j} &= \frac{\bar{F}_{i,j+1} - \bar{F}_{i,j-1}}{2\Delta y} + O(\Delta y)^2 \end{aligned} \quad (\text{C.21})$$

and the time marching term is discretized by a first-order forward quotient as

$$\left( \frac{\partial \bar{U}}{\partial t} \right)_{i,j}^n = \frac{\bar{U}_{i,j}^{n+1} - \bar{U}_{i,j}^n}{\Delta t} + O(\Delta t). \quad (\text{C.22})$$

Thereupon, the difference equations (C.21) and (C.22) are applied to (C.17) and transformed to equations for the unknown vectors with the truncation errors neglected:

$$\bar{U}_{i,j}^{n+1} = \bar{U}_{i,j}^n - \frac{\Delta t}{2} \left[ \frac{\bar{E}_{i+1,j}^n - \bar{E}_{i-1,j}^n}{\Delta x} + \frac{\bar{F}_{i,j+1}^n - \bar{F}_{i,j-1}^n}{\Delta y} \right]. \quad (\text{C.23})$$

The truncation errors show that the accuracy of the time approximation is of first-order and that of the space discretization of second-order. The conserved quantity  $\bar{U}$  in the grid point  $(i,j)$  at the time instant  $(n+1)$  can be approximately calculated with (C.23), since the flux vectors  $\bar{E}$  and  $\bar{F}$  are assumed to be known at the time instant  $n$ .

#### C.4 Explicit versus implicit approach

The flux vectors can be calculated explicitly or implicitly depending on the corresponding time level. The two approaches will be described for the 1-dimensional version of (C.23):

$$\bar{U}_i^{n+1} = \bar{U}_i^n - \frac{\Delta t}{2} \left[ \frac{\bar{E}_{i+1}^n - \bar{E}_{i-1}^n}{\Delta x} \right]. \quad (\text{C.24})$$

The flux vectors  $\bar{E}_{i+1}^n$  and  $\bar{E}_{i-1}^n$  in (C.24) are written in an *explicit* difference scheme at the time instant  $(n)$ . This has the advantage that the vectors are known and the CFD code is simple. However, the time step  $\Delta t$  has to be generally chosen to be very small to maintain stability resulting in an increase of computation time.

The *implicit* method uses the vector fluxes at the time instant  $(n+1)$  and we obtain

$$\bar{U}_i^n = \bar{U}_i^{n+1} + \frac{\Delta t}{2} \left[ \frac{\bar{E}_{i+1}^{n+1} - \bar{E}_{i-1}^{n+1}}{\Delta x} \right]. \quad (\text{C.25})$$

The variable of interest  $\bar{U}_i^{n+1}$  cannot be calculated directly because the flux vectors  $\bar{E}_{i+1}^{n+1}$  and  $\bar{E}_{i-1}^{n+1}$  in (C.25) are still unknown at the time instant  $(n+1)$ . Accordingly, we apply (C.25) at every grid point of the mesh and solve the tridiagonal matrix equation

$$\begin{bmatrix} \vdots \\ \bar{U}_i^n \\ \bar{U}_{i+1}^n \\ \bar{U}_{i+2}^n \\ \vdots \end{bmatrix} = \begin{bmatrix} \vdots \\ \bar{U}_i^{n+1} \\ \bar{U}_{i+1}^{n+1} \\ \bar{U}_{i+2}^{n+1} \\ \vdots \end{bmatrix} \cdot \begin{bmatrix} \ddots & 1 & & \ddots & 0 & 0 & 0 & 0 \\ 0 & c \frac{\bar{E}_{i-1}^{n+1}}{\bar{U}_{i-1}^{n+1}} & 1 & c \frac{\bar{E}_{i+1}^{n+1}}{\bar{U}_{i+1}^{n+1}} & 0 & 0 & 0 & 0 \\ 0 & 0 & c \frac{\bar{E}_i^{n+1}}{\bar{U}_i^{n+1}} & 1 & c \frac{\bar{E}_{i+2}^{n+1}}{\bar{U}_{i+2}^{n+1}} & 0 & 0 & 0 \\ 0 & 0 & 0 & c \frac{\bar{E}_{i+1}^{n+1}}{\bar{U}_{i+1}^{n+1}} & 1 & c \frac{\bar{E}_{i+3}^{n+1}}{\bar{U}_{i+3}^{n+1}} & 0 & 0 \\ 0 & 0 & 0 & 0 & \ddots & 1 & \ddots & \ddots \end{bmatrix}. \quad (\text{C.26})$$

The calculation time per iteration of (C.26) is longer than that of the explicit scheme but the necessary number of time steps is lower and the overall computational time decreases. However, an implicit scheme is more complicated to set up for CFD codes and the application of explicit schemes dominates nowadays. Explicit methods are simpler and more flexible and the convergence can be accelerated by various techniques like local time step control or multi-grid methods [56].

## D Turbulence models

### D.1 Standard $k$ - $\varepsilon$ model

The  $k$ - $\varepsilon$  model is a complete two-equation model rendering it unnecessary to know the turbulence structure. The starting point for a two-equation model is the Boussinesq approximation in (2.76). The independence of the 6 different Reynolds stresses is not valid any more, since they are modelled by one parameter only, the eddy viscosity. The turbulence is assumed to be isotropic and the eddy viscosity is defined as

$$\mu_t = C_\mu \cdot \rho \cdot \frac{k^2}{\varepsilon} \quad (\text{D.1})$$

with the turbulent kinetic energy  $k$ , the dissipation  $\varepsilon$ , the constant  $C_\mu$  and the density  $\rho$ . The derivation of the kinetic energy and the turbulent dissipation are based on (2.79) and presented in detail in [57] and [76]. The production term describes the generation of the turbulent kinetic energy as

$$P_k = \mu_t \frac{\partial \bar{u}_i}{\partial x_j} \left( \frac{\partial \bar{u}_i}{\partial x_j} + \frac{\partial \bar{u}_j}{\partial x_i} \right). \quad (\text{D.2})$$

The turbulent kinetic energy is obtained as

$$\underbrace{\rho \frac{\partial k}{\partial t} + \rho \bar{u}_j \frac{\partial k}{\partial x_j}}_{\text{Convection}} = \underbrace{P_k}_{\text{Production}} + \underbrace{\frac{\partial}{\partial x_j} \left[ \left( \mu + \frac{\mu_t}{\sigma_k} \right) \frac{\partial k}{\partial x_j} \right]}_{\text{Diffusion}} - \underbrace{\rho \cdot \varepsilon}_{\text{Dissipation}} \quad (\text{D.3})$$

and the turbulent dissipation is defined by

$$\underbrace{\rho \frac{\partial \varepsilon}{\partial t} + \rho \bar{u}_j \frac{\partial \varepsilon}{\partial x_j}}_{\text{Convection}} = \underbrace{C_{\varepsilon 1} \frac{\varepsilon}{k} P_k}_{\text{Production}} + \underbrace{\frac{\partial}{\partial x_j} \left[ \left( \mu + \frac{\mu_t}{\sigma_\varepsilon} \right) \frac{\partial \varepsilon}{\partial x_j} \right]}_{\text{Diffusion}} - \underbrace{C_{\varepsilon 2} \cdot \rho \cdot \frac{\varepsilon^2}{k}}_{\text{Dissipation}} \quad (\text{D.4})$$

with the closure coefficients [46]:

$$C_{\varepsilon 1} = 1,44, \quad C_{\varepsilon 2} = 1,92, \quad C_\mu = 0,09, \quad \sigma_k = 1,0, \quad \sigma_\varepsilon = 1,3. \quad (\text{D.5})$$

The left hand sides of (D.3) and (D.4) are the rate of change of  $k$  or  $\varepsilon$  plus the transport of  $k$  or  $\varepsilon$  by convection. The right hand sides are the rate of production plus the transport by diffusion minus the rate of dissipation of  $k$  or  $\varepsilon$ .

The  $k$ - $\varepsilon$  model is a simple and stable turbulence model and has a broad range of applicability. Hence it is available in many commercial CFD codes. Excellent results have been obtained by it for the computation of the free stream flows with relatively small pressure gradients for diverse problems including combustion, heat transfer and multi-phase flows. However, the calculation of flows near walls is a weak point of the model. The flow at walls separates too late and the separation area is computed to be too small.

## D.2 Wilcox $k$ - $\omega$ model

The  $k$ - $\omega$  model is also a two-equation model with the second equation referring to the turbulent frequency  $\omega$  instead of the turbulent dissipation  $\varepsilon$ . The idea of using an equation for the turbulent frequency has already been put forward by Kolmogorov [113]. His approach has changed through subsequent developments to the state-of-the-art  $k$ - $\omega$  model of Wilcox [79] with the turbulent frequency

$$\rho \frac{\partial \omega}{\partial t} + \rho u_j \frac{\partial \omega}{\partial x_j} = \alpha \frac{\omega}{k} P_k + \frac{\partial}{\partial x_j} \left[ \left( \mu + \frac{\mu_t}{\sigma_\omega} \right) \frac{\partial \omega}{\partial x_j} \right] - \beta \cdot \rho \cdot \omega^2 \quad (\text{D.6})$$

and the turbulent viscosity

$$\mu_t = \rho \cdot \frac{k}{\omega} . \quad (\text{D.7})$$

The equation for the turbulent kinetic energy is a modified version of (D.3):

$$\rho \frac{\partial k}{\partial t} + \rho u_j \frac{\partial k}{\partial x_j} = P_k + \frac{\partial}{\partial x_j} \left[ \left( \mu + \frac{\mu_t}{\sigma_k} \right) \frac{\partial k}{\partial x_j} \right] - \beta' \cdot \rho \cdot k \cdot \omega \quad (\text{D.8})$$

with the turbulent dissipation

$$\varepsilon = \beta' \cdot k \cdot \omega . \quad (\text{D.9})$$

The values of the model constants are taken from [46]:

$$\beta = 0,09 , \quad \alpha = 0,556, \quad \beta = 0,075, \quad \sigma_k = 2,0, \quad \sigma_\omega = 2,0. \quad (\text{D.10})$$

The  $k$ - $\omega$  model is generally more accurate in the treatment of the viscous near-wall region than the  $k$ - $\varepsilon$  model. Especially separating flows at walls are more precise with lower boundary layer resolutions. However, the computation of free stream flows is inferior compared to the  $k$ - $\varepsilon$  model.

### D.3 SST $k$ - $\omega$ model

The model equations below are defined in [46] and [80].

#### Wilcox $k$ - $\omega$ model:

Turbulent kinetic energy  $k$  equation:

$$\rho \frac{\partial k}{\partial t} + \rho u_j \frac{\partial k}{\partial x_j} = P_k + \frac{\partial}{\partial x_j} \left[ \left( \mu + \frac{\mu_t}{\sigma_k} \right) \frac{\partial k}{\partial x_j} \right] - \beta' \cdot \rho \cdot k \cdot \omega \quad (\text{D.11})$$

Turbulent frequency  $\omega$  equation:

$$\rho \frac{\partial \omega}{\partial t} + \rho u_j \frac{\partial \omega}{\partial x_j} = \alpha \frac{\omega}{k} P_k + \frac{\partial}{\partial x_j} \left[ \left( \mu + \frac{\mu_t}{\sigma_\omega} \right) \frac{\partial \omega}{\partial x_j} \right] - \beta \cdot \rho \cdot \omega^2 \quad (\text{D.12})$$

#### Transformed $k$ - $\varepsilon$ model:

Turbulent kinetic energy  $k$  equation:

$$\rho \frac{\partial k}{\partial t} + \rho u_j \frac{\partial k}{\partial x_j} = P_k + \frac{\partial}{\partial x_j} \left[ \left( \mu + \frac{\mu_t}{\sigma_{k2}} \right) \frac{\partial k}{\partial x_j} \right] - \beta' \cdot \rho \cdot k \cdot \omega \quad (\text{D.13})$$

Turbulent frequency  $\varepsilon$  equation:

$$\rho \frac{\partial \omega}{\partial t} + \rho u_j \frac{\partial \omega}{\partial x_j} = \alpha_2 \frac{\omega}{k} P_k + \frac{\partial}{\partial x_j} \left[ \left( \mu + \frac{\mu_t}{\sigma_{\omega 2}} \right) \frac{\partial \omega}{\partial x_j} \right] - \beta_2 \cdot \rho \cdot \omega^2 + 2\rho \frac{1}{\sigma_{\omega 2} \omega} \frac{\partial k}{\partial x_j} \frac{\partial \omega}{\partial x_j} \quad (\text{D.14})$$

Equation (D.11) and (D.12) are multiplied with  $F_1$  and (D.13) and (D.14) are multiplied by  $(1 - F_1)$ . The corresponding equations of each model are added together to give the new model:

$$\rho \frac{\partial k}{\partial t} + \rho \bar{u}_j \frac{\partial k}{\partial x_j} = P_k + \frac{\partial}{\partial x_j} \left[ \left( \mu + \frac{\mu_t}{\sigma_{k3}} \right) \frac{\partial k}{\partial x_j} \right] - \rho \cdot \beta' \cdot k \cdot \omega \quad (\text{D.15})$$

$$\begin{aligned} \rho \frac{\partial \omega}{\partial t} + \rho \bar{u}_j \frac{\partial \omega}{\partial x_j} = \\ \alpha_3 \frac{\omega}{k} P_k + \frac{\partial}{\partial x_j} \left[ \left( \mu + \frac{\mu_t}{\sigma_{\omega 3}} \right) \frac{\partial \omega}{\partial x_j} \right] - \beta_3 \cdot \rho \cdot \omega^2 + (1 - F_1) 2\rho \frac{1}{\sigma_{\omega 2} \omega} \frac{\partial k}{\partial x_j} \frac{\partial \omega}{\partial x_j} \end{aligned} \quad (\text{D.16})$$

**Blending function  $F_1$ :**

$$F_1 = \tanh \left\{ \left\{ \min \left[ \max \left( \frac{\sqrt{k}}{\beta' \omega y}, \frac{500\nu}{y^2 \omega} \right), \frac{4\rho \sigma_{w2} k}{CD_{k\omega} y^2} \right] \right\}^4 \right\} \quad (\text{D.17})$$

with

$$CD_{k\omega} = \max \left( 2\rho \frac{1}{\sigma_{\omega 2} \omega} \frac{\partial k}{\partial x_j} \frac{\partial \omega}{\partial x_j}, 1 \cdot 10^{-10} \right) \quad (\text{D.18})$$

**Turbulent viscosity  $\mu_t$ :**

$$\mu_t = \frac{\rho \cdot a_1 \cdot k}{\max(a_1 \omega, SF_2)} \quad (\text{D.19})$$

with the blending function  $F_2$

$$F_2 = \tanh \left\{ \left[ \max \left( \frac{2 \cdot \sqrt{k}}{\beta' \omega y}, \frac{500\nu}{y^2 \omega} \right) \right]^2 \right\} \quad (\text{D.20})$$

and the magnitude of the strain rate

$$S = \frac{1}{2} \left( \frac{\partial \bar{u}_i}{\partial x_j} + \frac{\partial \bar{u}_j}{\partial x_i} \right) \quad (\text{D.21})$$

The coefficients of the SST turbulence model are a linear combination of the corresponding coefficients of the  $k$ - $\varepsilon$  and  $k$ - $\omega$  model

$$\Phi_3 = F_1 \Phi_1 + (1 - F_1) \Phi_2 \quad (\text{D.22})$$

## Appendix

---

with the coefficients

$$\beta = 0.09, \quad \alpha = 0.5556, \quad \beta = 0.075, \quad \sigma_k = 2.0, \quad \sigma_\omega = 2.0, \quad (\text{D.23})$$

$$\alpha_2 = 0.44, \quad \beta_2 = 0.0828, \quad \sigma_{\omega_2} = 1.168, \quad \sigma_{k_2} = 1.0, \quad (\text{D.24})$$